ORGANIC ELECTRODES FOR STRUCTURAL ENERGY AND POWER

A Dissertation

by

SE RA KWON

Submitted to the Office of Graduate and Professional Studies of
Texas A&M University
in partial fulfillment of the requirements for the degree of

DOCTOR OF PHILOSOPHY

Chair of Committee,	Jodie L. Lutkenhaus
Committee Members,	Perla Balbuena
	Mustafa Akbulut
	Partha Mukherjee
Head of Department,	M. Nazmul Karim

May 2017

Major Subject: Chemical Engineering

ABSTRACT

Structural power systems, which simultaneously provide structural and electrochemical energy storage functionalities, have arisen as an emerging need for a wide range of applications. A challenge is to develop the multifunctional composite electrodes which can perform the acceptable energy storage and mechanical roles in a single platform. Composite electrodes containing graphene and polymers are designed using different processing techniques and examined in the context of multifunctional structural electrodes. The relationship between materials properties, processing methods, and performance of the composite electrodes is investigated.

Polyaniline nanofibers (PANI NF)/reduced graphene oxide (RGO) composite electrodes are fabricated using spray-assisted layer-by-layer (LbL) assembly. In this spray-on approach, the most critical parameters to create uniform electrodes are blow-drying time and removal of rinsing step. The architecture and electrochemical performance are investigated and compared against control electrodes made by dip-assisted LbL assembly. The spray-assisted PANI NF/RGO LbL electrodes exhibit over 70 times faster film growth behavior and a more porous structure than dip-assisted LbL electrodes. The increased porosity enables an enhanced rate capability and a higher power at a given specific energy compared to dip-assisted LbL electrodes.

To design multifunctional structural electrodes, mechanically strong aramid nanofibers (ANFs) are utilized as reinforcing building blocks and blended with graphene using different film fabrication techniques. RGO/ANF LbL films are fabricated using

dip-assisted LbL assembly. The resulting electrodes exhibit an ANF-rich structure where ANFs act as a polymer matrix that interfacially interacts with RGO sheets. Chemical reduction leads to higher electrochemical performance. Nanomechanical testing shows that the electrodes have a modulus intermediate between the individual ANF and GO components. No cracks or defects are observed upon flexing 1000 times, which demonstrates that RGO/ANF LbL electrodes are promising for flexible, mechanically robust energy and power.

Free-standing RGO/ANF supercapacitor electrodes are fabricated via vacuum-assisted filtration and exhibit extraordinary mechanical strength and excellent electrochemical performance, which is attributed to the incorporation of ANFs as reinforcing nanofillers into the system where RGO sheets are interconnected with ANFs by non-covalent interfacial interactions. The RGO/ANF composite electrodes show multifunctionality superior to that of other graphene-based supercapacitors, indicating an excellent combination of both mechanical and electrochemical properties.

ACKNOWLEDGEMENTS

I would like to thank my committee chair, Dr. Lutkenhaus, and committee members, Dr. Balbuena, Dr. Akbulut, and Dr. Mukherjee, for their guidance and support throughout the course of this research.

Thanks also go to my colleagues, friends, the department faculties, staffs, and collaborators for making my time a great experience.

Finally, thanks to my mother, father, and brother for their encouragement.

CONTRIBUTORS AND FUNDING SOURCES

Contributors

This work was supervised by a dissertation committee consisting of Professor Jodie L. Lutkenhaus, Professor Perla Balbuena, and Professor Mustafa Akbulut of the Department of Chemical Engineering and Professor Partha Mukherjee of the Department of Mechanical Engineering.

The analyses depicted in Chapter 2 were conducted in part by Ju-Won Jeon of the Department of Chemical Engineering and were published in 2015. The data analyzed in Chapter 3 was conducted in part by Meagan B. Elinski and Professor James D. Batteas of the Department of Chemistry. The data analyzed in Chapter 4 was provided in part by John Harris of the Department of Chemical Engineering, Tianyang Zhou of the Department of Materials Science and Engineering, and Professor James G. Boyd of the Department of Aerospace Engineering.

All other work conducted for the dissertation was completed by the student independently.

Funding Sources

This work was made possible in part by the Air Force Office of Scientific Research under Grant Number FA9550-13-1-0147. Its contents are solely the responsibility of the authors and do not necessarily represent the official views of the Air Force Office of Scientific Research.

TABLE OF CONTENTS

Page

LIST OF FIGURES

FIGURE Page

FIGURE Page

FIGURE Page

FIGURE Page

LIST OF TABLES

CHAPTER I

INTRODUCTION

1.1 Introductory Remarks and Background

There is an emerging need for structural energy and power, which simultaneously provides energy storage and structural functionalities for a wide range of application, including aerial and ground vehicles and portable and wearable electronics. As a component, structural energy storage system such as lithium ion batteries and supercapacitors plays a critical role in the multifunctional performance as well as the reduction in mass or volume of the power system. The structural elements of the power system include mechanical strength and stiffness, adaptability to various substrates, and flexibility of the system.

Flexible energy storage devices, one of the structural power systems, have attracted great attention for the applications in portable, wearable electronics, such as roll-up displays, paper batteries, and paintable batteries.[1-4] For these flexible energy storage devices with various geometries, structural elements which can be folded, stretched, and seamlessly integrated into diverse platform are required.

The structural power system can be designed through structural electrodes, structural electrolytes, packaging, and multifunctional matrix.[5] Specifically, a structural electrode which performs both mechanical and energy storage roles in one electrode unit is a key component in the structural energy storage system. A simple approach to design the structural electrodes is using a structural material which possesses both

electrochemical and mechanical properties as itself. However, only a limited selection is offered. The examples are carbon-based materials such as carbon fiber, graphene, and carbon nanotubes.[6-9] While these choices can perform multifunctional roles, the material alone cannot easily achieve the desired performance in both properties.

An alternative strategy to the limited selection is multifunctional composite materials, the combination of components which are highly efficient in a given individual property. Multifunctional composites for the use as structural electrodes consist of constituents which can simultaneously and synergistically offer electrochemical and structural functions. For developing the multifunctional structural composite electrodes, a challenge is to optimize the energy storage and mechanical performance simultaneously without sacrificing either property. Since individual properties of components usually conflict with each other within the composite architecture, the balance between the electrochemical and structural properties as well as the synergistic effect from the combination are critical to address the issue. Thus, the structural composite electrodes can be designed by rationally selecting each constituent of the composite and optimizing the composition of each component within the composite.

Together, the processing techniques to create multifunctional composites can significantly influence the structure and performance of the structural power composites. Layer-by-layer (LbL) assembly and vacuum-assisted filtration are powerful techniques for the fabrication of multicomposite hybrid film. In LbL assembly, the film is fabricated via the alternate exposure of a substrate to the desired polyelectrolyte solution or

colloidal dispersion and film properties such as thickness, composition, and structure can be finely controlled by processing parameters.[10] In vacuum-assisted filtration, the film is fabricated using a self-assembly technique in which a suspension is under vacuum induced directional flow. The thickness and the structure can be controlled by varying the concentration of the suspension and filtration volume.[11-12] These processing methods can control nanoscale architecture and create hybrid film with well ordered, uniform layers. Therefore, LbL assembly and vacuum-assisted filtration are selected for designing multifunctional structural composite electrodes because the electrochemical and mechanical functions including charge storage and stress-transfer are highly dependent on the nanostructure of the composites.

In this context, this thesis demonstrates how selected materials and processing techniques can control the multifunctional properties, both electrochemical and mechanical performance of the structural energy storage system, providing a promising way to design multifunctional composite electrodes.

1.2 Electrochemical Energy Storage

Conventional electrochemical energy storage system can be classified into batteries, supercapacitors, and dielectric capacitors according to their energy storage mechanism and performance. The performance considers two main parameters, energy density and power density, which is how much energy can be stored and how fast the energy can be delivered, respectively. As illustrated Figure 1.1, batteries possess high energy density and modest power density due to a slow redox process mechanism. On

the other hand, dielectric capacitors provide low energy density and high power density. Supercapacitors offer moderate performance between batteries and dielectric capacitors, lower energy density and higher power capability than batteries.

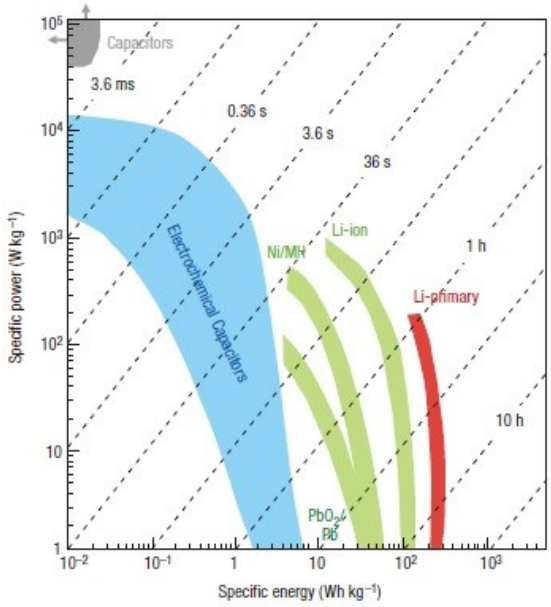

Figure 1.1. Specific energy against specific power for various electrical energy storage systems. Reproduced with permission.[13] Copyright 2008, Macmillan Publishers Limited.

1.2.1 Batteries

Since the Sony Co. has introduced the first commercial lithium-ion battery in 1991, lithium-ion batteries have become among the most commonly used power sources for a wide range of applications including portable electronics, microelectronics, electrical vehicles, hybrid electric vehicles, and plug-in hybrid electrical vehicles.[14] This is because the lithium-ion batteries have many advantages compared to previous

secondary batteries such as light weight, high energy density, and high energy efficiency.

A conventional lithium-ion battery is composed of three primary components; a cathode, an anode, and an electrolyte. Lithium-ion batteries store energy chemically by lithium intercalation/deintercalation processes between the anode and cathode.[15] The schematic illustration of lithium ion batteries is represented in Figure 1.2.

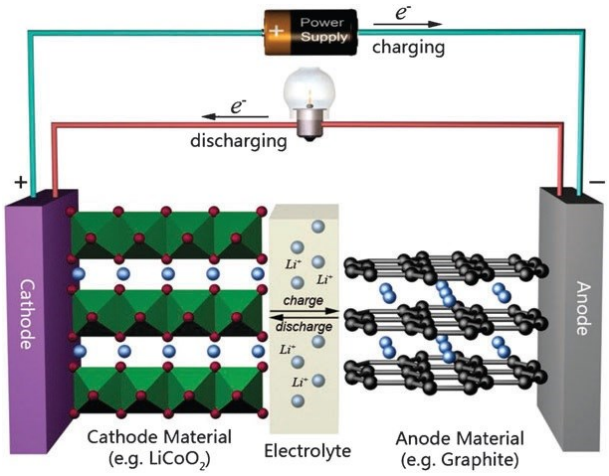

Figure 1.2. Schematic illustration of the charge/discharge processes in lithium ion batteries. Reproduced with permission.[16] Copyright 2011, Royal Society of Chemistry.

The most commonly used cathode and anode materials for lithium ion batteries are lithium cobalt oxide ($LiCoO_2$) and graphitic carbon, respectively.[17] During the discharge process, reduction takes places at the cathode as shown in following equation,

$$xLi^+ + xe^- + CoO_2 \rightarrow Li_xCoO_2 \qquad (1.1)$$

During the discharge, oxidation takes places at the anode material as shown in following equation,

$$LiC_6 \rightarrow Li_{1-x}C_6 + xLi^x + xe^- \quad (1.2)$$

An electrolyte serves as a medium for the lithium ion transport involved in the charge/discharge cycle. Ideally, an electrolyte should have high ion conductivity, low vapor pressure, and thermal and chemical stability over a wide range of voltage and temperature. A mixture of organic carbonates such as ethylene carbonate, diethylene carbonate, or dimethylene carbonate containing lithium salts such as $LiPF_6$, $LiBF_4$, or $LiClO_4$, is typically used. Also, ionic liquid and solid polymer gel electrolyte can be used for lithium-ion batteries.[18-19] A separator is placed between two electrodes. The main function of the separator is to keep two electrodes apart to prevent physical contact of the electrodes while enabling the transport of ionic charge carriers.[20]

There have been considerable efforts to improve the electrochemical performance of the electrodes since the nature of the active materials plays a dominant role in determining the energy storage performance. As cathode materials, transition metal oxides like $LiMO_2$ (M = Co, Ni, Mn), lithium iron phosphate ($LiFePO_4$), and vanadium oxides (V_2O_5) have been widely investigated.[21-25] Besides these materials, polymer has been also used as a promising cathode material for lithium-ion batteries due to its low-cost, high energy density, and environmental benignity.[26-27] The polymeric electrode materials for batteries include conducting polymers, radical compounds, organosulfur, and carbonyl compounds.

There have been a lot of reports on conducting polymers for using as battery electrodes such as polyacetylene (PAc), polyaniline (PANI), polypyrrole (Ppy), and polythiophene (PT). Specifically, PANI is among the most widely used conducting polymers for the electrode material due to its good environmental stability, good conductivity, ease of synthesis, and unique redox chemistry via doping/dedoping. In addition, water-processability of PANI has facilitated the incorporation of PANI with many other materials and extended the applicable area of PANI.[28-29] PANI has different oxidation states (leucoemeraldine, emeraldine salt, and pernigraniline), and the different properties such as conductivity and electrochromism can be shown depending on dopant, voltage, and environment.[30] Charge can be stored through reversible oxidation/reduction (doping/dedoping) between leucoemeraldine and emeraldine forms.[29] Especially, nanostructured PANI, such as nanofibers, nanotubes, nanorods, and nanowires, has been widely studied and applied as electrode materials for enhancing the electrochemical properties, taking advantages of nanostructures such as high surface area, short diffusion paths, and continuous three-dimensional conducting framework.[29, 31-32]

1.2.2 Electrochemical capacitors and supercapacitors

Electrochemical capacitors and supercapacitors can store charge on the surface of the electrodes through electrical double layer capacitance or through pseudocapacitance, Figure 1.3. Electrical double layer capacitors depend on the reversible ion adsorption on the electrical double layer, which exists at the electrolyte-electrode interface.[33] Pseudocapacitors are based on the Faradaic electrochemical redox reaction at the

electrical double layer, near the surface of the active material.[33] Since the charge storage is limited to the surface reactions of active materials without ion diffusion within the bulk electrode materials, electrochemical capacitors and supercapacitors offer much higher power density, but lower energy density than batteries. In addition, surface-confined reaction makes the cycle life of electrochemical capacitors much longer than that of batteries without the structural changes of the electrodes caused by lithium intercalation/deintercalation.[34]

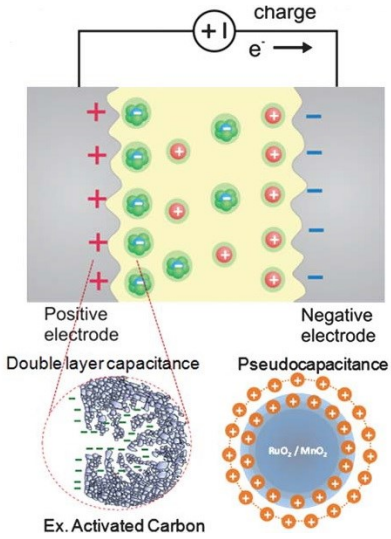

Figure 1.3. Schematic illustration of the charge/discharge processes in electrochemical capacitors. Reproduced with permission.[34] Copyright 2011, Royal Society of Chemistry.

The challenge for electrochemical capacitors and supercapacitors is to improve the energy density while maintaining their high power density and stable, long cycling advantages. The energy density of supercapacitors depends on the capacitance of the active material and overall cell voltage.[35] As a result, there have been a lot of efforts to

develop the electrode materials with large active surface area, specifically nanostructured materials.

Carbon materials are promising electrode materials for supercapacitors owing to high surface area, low cost, good electronic conductivity, and chemical stability.[36] Such examples are activated carbon, porous carbon, carbon nanotubes, and graphene. Carbon electrode materials in electrochemical capacitors are required to have high specific surface area, good conductivity, and excellent electrolyte accessibility.[37] Activated carbon has been used as a conventional electrode material for electrochemical capacitors due to its large surface area (2000 m^2/g) and high specific capacitance (100-200 F/g).[38-39] A lot of research efforts have focused on optimizing porous structure, controlling the morphology, and modifying the surface of carbon materials. The ordered hierarchical mesoporous/microporous carbon with narrow mesopore size and distribution and micropores on the mesopores walls improved specific capacitance, providing increased surface area and more favorable path for the electrolyte.[40] In addition, carbon materials with various morphologies including mesoporous carbon nanotubes, mesoporous carbon sphere arrays, mesoporous carbon nanofiber arrays were designed to achieve high surface area and electrical conductivity.[41-44] Another approach to enhance the performance of carbon electrode materials is surface functionalization. In this method, heteroatoms such as nitrogen and oxygen were incorporated in carbon materials and improved the performance, which was attributed to the Faradaic redox reaction of nitrogen and oxygen functional groups on the surface of carbon materials.[45-48]

Pseudocapacitive materials such as metal oxides and conducting polymers have been considered as promising electrode materials for supercapacitors. The pseudocapacitance of metal oxides involves both Faradaic redox reaction and the ion adsorption/desorption at electric double layer, leading to higher capacitance than carbon materials. Various metal oxides including RuO_2, IrO_2, MnO_2, V_2O_5, NiO, Co_3O_4, SnO_2, and Fe_2O_3 have been widely studied as pseudocapacitive electrode materials.[35, 49]

Conducting polymers, including Ppy, PANI, poly(3,4-ethylenedioxythiophene) (PEDOT), can store charge through highly reversible redox reaction on the surface and throughout the entire bulk electrode. PANI and Ppy are among the most widely used conducting polymer as electrode material in supercapacitors. PANI-coated hierarchical porous carbon composite and graphene-PANI composite electrodes for supercapacitors were developed and exhibited high specific capacitance and excellent cycling stability.[50-51] Also, nanocellulose-coupled Ppy/graphene oxide paper electrodes delivered high volumetric capacitance and showed stable cycling performance.[52]

1.3 Structural Materials

Structural materials are the materials used for their mechanical properties, primarily bearing the structural loads and dissipating the mechanical stress. Applications include aerial and ground transportation, body protection, energy production, and portable electronics. Structural materials can be metallic, ceramic, polymeric, or a composite between these materials. Specifically, the structural electrode materials for multifunctional structural power system which possess energy storage and load-bearing

capabilities are quite limited to carbon fibers, graphene, and carbon nanotubes. As a newly emerging structural material, aramid nanofibers have attracted great attention as polymeric building blocks for reinforcing nanocomposites. In this thesis, as structural materials, graphene and aramid nanofibers are used to design the multifunctional structural composite electrode materials.

1.3.1 Graphene

Graphene, a two-dimensional one-atom-thick planar sheet of sp^2 bonded carbon atoms, has been considered as a promising material due to its high electrical (200,000 $cm^2/V \cdot s$) and thermal conductivities (~5,000 $W/m \cdot K$), high mechanical strength (Young's modulus ~1,100 GPa, fracture strength ~125 GPa), and large specific surface area (2,630 m^2/g).[53-56] Especially, there have been numerous studies on the application of graphene and graphene-based composite materials to energy storage devices as an electrode material itself or as a conductive additive.[57-58]

Graphene has been produced through four different methods; chemical vapor deposition (CVD), mechanical exfoliation of graphite, epitaxial growth, and creation of colloidal suspensions.[53] Among these, the colloidal suspension approach to produce graphene and chemically modified graphene (CMG) from graphite or graphite-derivatives such as graphite oxide has been considered as a promising method for the bulk production of graphene. Chemical modification through the colloidal suspension method enables the use of graphene for a variety of applications.[11, 53, 59-62]

Figure 1.4 represents the typical colloidal suspension approach to prepare chemically converted graphene. The hydrophobic nature of graphene sheets causes irreversible aggregation of individual graphene sheets in solution-based processing, which prevents the full utilization of outstanding properties of individual graphene sheets.[59] Graphene oxide (GO) suspensions address this challenge without adding any dispersing agents. The hydrophilic GO suspension is obtained by the simple sonication of graphite oxide, chemically oxidized graphite.[63] Although the chemical oxidation yields homogenous colloidal dispersions, GO sheets are electrically insulating. The reduction of GO sheets can produce electrically conducting reduced graphene oxide (RGO) sheets.[53, 64] Chemical reduction using reductants is the most commonly used method to reduce GO sheets. The reducing agents can be hydrazine, including hydrazine monohydrate and dimethylhydrazine, metal hydride such as sodium hydride, sodium borohydride, ascorbic acid, and hydroiodic acid (HI).[65-69] Thermal treatment can be used to reduce the GO sheets by rapidly heating the GO up to 1050 ^{o}C.[64, 70] Also, the oxygen containing functional groups can be removed electrochemically.[71-72]

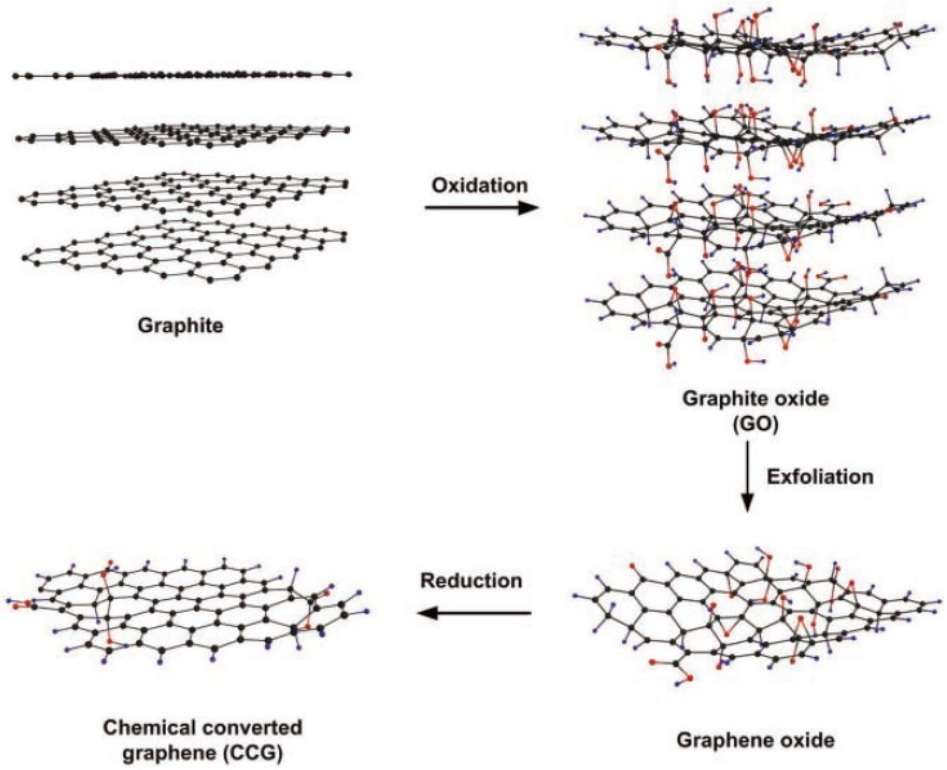

Figure 1.4. Chemically converted graphene by reduction of graphene oxide. Reproduced with permission.[73] Copyright 2011, Wiley-VCH.

As mentioned above, graphene and graphene-based composites have attracted great attention as an electrode material for energy storage devices such as batteries and supercapacitors due to their unique properties.[74] Graphene-based electrodes can be fabricated via a solution-based process, which is enabled by the liquid nature of CMO such as GO and RGO dispersions. Drop-casting, layer-by-layer assembly, and vacuum-assisted filtration of GO or RGO dispersion are commonly used to make the graphene film and the prepared GO film can be subsequently reduced by chemical, thermal, and electrochemical reduction. Graphene stores charge by both an electric double-layer

mechanism and a pseudocapacitive mechanism originating from the redox reaction of oxygen containing functional groups on the graphene basal sheet.[58, 75]

Further, graphene composite electrodes have been investigated to improve the electrochemical performance of the graphene electrodes. The electrochemical properties of graphene-metal oxide composite electrodes such as MnO_2/RGO, Fe_3O_4/RGO, and SnO_2/RGO were improved as compared to graphene-only electrodes, showing higher capacitance and enhanced rate capability and cycling behavior.[76-80] The incorporation of conducting polymers into the graphene electrodes such as RGO/PANI and RGO/Ppy composite electrodes exhibited stable performance and increased capacitance.[81-84] It was also reported that RGO/carbon nanotube (CNT) composite electrodes exhibited an enhancement in the capacitance and rate capability.[85-86] This enhancement of capacitance was attributed to the contribution of the pseudocapacitance of guest materials such as metal oxides, conducting polymers, and CNT to the overall capacitance. The introduction of the guest materials into the graphene electrodes can manipulate the structure and arrangement of the graphene sheets, which leads to higher performance of the electrodes.

1.3.2 Aramid nanofibers (ANFs)

Aramid nanofibers (ANFs), nanoscale Kevlar® fibers, are one of the most promising polymeric building blocks for nanocomposite materials. Kevlar®, an ultrastrong para-aramid synthetic macroscale fiber produced from poly(paraphenylene terephthalamide) (PPTA), is well known for its superior mechanical properties with a

modulus of 90 GPa and a tensile strength of 3.6 GPa.[87] The excellent mechanical properties arise from the highly-aligned backbone structure and the interactions between PPTA chains including π-π stacking, van der Waals forces, and hydrogen bonding, Figure 1.5.[86, 88] Kevlar® has been used as a reinforcing material for polymer matrix due to its high strength and stiffness.[89-91] However, the low reactivity and affinity caused by the inert structure of the PPTA chains has limited the incorporation of macroscale PPTA into composite materials.[89] There have been a lot of efforts to improve the reactivity of the PPTA with other materials such as hydrolysis and surface coating.[92-95]

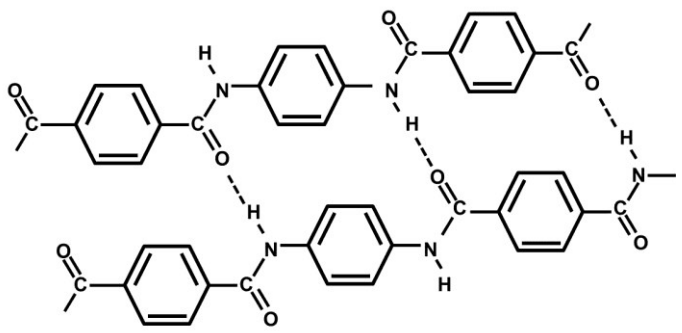

Figure 1.5. Molecular structure of PPTA.

A recently developed method to process Kevlar® into nanoscale ANFs, has addressed this issue. ANFs were obtained by the dissolution of macroscale bulk Kevlar® thread in dimethyl sulfoxide (DMSO) with potassium hydroxide (KOH).[86] The process occurs by the deprotonation of amide groups in the polymer chains and a stable dispersion of polymeric nanofibers with negatively charge surface functionalities was obtained.[86] The resulting ANFs is dark red liquid dispersion and the diameter of ANFs is

5-30 nm and the length is up to 10 μm.[86] Nanometer scale ANFs increase the available surface area and reactive sites to interact with other materials.[89] Also, the ANFs in the form of liquid dispersion can be utilized in various solvent-based processing techniques such as layer-by-layer assembly and vacuum-assisted filtration.[86] The nature of liquid dispersion and the enhancement of reactivity and adhesion with other materials lead to the easy incorporation of ANFs into nanocomposite materials in which the high mechanical properties are required.

There have been several reports on the nanocomposite materials containing ANFs as both reinforcing nanofillers and robust matrix, providing improved mechanical performance. Multi-walled carbon nanotube (MWNT)/Kevlar NF composite obtained from simple solution mixing of two materials increased the mechanical properties of poly(methyl methacrylate) polymer matrix (by 109 % tensile strength and by 89 % Young's modulus) acting as reinforcing nanofillers.[96] ANF/functionalized graphene composite nanofillers were also investigated for polymer reinforcement, showing an increase in tensile strength and Young's modulus by 84.5 % and 70.6 %, respectively.[97] Graphene/ANF composite film fabricated by vacuum-assisted filtration showed excellent mechanical properties (209.4 MPa for tensile strength and 29.4 GPa for Young's modulus) and electrical conductivity (145.8 S/m).[98] Au-ANFs composite films, Au nanoparticles aligned on spin-coated ANFs film, showed high mechanical strength (96 MPa for tensile strength) and electrical conductivity (1,250 S/cm).[99] In this composite, Au nanoparticles were incorporated into porous, high-strength ANFs networks and interconnected, resulting in three-dimensional conductive network.[99]

1.4 Methods

1.4.1 Layer-by-layer (LbL) assembly

Multifunctional materials such as structural electrodes can be created by designing a multi-composite material in which two or more individual components with desirable functionalities are combined using physical and chemical processes.[100] Among the various methods, layer-by-layer (LbL) assembly technique is a powerful tool for the fabrication of multi-composite hybrid film. The LbL assembly is a coating technique and the film is fabricated via alternate exposure of a substrate to oppositely charged polyelectrolyte or colloidal solutions.[100-101] A variety of materials can be applied for LbL assembly such as polyelectrolytes, inorganic nanoparticles, nanowires, clays, colloids, and proteins, which makes this film fabrication method versatile.[63, 101-106] Another advantage of LbL assembly is that LbL films can be built up uniformly on various substrates. LbL films can be assembled based on electrostatic interactions between charged species.[100] Other interactions such as ionic charge transfer, hydrogen bonding, covalent attachment, and van der Waals interaction also can be important driving forces in the assembly process.[10, 107]

The film characteristics such as structure and the thickness can be controlled by the deposition conditions such as pH value, solution concentration, adsorption time, ionic strength, and type of salts.[108-112] The thickness of the LbL films can be controlled by adjusting the number of layer pairs over the range from nanoscale to microscale, and the film architectures in multilayer LbL films are completely controlled by the

deposition sequence.[100] The LbL assembly has been widely used in numerous fields such as drug delivery system, energy devices, sensors, and anticorrosion coatings.[113-119]

The commonly used film buildup strategies of LbL assembly are dip-, spray-, and spin-assisted LbL deposition , Figure 1.6.[10]

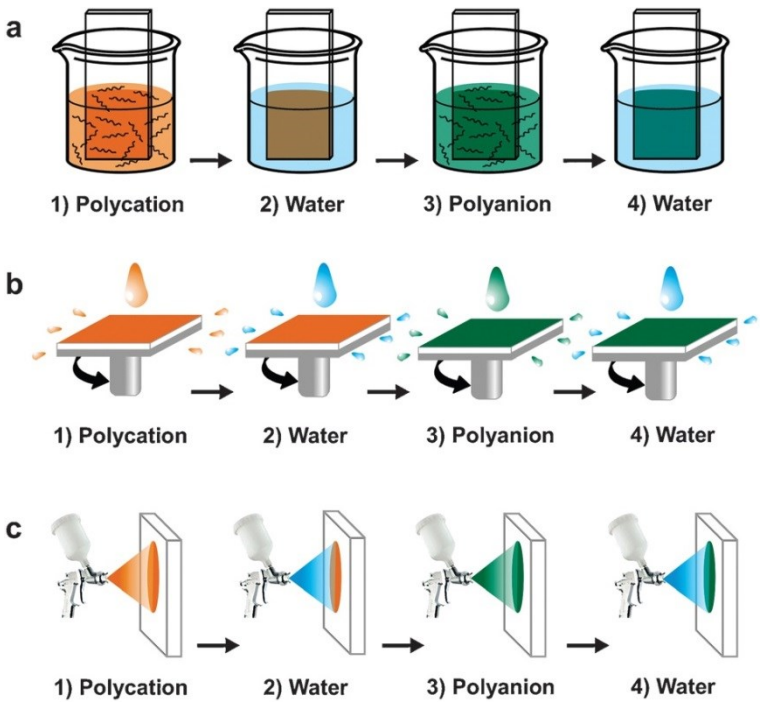

Figure 1.6. Schematic illustration of the LbL assembly with (a) dip-assisted, (b) spin-assisted, and (c) spray-assisted depositions. Reproduced with permission.[120] Copyright 2012, Royal Society of Chemistry.

First, dip-assisted LbL is the most widely used, conventional LbL technique. In dip-assisted LbL assembly, the film is constructed by alternately immersing the substrate

into oppositely charged polyelectrolyte or colloidal dispersions. The challenges are slow processing, solution contamination, limited scalability.[105, 121]

Spray-assisted LbL assembly technique can address these issues. In spray-assisted LbL assembly, films are fabricated via sequential spraying of oppositely charged polyelectrolytes or nanoparticle suspensions onto substrates.[121-122] The film deposition can be affected by several parameters including the concentration of spraying solutions, spraying time, rinsing, and air-blowing time.[122] This spray-assisted LbL assembly process can significantly reduce the processing time and constraints for materials and scale of substrates.[122] These advantages allow this assembly method to be used to fabricate films rapidly on relatively large and diverse substrates, broadening the processability of spray-assisted LbL assembly for industrial applications.[29, 122-123]

Another strategy is spin-assisted LbL assembly. Spin-assisted LbL assembly is the combination of spin coating and conventional LbL techniques.[103] In spin-assisted LbL assembly, the film is constructed by sequentially dropping cationic and anionic solutions onto a spinning substrate, and the thickness of the deposited layers can be controlled by solvent evaporation, spin speed, spin time, solute molecular weight, and solute concentration.[103, 124]

Specifically, these advantages make LbL assembly a promising method to fabricate electrode materials for energy storage system.[34] Well-controlled structure plays a critical role in electrochemical and mechanical performance of the nanostructured electrodes, which depends on the available active surface area for charge storage,

porosity for facilitating ion diffusion, and interconnectivity between the components for electrical conductivity and mechanical stress transfer.[34-35]

The LbL assembly process has been utilized for designing carbon-based nanostructured electrodes such as graphene and MWNT. It was reported that LbL assembled MWNT/chemically reduced graphene electrodes were designed for electrochemical micro-capacitor applications. The resulting LbL electrode showed high specific and volumetric capacitance arising from the controlled structure where MWNTs separate chemically reduced graphene sheets, providing the porous structure and larger electrochemically active surface area.[86] LbL-MWNT electrodes were fabricated by LbL assembly of functionalized MWNTs with carboxylic-acid and amine groups for lithium batteries.[125] The LbL-MWNT electrodes showed high energy and power density, which was attributed to the redox reaction of oxygen containing functional groups on the MWNTs by lithium ions and porous network structure of the electrodes.[125] LbL-MWNT electrodes on a porous carbon paper substrate was also fabricated using vacuum-assisted spay LbL assembly.[123] Vacuum-assisted spay LbL process enabled thick film fabrication in short processing time and exhibited excellent areal energy and energy retention capability.[123]

Besides all carbon-based electrodes, carbon materials can be blended with nanoscale conducting polymers using LbL assembly. PANI/RGO and PANI/MWNT LbL electrodes showed excellent electrochemical performance which was attributed to pseudocapacitive charge storage of PANI and intimate connection between the materials.[71, 126]

1.4.2 Vacuum-assisted filtration

Vacuum-assisted filtration technique is a powerful method for designing well-ordered, free-standing nanocomposite films. In vacuum-assisted filtration, a suspension containing all components of the composite is filtrated through a membrane under vacuum induced directional flow. During the process, the liquid passes through the membrane pores and the dispersed materials are accumulated on the membrane. As the filtration proceeds, accumulated materials on the membrane block the membrane pores and the filtration rate decreases, which enables the disordered components in the suspension to be uniformly ordered. This self-assembly technique can create highly ordered, homogenous self-supporting thin films, Figure 1.7.[12, 127]

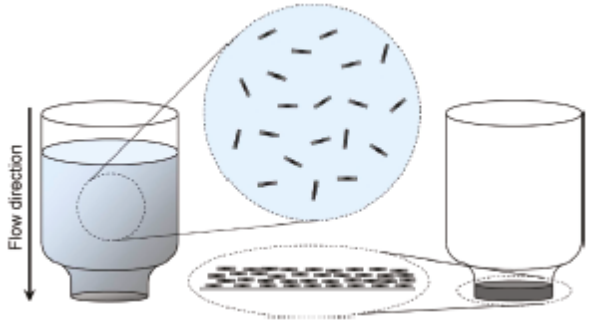

Figure 1.7. Schematic illustration of the vacuum-assisted filtration process. Reproduced with permission.[127] Copyright 2011. American Chemical Society.

Besides controlling the structure of the nanocomposites, the vacuum-assisted filtration process can control the film thickness by varying the concentration of the suspension and filtration volume. Also, the yield of the process is nearly 100 %,

independent of the components and substrates.[11] The vacuum-assisted filtration process has several advantages over other nanocomposite fabrication methods; a wide range of material selection, cost-effective and simple setup, and easy control of individual contents within the composite. [11-12]

In this regard, the vacuum-assisted filtration process is suitable for designing self-standing, highly layered graphene and graphene-based composite films. In the self-assembly process, the graphene or GO nanosheets can be adhered each other by attraction force such as van der Walls interaction, which makes the graphene or GO papers possess excellent mechanical properties through a brick-and-mortar structure.[127] The mechanical properties were enhanced by manipulating the interactions between the graphene nanosheets by intercalated solvents, ions, and nanofillers, forming non-covalent, hydrogen bonding and chemical interaction. [128-130]

Graphene and graphene-based composite papers fabricated by vacuum-assisted filtration have shown great potentials as free-standing, flexible electrodes. There have been considerable efforts to develop the graphene and graphene composite electrodes by optimizing the nanostructure of graphene electrodes. It was reported that solvated graphene paper electrodes fabricated by vacuum-assisted filtration for supercapacitors exhibited excellent electrochemical performance due to increased surface area.[9] Further, the electrochemical performance of graphene paper electrodes has been improved when combined with other guest materials including conducting polymers, transition metal oxides, and CNTs by manipulating the nanoarchitectures of the electrodes using vacuum-assisted filtration.[75, 83, 131]

1.5 Thesis Overview

In this thesis, graphene-polymer composite electrodes for structural energy and power system are designed and fabricated using different processing techniques.

In Chapter II, electrodes containing polyaniline nanofibers (PANI NFs) and electrochemically reduced graphene oxide (ERGO) sheets are demonstrated. The PANI NF/ERGO electrodes are successfully fabricated using spay-assisted LbL assembly of the two anisotropic nanomaterials. The water-based spray-on approach reveals that the electrodes can be seamlessly integrated into various substrates, indicating the adaptability and flexibility of this fabrication approach. The architecture and electrochemical performance are examined and compared against control electrodes made by dip-assisted LbL assembly. The spray-assisted LbL electrodes exhibit more porous structure. It is found that spray-assisted LbL assembly shows over 70 times faster film growth rate and yields electrodes with better rate capability relative to dip-assisted LbL assembly.

To design mechanically robust nanocomposite electrodes, newly emerging structural material, ANFs are introduced into multifunctional composites as reinforcing building blocks. The dispersible nature of ANFs enables its use in facile solvent-based processing systems such as LbL assembly and vacuum-assisted filtration for creating multifunctional composites. In Chapter III, ANFs and GO sheets are blended using dip-assisted LbL assembly, followed by thermal and chemical reduction. The resulting RGO/ANF films exhibit an ANF-rich structure where ANFs act as a polymer matrix that interfacially interacts with RGO sheets by hydrogen bonding and π-π interactions. It is

shown that the RGO/ANF films consist of 75 wt% ANFs and 25 wt% GO sheets. The RGO/ANF LbL electrodes shows capacitive charge storage behavior and chemical reduction leads to a higher areal capacitance than thermal reduction. Nanomechanical testing shows that the electrodes have a modulus intermediate between the two native materials, GO sheets and ANFs. No cracks or defects are observed upon flexing GO/ANF films 1000 times, whereas a GO control shows extensive cracking. These results demonstrate that electrodes containing ANFs and RGO sheets are promising for flexible, mechanically robust energy and power.

In Chapter IV, free-standing, high-strength composite supercapacitor electrodes consisting of RGO sheets and ANFs fabricated by vacuum-assisted filtration are demonstrated. These RGO/ANF composite paper electrodes exhibit extraordinary high tensile strength and excellent electrochemical stability, which is attributed to the incorporation of ANFs as reinforcing nanofillers into the system where RGO sheets are interconnected with ANFs by extensive non-covalent interfacial interactions. In addition, the tradeoff between capacitance and mechanical properties is evaluated as a function of ANFs loading. The RGO/ANF composite electrodes show multifunctionality superior to that of other graphene-based supercapacitors, indicating excellent combination of both mechanical and electrochemical properties.

The conclusions and future directions for the structural electrodes are presented in Chapter V.

CHAPTER II

SPRAYABLE, PAINTABLE LAYER-BY-LAYER POLYANILINE NANOFIBER/GRAPHENE ELECTRODES[1]

2.1 Introduction

Structural energy and power, in which a battery or capacitor is seamlessly integrated into the object it powers, is receiving more and more attention. The general concept is to design a battery and its form factor around the device rather than *vice versa*. Spray-on approaches are particularly interesting in this regard because they offer large-area coverage onto complex surfaces.[4, 29, 123] It is desirable to use water as the spraying medium, as it limits the use of alternative volatile or costly solvents. To this end, it is critical to identify a water-based spray-on process that is suitable for anisotropic nanomaterials such as polyaniline nanofibers (PANI NFs) and functionalized graphene sheets, which are often investigated as electrode materials.

Polyaniline (PANI) is a p-type conjugated polymer, and has long been explored as a cathodic material for lithium metal and lithium-ion batteries and as a pseudocapacitive material for supercapacitors. PANI is an intrinsic conductor and is redox-active, storing charge through a reversible doping-dedoping mechanism.[27, 30, 83] PANI NFs, which tend to generate porous architectures, have been investigated as electrodes for electrochemical energy storage.[83, 132-137] Examples of such electrodes

[1]Modified and reprinted with permission from "Sprayable, paintable layer-by-layer polyaniline nanofiber/graphene electrodes" by Se Ra Kwon, Ju-Won Jeon, and Jodie L. Lutkenhaus, *RSC Advances* 2015, 5, 14994–15001, Copyright 2015, Royal Society of Chemistry

include PANI NF/V_2O_5, PANI NF/multiwall carbon nanotubes (MWNTs), and PANI NF/graphene.[30, 71, 83, 126, 138] This study focuses specifically upon water-processable PANI NFs, which are 30-50 nm in diameter and 100-500 nm long.[139] Their small size and stability in water renders them excellent candidates for spray-on processing.

Graphene is a two-dimensional carbon sheet, and has been considered a promising material due to its high electrical and thermal conductivities, mechanical strength, and specific surface area.[54, 58, 140] Graphene and graphene-based composite materials have been proposed for use in energy storage and generation devices such as batteries, supercapacitors, fuel cells, and solar cells.[57, 68, 141] It has been shown that the composite materials containing nanostructured graphene and conducting polymers can significantly improve the electrochemical performance due to their nanoarchitecture which provides increased surface area for charge storage and less diffusion limitation for ionic and electronic transport.[31, 34] However, pristine graphene sheets are challenging to suspend and process, especially in water. Instead, it is more practical to utilize graphene oxide (GO) sheets, which bear oxygen-containing functional groups in their basal plane and edges. GO sheets can be reduced chemically, thermally, or electrochemically to yield reduced graphene oxide (RGO).[59, 71, 142-143] Energy storage in RGO electrodes proceeds by both capacitive (electrical double layer) and pseudocapacitive (via remnant oxygen-containing functional groups) mechanisms.[57, 68, 75, 125, 144]

Thus, there have been great efforts to fabricate hybrid electrodes containing both PANI NFs and graphene via various methods such as *in-situ* chemical polymerization of aniline with graphene, vacuum filtration, and layer-by-layer (LbL) assembly.[32, 71, 83, 138,

[145-147] With the exception of LbL assembly, none of these techniques have proven suitable for large-area deposition via spraying or comparable methods.

LbL assembly is a powerful and versatile tool for the fabrication of multi-component hybrid electrodes. In LbL assembly, the film or electrode is fabricated via alternate exposure of a substrate to oppositely charged (or complementary) species from solutions or dispersions. Film properties such as thickness, composition, and structure can be precisely controlled by deposition conditions.[100] The LbL process has been utilized in the deposition of electrodes for batteries and supercapacitors. The motivation is that LbL assembly allows for molecular-level mixing of the adsorbing species, leading to synergistic effects between the two.[71, 143, 146, 148] Examples include PANI/MWNT, MWNT/graphene, MWNT/MnO_2, and MWNT/MWNT electrodes, for which dip-assisted LbL assembly was employed for all.[86, 118, 123, 126, 149] Dip-assisted LbL assembly relies upon immersion of the substrate, as compared to spraying of the substrate as is done for spray-assisted LbL assembly. The former approach has encountered challenges with slow processing, cross-contamination of baths, and cumbersome handling of large-scale substrates.[150] The latter process is faster, eliminates cross-contamination, and can be scaled up to large-area substrates.[29, 122-123, 150-151] Spray-assisted LbL assembly has been proposed for applications such as drug delivery, anti-reflection coatings, and light-emitting diodes.[152-154]

Recently, we reported on the fabrication of PANI NF/electrochemically reduced graphene oxide (ERGO) electrodes made via dip-assisted LbL assembly.[71] These electrodes performed quite well as cathodes in lithium metal batteries, but the dipping

process remains cumbersome. For the purposes of large-scale deposition and potential integration into flexible or complex substrates, we were motivated to assemble analogous electrodes via spray-assisted LbL assembly and compare their performance to their predecessor. To date, there exists only two reports on electrodes fabricated from spray-assisted LbL assembly including PANI NF/V_2O_5 and $MWNT^+$/$MWNT^-$ electrodes.[29, 145] To our knowledge, there are very few reports on spray-assisted LbL assembly with GO sheets, perhaps because they are somewhat difficult to assemble into a uniform film.[155-157]

Herein, we present PANI NF/ERGO electrodes fabricated via spray-assisted LbL assembly for the first time. These electrodes are formed by the alternate spraying of positively charged PANI NFs and negatively charged GO sheets. Best practices towards the spraying and assembly of these components is first presented, in which film growth is characterized by profilometry, quartz crystal microbalance (QCM), scanning electron microscopy (SEM), and Raman spectroscopy. Following assembly, the GO sheets are electrochemically reduced to ERGO to produce a PANI NF/ERGO electrode. The results of the electrochemical reduction step are presented, followed by the charge storage behavior of these electrodes in a nonaqueous half-cell with lithium as the anode (i.e., lithium metal battery). Results are compared to analogous electrodes made previously by dip-assisted LbL assembly.

2.2 Experimental Section

2.2.1 Materials

Aniline, ammonium peroxydisulfate, propylene carbonate, lithium perchlorate, potassium permanganate, sodium nitrate, and hydrazine were purchased from Sigma Aldrich. Li foil was purchased from Alfa Aesar. Linear polyethyleneimine (PEI, Mw ~25,000) and poly(acrylic acid) (PAA, Mw ~50,000, 25% aqueous solution) were purchased from Polysciences. Graphite (SP-1) was purchased from Bay Carbon. Indium-tin oxide (ITO)-coated glass (resistance <20 Ω/sq) and In_2O_3/Au/Ag-coated PET film (resistance <10 Ω/sq) were purchased from Delta Technologies. Microporous poly(propylene) separator (Celgard 3501) was provided by Celgard.

2.2.2 Preparation of PANI NF and GO dispersions

PANI NFs were synthesized using a rapid mixing approach.[139] Aniline (1.49 g, 16 mmol) was dissolved in 50 mL of 1 M HCl solution. Ammonium peroxydisulfate (0.915 g, 4 mmol) was dissolved in 50 mL of 1 M HCl solution. Both solutions were purged with nitrogen for 1 h at room temperature. Then, ammonium peroxydisulfate solution was rapidly mixed with aniline solution under nitrogen, and the mixed solution was stirred for 24 h at room temperature. After polymerization, the resulting deep-green PANI NF dispersion was dialyzed against deionized water for three days. For LbL assembly, the PANI NF dispersion was diluted to 0.5 mg/mL with deionized water, and the pH value was adjusted to 2.5.

Graphite oxide was synthesized using a modified Hummers method.[158] 3 g of graphite powder was put into cold, concentrated 120 mL of H_2SO_4. 2.5 g of $NaNO_3$ was added and stirred for 5 h in an ice water bath. Then, 15 g of $KMnO_4$ was gradually added to the mixture under stirring and cooling with ice so that the temperature of the mixture was kept below 20 ^oC. Then, the mixture was stirred at 35 ^oC for 2 h and diluted with 250 mL of cold deionized water. 700 mL of deionized water and 20 mL of 30 wt% H_2O_2 was added to the mixture, and the reaction mixture became brown in color. The mixture was washed with 5 wt% HCl solution and filtered. The filtered mixture was re-dispersed in deionized water and dialyzed. Graphite oxide power was obtained after the resulting dispersion was dried at 60 ^oC. The graphite oxide powder was dissolved in deionized water (0.5 mg/mL) and exfoliated via sonication to give GO sheets in dispersion.

2.2.3 Preparation of PANI NF/GO spray-assisted LbL films

PANI NF/GO spray-assisted LbL films were fabricated on ITO-coated glass using an automated spray-assisted LbL system (Svaya Nanotechnologies). ITO-coated glass substrates were cleaned via sequential sonication in dichloromethane, acetone, methanol, and deionized water for 15 min each. Then, the substrates were dried in a convection oven, followed by 5 min of oxygen plasma treatment (Harrick PDC-32G). For LbL assembly, two layer pairs of PEI and PAA were sprayed onto the clean substrates as base-layers. 20 mM of PEI in water (pH 4) was sprayed for 10 s, followed by rinsing with water (pH 4) for 10 s. The same processes were then carried out with 20 mM of PAA in water (pH 4) and rinsing as before. After the base-layers were deposited,

PANI NF/GO spray-assisted LbL films were fabricated. The PANI NF dispersion (0.5 mg/mL, pH 2.5) was sprayed onto the substrate for 10 s, followed by blow-drying with air, then the GO dispersion (0.5 mg/mL, pH 3.5) was sprayed for 10 s, followed by blow-drying. The above procedure was repeated to achieve the desired number of layer pairs. The dispersions and blown air were applied with regulated pressure of 25 psi. Electrochemical reduction was carried out by holding the LbL film at 1.5 V vs Li/Li^+ in a three-electrode cell as described below.

2.2.4 Materials characterization

Thickness was measured using a profilometer (P-6, KLA-Tencor) from at least 10 selected points per sample and averaged. The mass density of the LbL film was measured using a quartz crystal microbalance (Maxtek-RQCM, Inficon). Raman spectra were recorded using a Raman spectrometer (Horiba Jobin Yvon). Morphologies of the LbL films were investigated using a field-emission scanning electron microscope (FESEM) (JSM-7500F, JEOL).

2.2.5 Electrochemical characterization

After the LbL films were fabricated, they were dried in air for 24 h and then under vacuum before electrochemical testing. Electrochemical properties were measured using either three-electrode cells or two-electrode sandwich cells. For the three-electrode cell, the spray-assisted LbL electrode on ITO-coated glass was used as the working electrode and two Li foils were used as counter and reference electrodes. As an

electrolyte, 0.5 M $LiClO_4$ in propylene carbonate (PC) was used. The two-electrode sandwich cell was comprised of the spray-assisted LbL electrode on ITO-coated glass as a cathode, Li foil anode, a poly(propylene) separator, and 1 M $LiClO_4$ in PC as the electrolyte. All electrochemical tests were performed using a potentiostat (SI 1287, Solatron) at room temperature in an argon-filled, oxygen- and water-free argon-filled glove box (MBraun). The average active area was 2.45 cm^2, and typical electrode masses were 1.2 $\mu g/cm^2$ with variations depending on the number of layers deposited.

2.3 Results and Discussion

Positively charged PANI NFs and negatively charged GO sheets were alternately sprayed from water-based dispersions onto ITO-coated glass slides. In spray-assisted LbL assembly, film deposition can be affected by several parameters including concentration, spraying time, rinsing time, and air-blowing time.[29, 121-122] For this present system, we found that rinsing and blow-drying times affect the quality of the film most significantly. Any amount of rinsing caused the films to delaminate and deconstruct. Figure 2.1a shows an example, where the film had deconstructed during growth, leaving behind patches of film. Accordingly, the rinsing step was eliminated in favor of blow-drying. An intermediate blow-drying time of 1 min was found to yield the most uniform films with steady LbL growth. Without blow-drying or rinsing, poor film growth was observed, Figure 2.1b. Blow-drying for 2 min resulted in uneven film growth, Figure 2.1c and 1d.

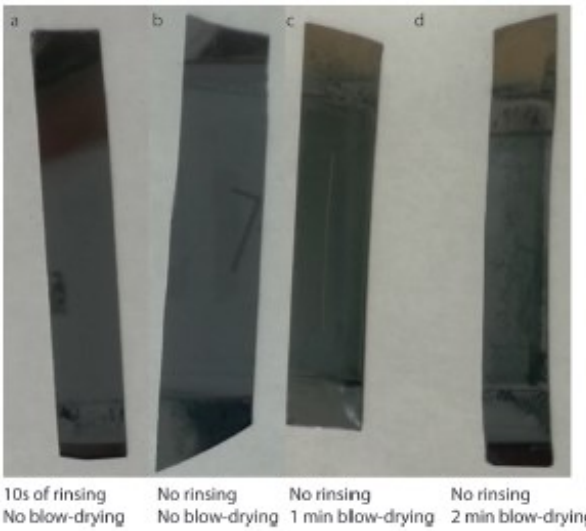

Figure 2.1. Digital images of PANI NF/GO LbL-coated silicon wafer pieces for which various spraying parameters were varied: (a) 10 seconds of rinsing and no blow-drying, (b) no rinsing and no blow-drying, (c) no rinsing and 1 min of blow-drying, and (d) no rinsing and 2 min of blow-drying. In cases (a) and (b), little to no film growth was observed. In case (d) the film was patchy and uneven. Case (c) yielded a uniform film and was selected for further study. The scratch in the film from case (c) was intentional as it was later used for profilometry.

The sensitivity of LbL film quality to rinsing and blow-drying times points to the importance of balancing processing vs adsorption timescales. Anisotropic materials require enough time to rotate, translate, and diffuse to the surface so as to adsorb at some favored orientation. During the spraying process the substrate's surface develops a wetted film, through which the adsorbing species must diffuse. Rinsing disturbs and renews the wetted film, removing non-adsorbed anisotropic nanoparticles. If the time

scale of spraying and rinsing is shorter than the time scale of the diffusion-adsorption process, then nanoparticle adsorption will be weak and poor films will result. On the other hand, blow-drying decreases the thickness of the wetted film, reducing the diffusion path and the timescale of adsorption.[29, 122]

Good-quality PANI NF/GO LbL films were constructed using the optimized spraying parameters (10 sec spraying and 1 min blow-drying for each layer), Figure 2.2a. The films were green in color and became darker with increasing number of layer pairs, indicative of an increase in thickness as assembly continued. The film thickness was measured using profilometry for various numbers of layer pairs, in which linear growth behavior was observed, Figure 2.2b. The average thickness per layer pair was 46 nm, which is comparable with the diameter of PANI NFs.[122] This value is suggestive of a single layer of PANI NFs laying parallel to the substrate, with GO sheets in between the PANI NF layers. Also, this layer pair thickness was much larger than that for films fabricated by dip-assisted LbL assembly (9 nm), which were proposed to exhibit patchy adsorption and well-mixed layers. The significant difference for spraying here is that the diffusion path is shorter than that of dipping, which possibly leads to enhanced adsorption of nanoparticles and greater layer pair thickness in sprayed films. This result leads to 74-fold enhancement of the growth rate for spray vs dip-assisted LbL assembly (0.29 nm/s vs 0.0039 nm/s, respectively).

The incremental mass adsorbed per layer was measured after each adsorption step using quartz crystal microbalance (QCM), allowing for an estimation of the composition. Similar to the trend in the thickness, the mass of the LbL film increased

linearly (1.25 μg/cm^2 per layer pair) as assembly continued, the mass of 100-layer pair film was 124.84 μg/cm^2. The composition of the film was approximately 67 wt% PANI NF and 33 wt% GO sheets, Figure 2.2c. From the area, thickness per layer pair, and mass per layer pair, the average density of the spray-assisted LbL films was calculated to be 0.4 g/cm^3, suggestive of a porous architecture. This value is lower than that of analogous films made by dipping (0.56 g/cm^3).[71] The void fraction of the spray-assisted LbL electrode was estimated to be 0.74 from the density of the composite electrode, polyaniline (1.329 g/cm^3), and GO sheets (2.2 g/cm^3).[68]

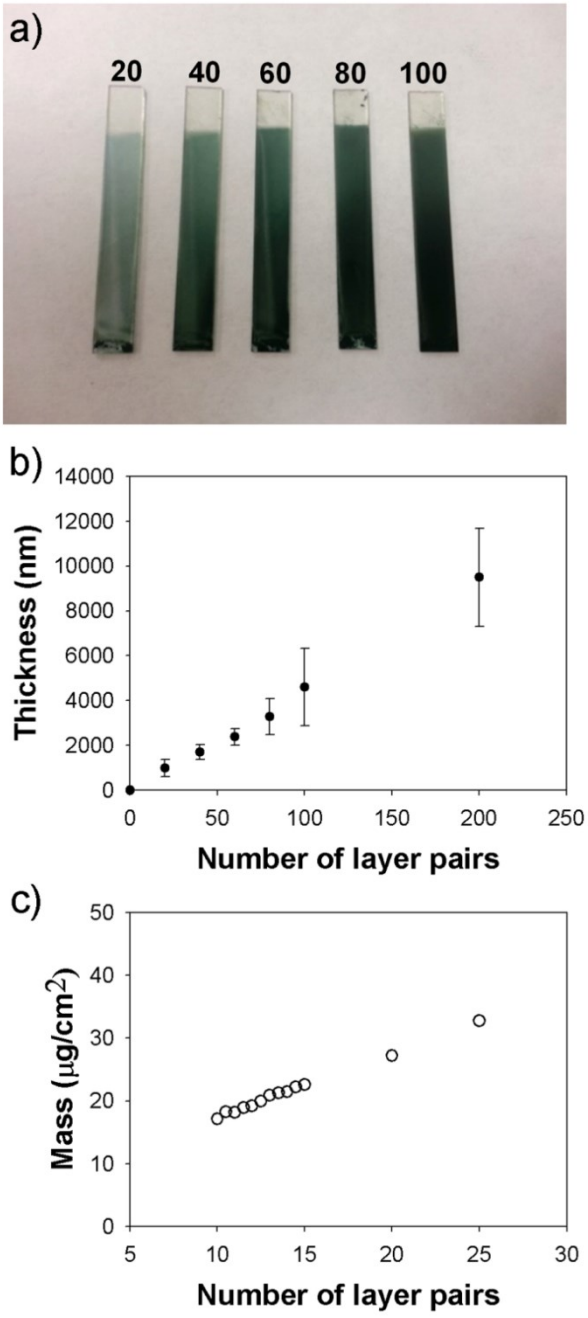

Figure 2.2. (a) Digital image of the PANI NF/GO spray-assisted LbL films with varying number of layer pairs. (b) Thickness and (c) mass of spray-assisted PANI NF/GO LbL films as measured using profilometry and QCM, respectively.

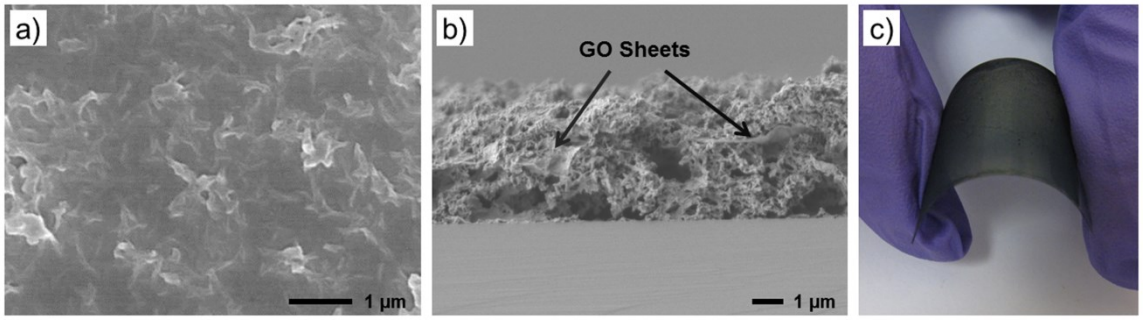

Figure 2.3. (a) Top-view and (b) cross-sectional-SEM images of PANI NF/GO spray-assisted LbL films, and (c) digital image of a PANI NF/GO spray-assisted LbL film coated onto a flexible PET substrate.

The morphology of the PANI NF/GO spray-assisted LbL film was investigated using SEM. Figure 2.3a shows a top-view SEM image of the PANI NF/GO spray-assisted LbL film, in which GO sheets comprised the outermost layer. The opaque regions are consistent with GO sheets, and the surface morphology of the film was rough probably due to the PANI NFs just below the GO sheets. In addition, a cross-sectional SEM image of the film confirmed the presence of both PANI NFs and GO, where the PANI NFs were sandwiched between GO sheets, Figure 2.3b.

To demonstrate the versatility of the process, the spray-assisted LbL technique was applied to a flexible conductive PET substrate, Figure 2.3c. The film did not display any obvious cracks or delamination during flexure. On the contrary, conventional dip-assisted LbL on the same substrate using PANI NFs and chemically RGO sheets was unsuccessful because of severe film delamination and aggregation. Thus, the spray-

assisted LbL process can address specific challenges found in dipping and can broaden the versatility and processability for the substrates and the depositing materials.

As-prepared PANI NF/GO spray-assisted LbL films were electrochemically reduced at 1.5 V vs Li/Li^+ in 0.5 M $LiClO_4$ in propylene carbonate for 10 h.[71] After electrochemical reduction, the color of the films changed from green to black, indicating that GO was reduced to ERGO, Figure 2.4a.[159] Electrochemical reduction was further confirmed using Raman spectroscopy. Figure 2.4b shows Raman spectra of PANI NF/GO spray-assisted LbL films before and after the electrochemical reduction, together with those from PANI NFs and GO sheets. PANI NFs show characteristic peaks at 1580 cm^{-1}, 1486 cm^{-1}, 1386 cm^{-1}, and 1166 cm^{-1}, which are assigned to C=C, C=N, and $C\text{-}N^{*+}$ stretching, and C-H in-plane bending, respectively.[126, 160] In GO's spectrum, the two main peaks observed were at 1335 cm^{-1} and 1590 cm^{-1}, corresponding to *D* and *G* bands, respectively. The *D* band is related to structural defects and disorder of carbon domains and the *G* band is assigned to sp^2-hybridized carbon structures.[71, 160] The presence of peaks from both PANI NFs and GO sheets in the spectra of the PANI NF/GO film confirms that both materials are incorporated into the film. The *D*/*G* intensity ratio increased for PANI NF/GO films upon electrochemical reduction from 0.94 to 1.07, which indicates that GO sheets within PANI NF/GO film were successfully reduced.[71, 147, 161]

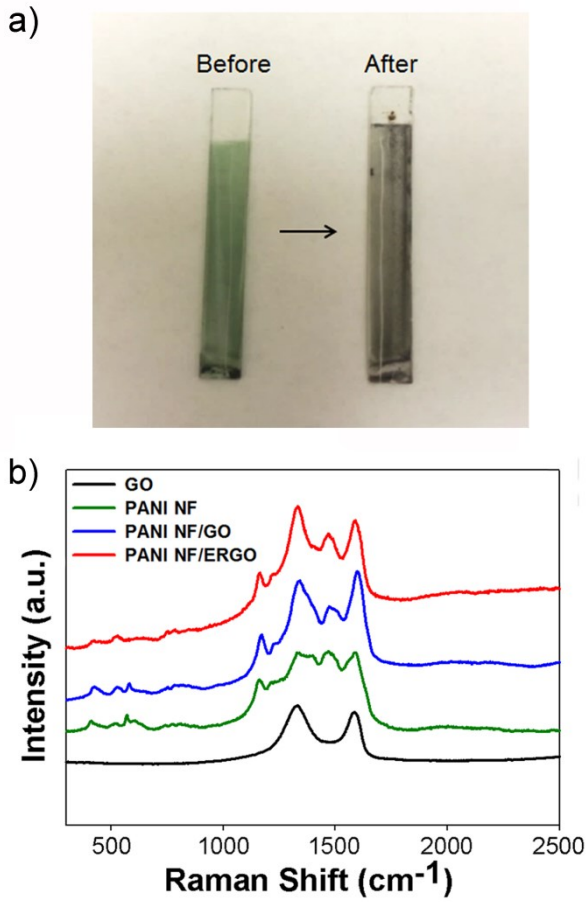

Figure 2.4. (a) Digital image of a PANI NF/GO spray-assisted LbL film before and after electrochemical reduction. (b) Raman spectra of PANI NFs, GO sheets, PANI NF/GO, and PANI NF/ERGO spray-assisted LbL films.

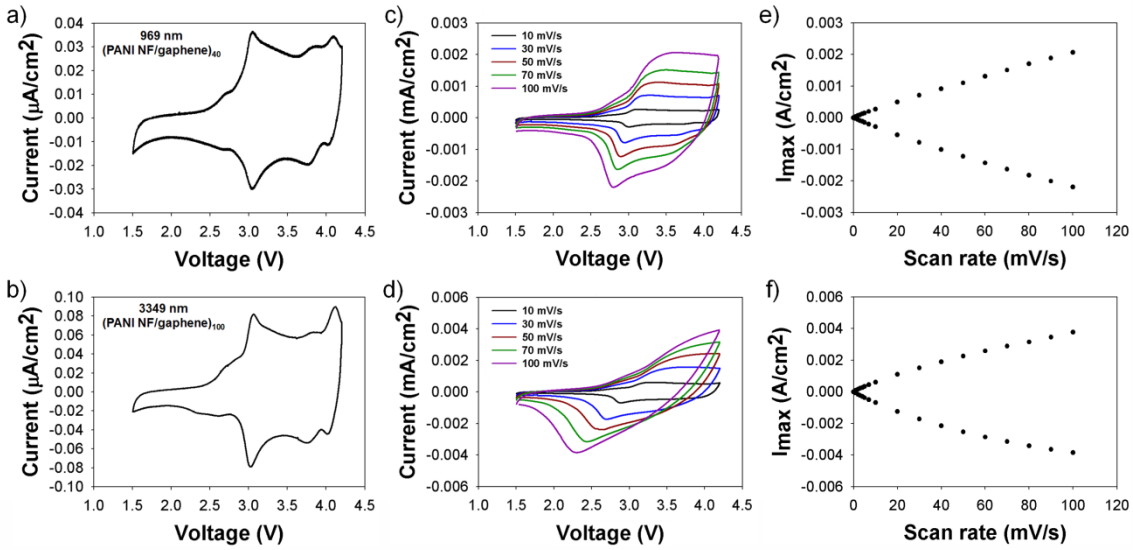

Figure 2.5. Cyclic voltammograms of PANI NF/ERGO spray-assisted LbL electrodes (a and b) at a scan rate of 1 mV/s and (c and d) at varying scan rates. (e and f) Plots of the maximum current vs scan rate. Panels (a, c and e) correspond to 40-layer pair electrodes (969 nm thick) and panels (b, d and f) correspond to 100-layer pair electrodes (3349 nm thick).

Having successfully obtained spray-on PANI NF/ERGO electrodes, we next turn to the investigation of their electrochemical properties. Cyclic voltammetry was performed using a three-electrode cell to compare the redox behavior of a 40-layer pair electrode (969 nm) against a 100-layer pair electrode (3349 nm). The electrolyte was 0.5 M $LiClO_4$ in propylene carbonate, and the counter and reference electrodes were separate lithium metal ribbons. The voltage range was 1.5-4.2 V vs Li/Li^+, and the scan rate was 1 mV/s, Figure 2.5a and 5b. Both electrodes displayed two distinct symmetric

pairs of anodic and cathodic peaks near 3 V and 3.8 V. The peaks are consistent with Faradaic redox reactions attributed to PANI NFs, and are assigned to leucoemeraldine/emeraldine and emeraldine/pernigraniline redox reactions, respectively.[30, 71] The symmetry of both pairs of peaks is indicative of the reversibility of the redox reaction and the lack of diffusion limitations for under the 1 mV/s scan rate.[29]

The results from cyclic voltammetry demonstrate that thinner electrodes are less susceptible to ion transport limitations as compared to thicker spray-assisted LbL electrodes. The increased distortion and shifted peaks associated with the thicker electrode are consistent with hindered diffusion of ions. On the other hand, the linear relationship of current with scan rate suggests that the redox reaction remains largely pseudocapacitive and surface-confined in nature.[71, 162-163] As compared to control electrodes made from dip-assisted LbL assembly, the extent of the transport limitation is much less for the sprayed electrodes, likely because they are more porous.[71]

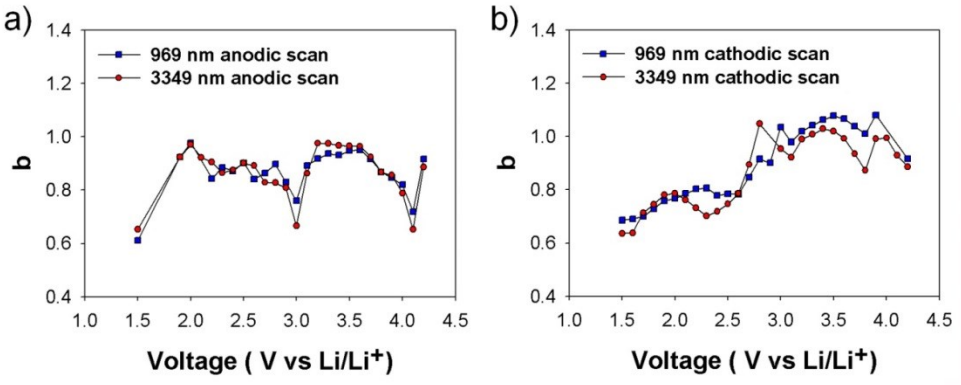

Figure 2.6. *b* values obtained from (a) anodic scans and (b) cathodic scans vs voltage for PANI NF/ERGO spray-assisted LbL electrodes of two different thicknesses. The *b* value was estimated from cyclic voltammograms shown in Figure 2.5, over a scan range of 10-100 mV/s. At a given potential the current *i* measured for each scan rate *v* was fit with adjustable parameters *a* and *b* using the function: $i=av^b$.

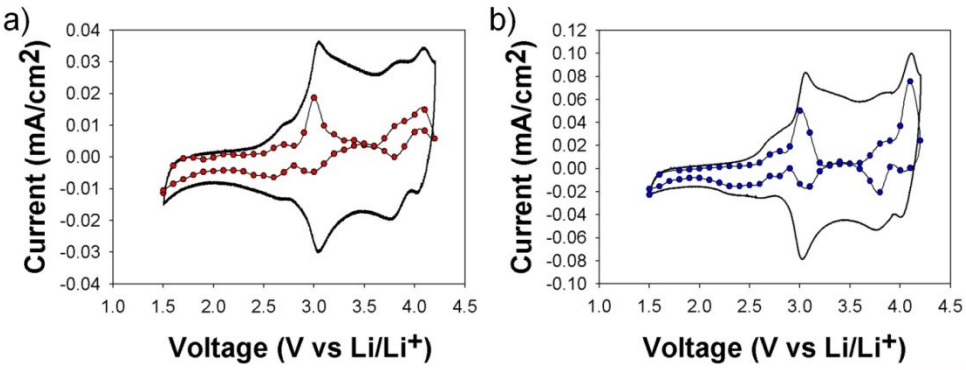

Figure 2.7. The diffusion-controlled contribution separated from cyclic voltammograms of (a) 969 nm and (b) 3349 nm thick $(PANI\ NF/ERGO)_{100}$ spray-assisted LbL electrodes at a scan rate of 1 mV/s. The diffusion-controlled contribution is taken as the second term in the following function: $i=a_1v+a_2v^{0.5}$. This function is fit to the cyclic voltammograms shown in Figure 2.5, over a scan range of 10-100mV/s.

To further understand the nature of charge storage in PANI NF/ERGO spray-assisted LbL electrodes, we performed an analysis of the cyclic voltammograms from Figure 2.5 such that processes related to diffusion-control and non-diffusion control could be quantitatively separated using a quantity *b*, Figure 2.6 and 2.7. This process is well described in our previous reports.[30, 71] The quantity *b* is equal to unity for non-diffusion control and equal to 0.5 for diffusion control. Both sets of LbL electrodes exhibited *b*-values of 0.8-1.0, and no distinct differences between thick and thin electrodes were observed. This value is supportive of a pseudocapacitive charge storage mechanism with slight diffusion control. On the other hand, *b*-values in comparable electrodes made via dip-assisted LbL assembly were strongly dependent on thickness, for which strong diffusion limitations arose in films even just 1520 nm thick.[71]

Galvanostatic charge-discharge testing was carried out to evaluate the electrochemical performance of the 100-layer pair electrode. Capacity, energy, and power are reported per gram of electrode (PANI NF + ERGO) or per cubic centimeter of electrode (apparent volume). Upon cycling between 1.5 and 4.2 V vs Li/Li^+, a sloping discharge profile was observed (Figure 2.8a). This profile is consistent with a pseudocapacitive charge storage mechanism, and is commonly observed for conjugated polymers.[27, 29]

Figure 2.8b exhibits the specific capacities of 60 and 100-layer pair sprayed electrodes. The 60-layer pair electrode was similar in thickness to a control electrode made by dipping, allowing for a suitable comparison. As the discharge current increased from 0.03 to 20 A/g, the specific capacity of the 100-layer pair sprayed electrode

decreased steadily from 114 to 34 mAh/g (45 to 14 mAh/cm^3). The capacity of the 60-layer pair remained fairly steady at 112 to 74 mAh/g. For a similar thickness, the capacity of a control made by dipping precipitously declined from 220 to 1.5 mAh/g as discharge current increased.[71] The spray-assisted LbL electrode clearly demonstrates a better rate capability as compared to dip-assisted LbL electrode, which we attribute to increased porosity brought about by the spray-assembly process. Accelerated cycling of the 100-layer pair spray-assisted LbL electrode showed an excellent capacity retention of 90% over 1000 cycles, Figure 2.8c.

The energy and power of the spray-assisted LbL electrodes were measured and summarized in Ragone plots based upon electrode mass and apparent electrode volume (Figure 2.9a and 2b). The highest specific energy was 346 mWh/g (138 mWh/cm^3) obtained at a discharge current of 0.1 A/g, and the highest specific power was 54090 mW/g (21640 mWh/cm^3) obtained at a discharge current of 20 A/g for the spray-assisted LbL electrode. Compared to dipped LbL electrodes of similar thickness, the sprayed electrode exhibited higher specific power at a given specific energy, confirming the enhanced rate capability of the sprayed LbL electrodes.

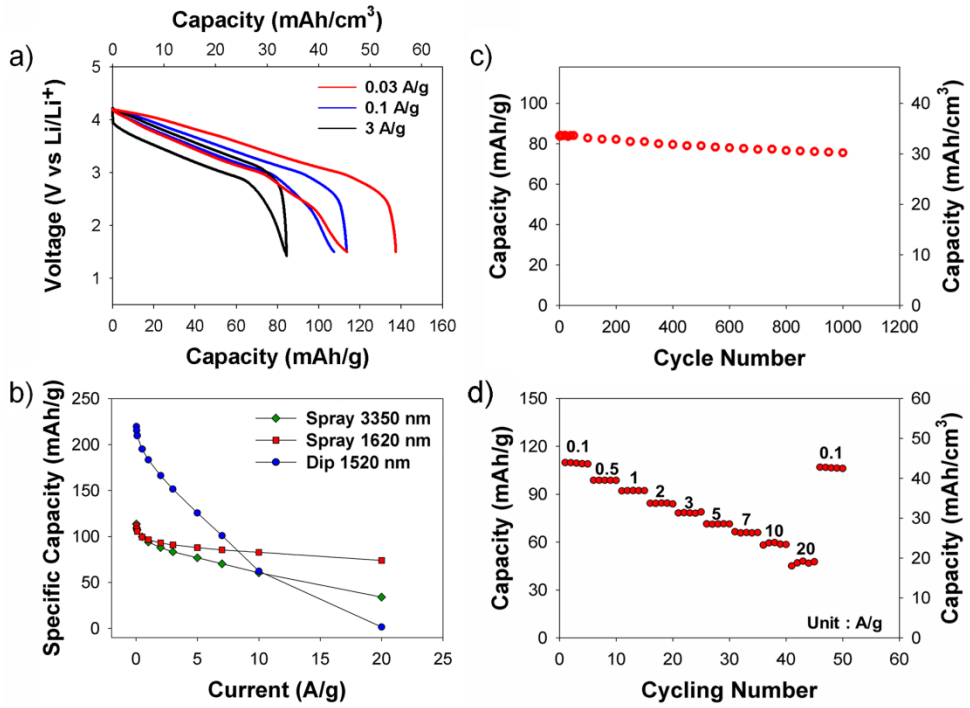

Figure 2.8. (a) Voltage vs specific capacity for a 100-layer pair PANI/ERGO spray-assisted LbL electrode at various discharge currents. (b) Specific capacity of a PANI-NF/ERGO dip-assisted LbL electrode compared to various PANI-NF/ERGO spray-assisted LbL electrodes vs discharge current. (c) Cycling behaviour of a 100-layer pair PANI/ERGO spray-assisted LbL electrode at 2 A/g. (d) Galvanostatic cycling of a 100-layer pair PANI/ERGO spray-assisted LbL electrode at varying discharge currents. Data from panels a–c were obtained using a three-electrode cell, and panel d from a two-electrode cell as described in the Experimental section.

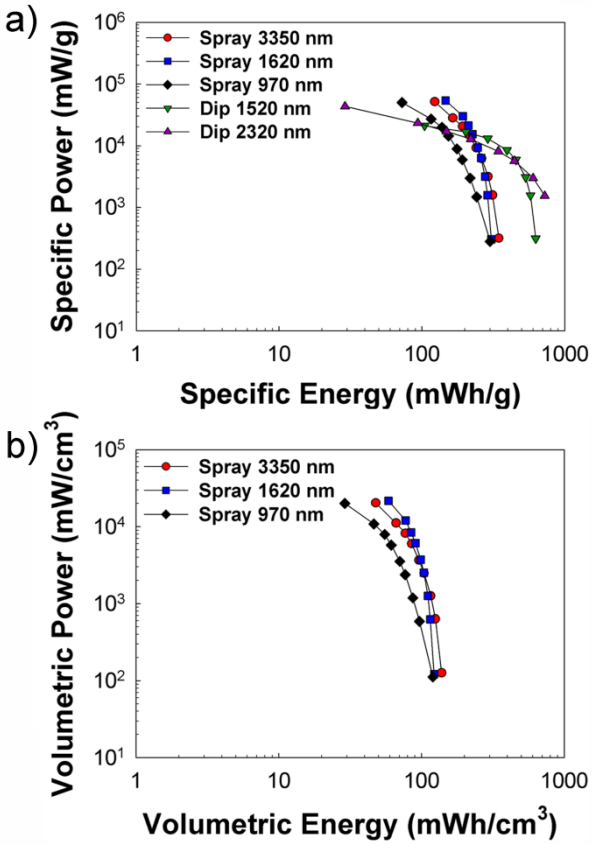

Figure 2.9. Ragone plots for various PANI NF/ERGO spray-assisted LbL electrodes based on (a) mass and (b) volume. Electrodes were evaluated in two-electrode cells from 1.5–4.2 V, where the anode was lithium metal and the electrolyte was $LiClO_4$ in propylene carbonate.

2.4 Conclusion

PANI NF/ERGO electrodes were successfully fabricated via spray-assisted LbL assembly of PANI NFs and GO sheets, followed by an electrochemical reduction step. Removal of the rinsing step and addition of a blow-drying step was critical toward the successful deposition of the two nanomaterials by spray. The PANI NF/GO spray-assisted LbL film exhibited linear film growth behavior (46 nm per layer pair), and the growth rate was 74 times faster than the analogous dipping process. This layer pair thickness was consistent with PANI NFs adsorbing in a single layer and laying flat against the substrate's surface. The spray-assisted LbL electrodes were less dense and more porous than those made from dipping. Compared with dip-assisted LbL electrodes, spray-assisted LbL electrodes exhibited an improved rate capability and a higher power at a given specific energy, which we attribute to enhanced porosity. The capacity, energy, and power reached values as high as 114 mAh/g (45 mAh/cm^3) at 0.03 A/g, 346 mWh/g (138 mWh/cm^3) at 0.1 A/g, and 54090 mW/g (21640 mW/cm^3) at 20 A/g, respectively.

The spray-assisted LbL process has proven itself to be a rapid fabrication method for the deposition of uniform electrodes onto a variety of substrates, even flexible PET. These sprayed or paintable electrodes, as demonstrated here, raise the prospect of LbL assembly as a versatile tool towards the formation of batteries onto objects of complex shapes for structural energy and power.

CHAPTER III

ROBUST AND FLEXIBLE ARAMID NANOFIBER/GRAPHENE LAYER-BY-LAYER ELECTRODES[1]

3.1 Introduction

With an increasing demand for flexible energy and power systems, considerable research efforts have focused on designing battery and capacitor electrodes that can withstand repeated mechanical deformation without loss of performance.[2, 164-167] To meet both mechanical and electrochemical needs, multi-functional hybrid materials are required. Graphene and graphene-based composites have been widely studied for use as electrode materials in energy storage devices such as batteries and supercapacitors.[57, 168-170] For supercapacitors, graphene stores charge by an electric double layer mechanism and by a pseudocapacitive mechanism with oxygen-containing functional groups at the surface.[58, 86, 171] In this regard, the combination of mechanically strong aramid nanofibers (ANFs) and graphene sheets is an attractive solution to develop flexible electrodes with high electrochemical performance. But, there remain questions as to how aramid nanofibers might affect the energy storage and mechanical properties of the graphene-based electrode.

Kevlar®, a para-aramid polymer synthesized from poly(paraphenylene terephthalamide) (PPTA), is well known for its superior mechanical properties and is a

[1]Modified and reprinted from "Robust and flexible aramid nanofiber/graphene layer-by-layer electrodes" by Se Ra Kwon, Meagan B. Elinski, James D. Batteas, and Jodie L. Lutkenhaus, *Submitted.*

promising candidate for reinforcing materials.[172] The impressive mechanical properties of PPTA, a modulus of 103 GPa and a tensile strength of 3.8 GPa, arise from interactions between PPTA chains, such as π-π stacking, van der Waals forces, and hydrogen bonding.[88-89, 172] However, the closely-packed structure renders PPTA relatively inert, which has limited its processability and incorporation into composite materials.[89, 173] Significant efforts to improve the interactions between PPTA and other materials, such as hydrolysis and surface coating, have been undertaken.[89-94] A recently developed method that produces nanoscale PPTA fibers (aramid nanofibers, ANFs) provides a simpler alternative to such processing issues. In this method, macroscale bulk Kevlar® thread is split into nanoscale aramid fibers through dissolution in dimethyl sulfoxide (DMSO) with potassium hydroxide (KOH).[172] During the process, ANFs form by the deprotonation of the amide groups, leading to the dissociation of hydrogen bonds between polymer chains.[172] The end product is a dispersion of polymeric nanofibers 20-40 nm in diameter and 5-10 μm in length with a negative surface charge.[89, 172] As a liquid dispersion, the ANFs can be utilized in various processing techniques such as layer-by-layer (LbL) assembly and vacuum-assisted filtration, amenable for a variety of applications where the mechanical properties are of interest.[98, 174-176]

Graphene, a two-dimensional material consisting of atomically thin sheets of sp^2-hybridized carbon, has attracted great attention due to its exceptional mechanical strength (modulus of 1100 GPa, fracture strength of 130 GPa), high thermal conductivity (5800 W/m·K), and large specific surface area (2630 m^2/g).[53-54, 177] These unique

properties allow graphene to be incorporated into nanocomposite materials for electronics, surface coatings, energy storage, and reinforcement.[168, 178-179]

There have been several reports on composite materials containing ANFs and graphene or graphene-derivatives fabricated by various methods such as vacuum-assisted filtration, non-covalent functionalization, and LbL assembly.[97-98, 174] Flexible ANF/graphene nanocomposite paper made by vacuum-assisted filtration exhibited a high Young's modulus (29.6 GPa) and tensile strength (209.4 MPa).[98] ANF/carbon nanotube (CNT) paper assembled through vacuum-assisted LbL processing showed high mechanical performance, with a Young's modulus of 35 GPa and an ultimate tensile strength of 383 MPa.[176] It was also reported that ANF-functionalized graphene sheets used as nanofiller for polymer reinforcement increased the Young's modulus by 70.6 % and the tensile strength by 84.5 % of a poly(methylmethacrylate) composite with only 0.7 wt% filler.[97] Elsewhere, surface coating via LbL assembly of graphene oxide (GO) and ANFs on glass fiber fillers enhanced the interfacial shear strength by 39 % between the filler and the epoxy matrix.[174]

LbL assembly is a powerful technique for the fabrication of multi-component hybrid films in which the film is fabricated via the alternate exposure of a substrate to the desired polyelectrolyte solution or colloidal dispersion. Film properties such as thickness, composition, and structure can be precisely controlled by deposition conditions.[100] LbL assembly usually is facilitated by electrostatic interactions, hydrogen bonding, and van der Waals forces between materials.[100, 107, 180] It has been shown that LbL assembly affords nanoscale organization for hybrid films with ordered, uniform

layers.[176, 181-183] This structure allows for increased interfacial contact between the polymer and the nanomaterial for better stress-transfer and charge storage, demonstrating how the nanoarchitecture of the film plays a significant role in the mechanical and electrochemical performance.[34] For example, poly(ethylene oxide) (PEO)/ANF LbL films were used as a thermally stable dendrite-suppressing ion conductor for lithium batteries due to the film's high modulus.[175]

Here, we report supercapacitor electrodes comprised of reduced graphene oxide sheets and aramid nanofibers made by LbL assembly for the first time. We examine how the inclusion of ANFs affects energy storage, modulus, and flexibility in relation to the resulting LbL structure. GO/ANF LbL films were constructed by the alternate deposition of GO sheets and ANFs facilitated by hydrogen bonding and π-π interactions and were reduced by various methods. Here, the LbL assembly technique is selected because it offers conformal deposition of electrodes onto various surfaces and because of the good interfacial contact between the ANFs and reduced GO sheets, allowing for the potential integration of batteries or capacitors into everyday objects.

3.2 Experimental Section

3.2.1 Materials

Kevlar® 69 was purchased from Thread Exchange. Dimethyl sulfoxide (DMSO), poly(diallyldimethylammonium chloride) (PDDA, Mw 200,000~350,000, 20% aqueous solution), propylene carbonate, lithium perchlorate, potassium permanganate, and sodium nitrate were purchased from Sigma Aldrich. Graphite (SP-1) was purchased

from Bay Carbon. Potassium hydroxide was purchased from Amresco. Lithium foil and hydrazine monohydrate were purchased from Alfa Aesar. Indium-tin oxide (ITO)-coated glass (resistance <20 Ω) and ITO-coated PET substrate (resistance = 10 Ω) were purchased from Delta Technologies.

3.2.2 Preparation of aramid nanofiber and graphene oxide dispersions

1.0 g of bulk Kevlar® 69 and 1.5 g KOH were added into 500 mL of DMSO and magnetically stirred for 7 to 10 days at room temperature.[172] After stirring, a dark red ANF/DMSO dispersion was obtained. Graphite oxide was synthesized using the modified Hummers method.[158] 3 g of graphite powder was added to 120 mL of cold, concentrated H_2SO_4. 2.5 g of $NaNO_3$ was added and stirred for 5 h in an ice water bath. Then, 15 g of $KMnO_4$ was gradually added to the mixture under stirring and cooling with ice so that the temperature of the mixture was maintained below 20 °C. After the addition, the mixture was stirred at 35 °C for 2 h, then diluted with 250 mL of deionized water while surrounded by an ice bath. 700 mL of deionized water and 20 mL of 30 wt% H_2O_2 was added to the mixture. During this reaction the color turned to brown. The mixture was washed with 5 wt% HCl solution and filtered. The filtrate was re-dispersed in deionized water and dialyzed to remove metal ions and acids. Graphite oxide power was obtained after the resulting dispersion was dried at 60 °C. The graphite oxide powder was added to deionized water (0.5 mg/mL) and exfoliated under ultrasonication to yield the graphene oxide dispersion.

3.2.3 Preparation and reduction of GO/ANF LbL films

GO/ANF LbL films were assembled on ITO-coated glass substrates and Si(100) substrates using an automated slide stainer (HMS series, Carl Zeiss). ITO-coated glass substrates were cleaned via sonication in dichloromethane, acetone, methanol, and deionized water for 15 min each. Then, the substrates were dried in a convection oven, followed by 5 min oxygen plasma treatment (Harrick PDC-32G). Silicon substrates were cleaned using basic piranha solution, followed by 5 min oxygen plasma treatment. For LbL assembly, a clean substrate was first dipped into a 1 wt% PDDA solution for 1 min and rinsed with water for 1 min. The positively charged substrate was then immersed in the GO dispersion (0.5 mg/mL, pH 3.5) for 1 min, rinsed twice with water (pH 3.5) for 1 min, then dried gently with low-velocity air. The substrate was then dipped into the ANF/DMSO dispersion (0.2 mg/mL) for 10 s, then rinsed with DMSO and water for 30 s and 1 min, respectively, before drying as before. The above procedure was repeated to achieve the desired number of layer pairs.

For thermally reduced GO/ANF LbL films (TRGO/ANF), as-prepared GO/ANF LbL films were annealed at 200 °C in vacuum for 2 h. For chemically reduced GO/ANF LbL films (CRGO/ANF), hydrazine vapor was used. As-prepared GO/ANF LbL films were placed in a small glass petri dish inside a larger petri dish to which 1 mL of hydrazine monohydrate 98% was added. The larger petri dish was covered with a lid, sealed with paraffin film, and placed over a hot plate at 40 °C for 18 h. The films were rinsed with water and dried at 80 °C under vacuum.

For LbL assembly on flexible, ITO-coated PET, the substrates were cleaned using 5 min oxygen plasma. GO/ANF LbL films were built up on the PET substrates following the same assembly procedure with the films fabricated on ITO-coated glass. For GO/PDDA LbL films as control, the PET substrate was immersed in 1 wt% PDDA solution and rinsed with water twice for 1 min, then dried. The substrate was dipped into GO dispersion (0.5 mg/mL, pH 3.5) for 1 min, then rinsed with water (pH 3.5) twice for 1 min, followed by drying. The procedure was repeated 20 times to yield 20 layer pairs GO/ANF and GO/PDDA LbL films.

3.2.4 Materials characterization

UV-vis absorption spectra of the LbL films was measured using a SolidSpec-3700 (Shimadzu). The thickness of the LbL films was measured using a profilometer (P-6, KLA-Tencor). The thickness was averaged from at least ten selected points of each sample. LbL films were characterized using Raman microspectroscopy (Horiba Jobin Yvon) with 514 nm excitation. X-ray photoelectron spectroscopy (XPS) analysis was performed using an Omicron ESCA Probe (Omicron Nanotechnology) with a monochromated Mg Ka radiation (hm = 1253.6 eV, 150 W, 15 kV). Survey scans were carried out with analyzer pass energy of 100 eV up to binding energies of 1100 eV (1.0 eV steps, 50 ms dwell time). High resolution scans of carbon (C1s) and nitrogen (N1s) were performed with a pass energy of 150 eV (0.05 eV steps, 200 ms dwell time). All spectra were calibrated with the C 1s photoemission peak for sp^2-hybridized carbons at 284.5 eV. Curve fitting of C1s and N1s spectra was done using a Gaussian-Lorentzian

peak shape after Shirley-type background correction. Given the XPS penetration depth (*ca.* 10 nm) and the layer pair thickness (1.2 nm), this samples about 8 layer pairs of material. Surface morphologies of the LbL films were investigated using scanning electron microscopy (SEM, JSM-7500F, JEOL) and atomic force microscopy (AFM, Agilent 5500) in tapping mode (Aspire CT170R silicon tips) and contact mode (Mikromasch CSC37 silicon tips) in a dry nitrogen environment (relative humidity 0.1%).

The nanomechanical properties of the GO/ANF LbL films were measured in a dry nitrogen environment by nanoindentation using an Agilent 5500 AFM. Silicon tips were obtained from MikroMasch (CSC37/ALBS), with a nominal spring constant of 1 N/m, individually determined *in situ* by the Sader method.[184] The radius of curvature of each tip used (*ca.* 12 nm) was determined experimentally (NioProbe standard, Aurora NanoDevices Inc.) by blind tip reconstruction using Scanning Probe Image Processing (SPIP) Software (Image Metrology, Denmark). AFM images were collected in contact mode under nitrogen at an applied load of 1 nN. Force-distance curves were taken with a maximum applied load of 15 nN. All images, force-distance curves, and related calculations were processed via SPIP.

Young's moduli were calculated based on the indentation of the LbL films as compared to an ideally hard SiO_2 reference (thermally grown SiO_2/Si(100) oxide film 90 nm in thickness, Young's modulus 72 GPa).[185] Force-distance curves with a maximum applied load of 15 nN were taken on the reference and LbL films, limiting the measurements to an indentation depth of *ca.* 10 nm, approximately 20% of the film

thickness, to avoid substrate contributions. The force-distance curves on the LbL films were collected in a grid array at 32 x 32 points over a 1 x 1 μm area (therefore reported values of Young's modulus, adhesion, and indentation depth are the averages and corresponding standard deviations from a total of 1,024 force-distance curves).

3.2.5 Electrical and electrochemical characterization

The electrical conductivity of the LbL films was measured using a four-point probe method (Keithley 2000 multimeter and 6221 DC and AC current source) with probe spacing 1.5875 mm at room temperature. The electrical conductivities, (σ, S/m) of the LbL films were obtained from the bulk resistivity (ρ, Ω·m) according to the relationship, $\sigma = 1/\rho$. The bulk resistivity of the LbL films was calculated by the following equation: $\rho = 4.532 \times (V/I) \times d \times f(a)$, where I(A) is the current applied by the current source, V (V) is the generated voltage, d (m) is the thickness of the LbL film, and $f(a)$ is a correction factor set to unity.

The electrochemical properties were characterized using a three-electrode cell, where the LbL film on an ITO-coated glass substrate was used as a working electrode and two Li foils were used as counter and reference electrodes. Propylene carbonate with 0.5 M $LiClO_4$ was used as the electrolyte. All electrochemical tests were performed using a potentiostat (Solatron 1287) at room temperature in an oxygen- and water-free, argon-filled glove box (MBraun). Cyclic voltammetry was conducted at varying scan rates from 5 to 200 mV/s in a voltage range of 2 to 4 V (vs Li/Li^+).

3.3 Results and Discussion

ANFs were prepared by the dissolution of macroscale Kevlar® fiber in DMSO with KOH.[172] The dissolution process occurred through the deprotonation of the PPTA's amide groups, which yielded a dark red dispersion of negatively charged ANFs. The ANF/DMSO dispersion was stable for several months, which was attributed to the balance of electrostatic repulsion between ANFs and π-π and van der Waals attractive interactions between PPTA chains. The diameter of the prepared ANFs was about 30-40 nm, and the length was about 5 - 10 μm, Figure 3.1a.

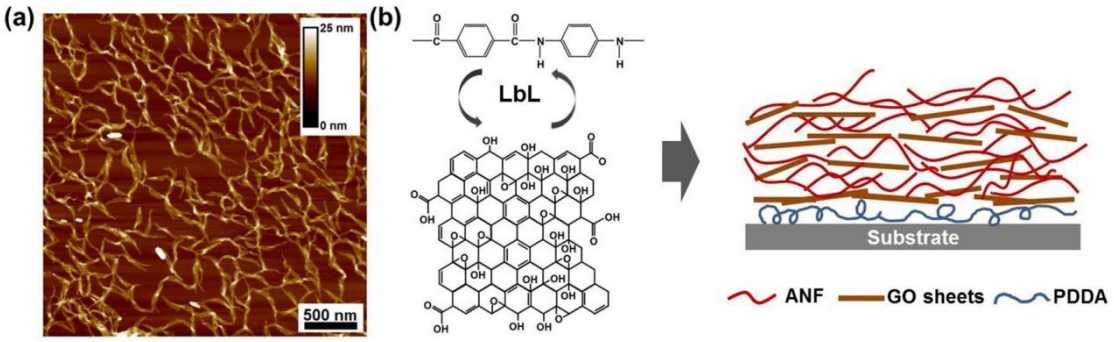

Figure 3.1. (a) AFM image of ANFs drop-casted on mica. (b) LbL assembly of ANFs and GO sheets.

The GO/ANF composite films were fabricated using an LbL dipping process, Figure 3.1b. Positively charged PDDA was deposited on the substrate as the first layer to promote LbL growth. Next, the substrates were immersed in the GO dispersion, followed by rinsing with water and blow-drying. GO sheets are expected to adsorb and adhere by electrostatic interactions with PDDA. Then, the substrates were immersed in

the ANF/DMSO dispersion, followed by rinsing with DMSO and water. Loosely adsorbed ANFs were removed during the DMSO rinsing step, and the water rinsing step re-protonated the negatively charged ANFs, which allowed for aromatic stacking and hydrogen bonding between the ANF chains, as well as the ANFs and GO sheets. Hydrogen bonding between ANFs and GO sheets takes place between GO –OH/–COOH groups and ANF –C=O groups, and/or between the GO –C=O/C-O groups and ANF –NH groups. The GO/ANF LbL films were light brown color, due to the GO sheets (Figure 3.2). The prepared LbL films are denoted as $(GO/ANF)_n$, where n is the number of layer pairs deposited.

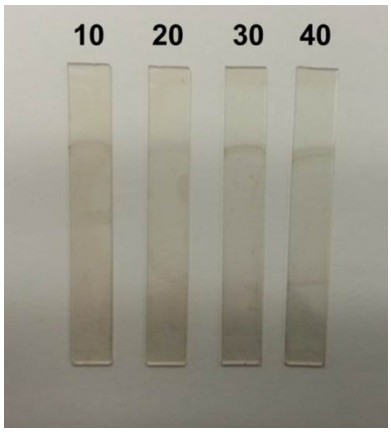

Figure 3.2. Digital image of GO/ANF LbL films on ITO-coated glass with 10, 20, 30, and 40 layer pairs.

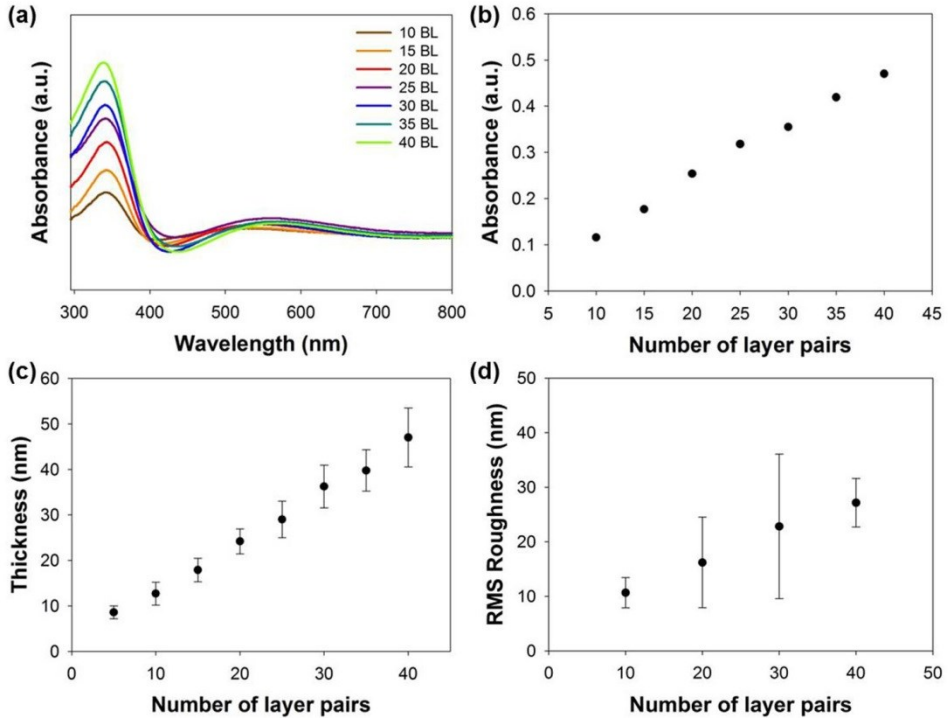

Figure 3.3. (a) UV-vis spectra of GO/ANF LbL films as a function of layer pairs or bilayers (BL). (b) Absorbance intensity at 335 nm as a function of the number of layer pairs. (c) Thickness and (d) RMS roughness of GO/ANF LbL films measured using profilometry.

The growth behavior of the GO/ANF LbL films was examined using UV-vis absorption spectroscopy and profilometry. The gradual increase in the UV-vis absorbance at 335 nm, a characteristic peak of the reprotonated ANFs, indicated linear growth of the GO/ANF LbL films with increasing number of layer pairs, Figure 3.3a and 3b.[97] The linear growth was also confirmed using profilometry, Figure 3.3c. The thickness of the $(GO/ANF)_{40}$ LbL film reached 48 nm with a layer pair thickness of 1.2

nm. This low cycle thickness indicates sub-monolayer adsorption of the components.[172] This growth rate is similar to that reported elsewhere for PDDA/ANF LbL films, which exhibited a1.6 nm layer pair thickness.[172] Further, the relatively large roughness of the LbL film demonstrates the randomly packed structure of the LbL films (Figure 3.3d). The root-mean-square (RMS) roughness of the $(GO/ANF)_{40}$ LbL film surface was 23 nm measured by profilometry and 10 nm measured by AFM. While the LbL films showed a rough structure on a larger length scale due to patchy growth, locally smoother structures were observed in AFM topographical images over a scan area of 5 x 5 μm.

The morphology of the GO/ANF LbL film was observed using SEM. Figure 3.4a and 4b shows surface SEM images of the $(GO/ANF)_{40}$ LbL film, where ANFs are the outermost layer. The magnified SEM image shows randomly distributed and entangled ANFs densely covering the film surface. GO sheets were not readily observable by top-down SEM. However, the structure of the GO sheets within the LbL film was further examined using AFM in tapping mode. Figure 3.4c and 4d shows AFM phase images (5 x 5 μm area) of the $(GO/ANF)_{35}$ and $(GO/ANF)_{35.5}$ LbL films, in which the outermost layers were ANFs and GO sheets, respectively. The dark regions are indicative of ANFs, which appear to be densely packed at the surface. The light regions are indicative of GO sheets laying flat on the surface. The results demonstrate the presence of both GO sheets and ANFs in the LbL films and show an ANF-rich structure with GO sheets intercalated between the ANFs. These images suggest that LbL assembly results in sub-monolayer deposition of GO sheets and tightly packed ANFs that fill the void, which partly explains the low growth rate.

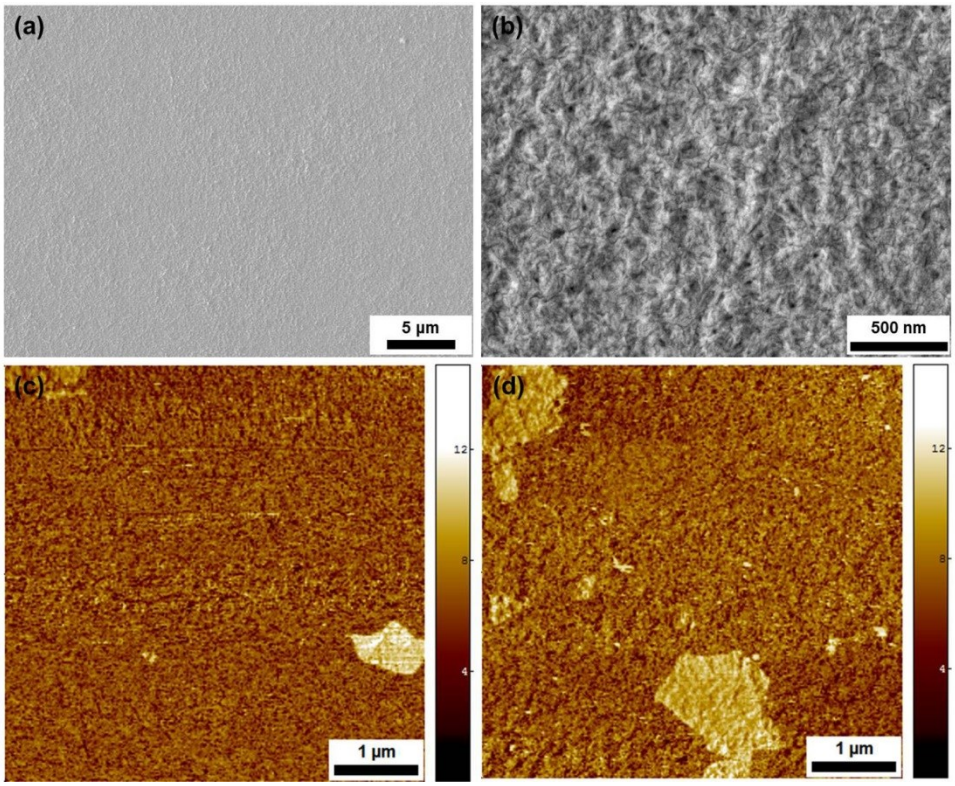

Figure 3.4. SEM images of $(GO/ANF)_{40}$ LbL films at (a) low and (b) high magnification. The top-most layer is ANFs. AFM phase images (5 x 5 µm) of (c) $(GO/ANF)_{35}$ LbL film, where the top-most layer is ANFs and (d) $(GO/ANF)_{35.5}$ LbL film, where the top-most layer is GO sheets (Phase range is 15°).

XPS analysis was used to gain insight into the surface composition and the intermolecular interactions between the GO sheets and ANFs within the assembled GO/ANF LbL films. Evaluating the atomic percentages from the XPS results (Table 3.1) allowed us to calculate the surface composition of the GO/ANF LbL films as 25 wt% GO sheets and 75 wt% ANFs. This suggests that the GO/ANF LbL films have an ANF-dominated structure, consistent with the morphology of the films observed in AFM and

SEM images. The C1s and N1s spectra of the ANFs and GO/ANF LbL films (Figure 3.5) allow for detailed analysis of the surface functional groups of the films. The peaks from the C1s spectra for ANFs were deconvoluted to: C-C (284.6 eV), C-N (286.1 eV), amide N-C=O (287.8 eV), and π-π interactions of aromatic phenyl groups (290.2 eV), Figure 3.5a.[173, 186] Further, in the C1s spectra for the GO/ANF LbL films, the peaks were deconvoluted to: sp^2-hybridized carbon (284.5 eV), C-N or C-O (286.1 eV), carbonyl C=O (286.7 eV), amide N-C=O (287.8 eV), carboxyl O=C-OH (289 eV), and π-π interactions (291 eV).[86, 187] For the LbL film, the π-π interaction peak around 291 eV was upshifted to a higher binding energy, indicating interactions between GO sheets and ANFs, Figure 3.5c.[188] The N1s spectra for ANFs and GO/ANF LbL films are shown in Figures 3.5b and 5d. In the spectra of the LbL composite film, Figure 3.5d, a new peak around 401.8 eV was observed, not present in the ANF spectra where only the amide N-C=O (399. 9 eV) peak is seen.[86] The new peak may arise from hydrogen bonding between the ANF amide groups with the oxygen-containing functional groups on GO sheets.[189] These results show that hydrogen bonding and π-π interactions stabilize the GO/ANF composite. These interactions should also lead to favorable mechanical properties.

Table 3.1. Summary of composition (atomic %) from XPS survey scans

	Not reduced	Chemically reduced	Thermally reduced
C	76.1	79.3	83.7
O	19.5	13.1	12.0
N	4.4	7.6	4.4
C/O	3.9	6.1	7.0

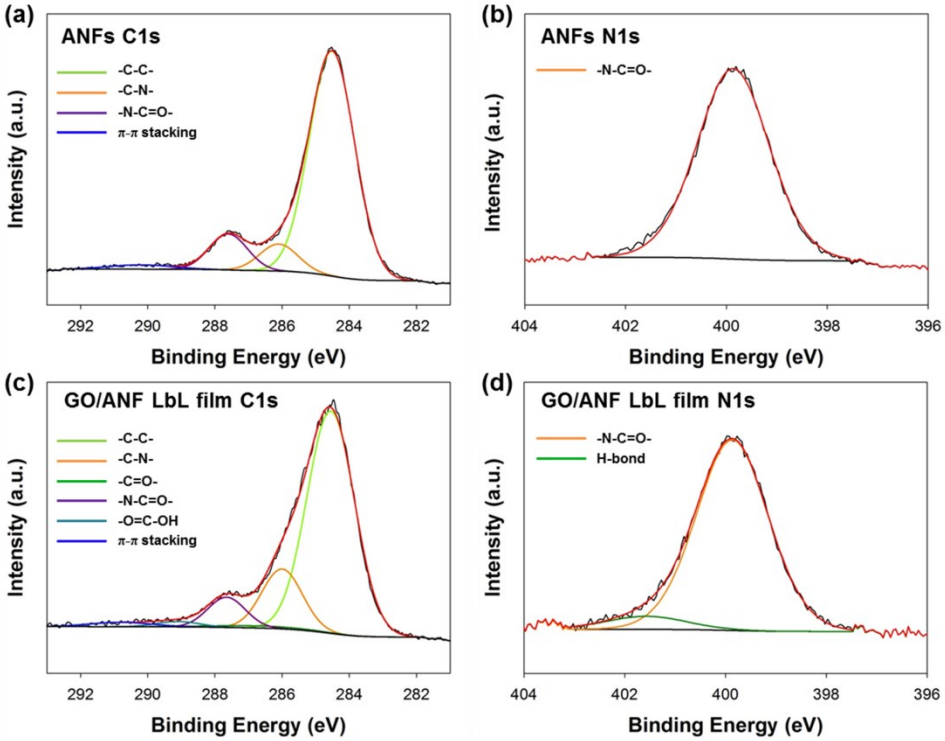

Figure 3.5. XPS C1s spectra of (a) ANFs and (c) (GO/ANF) LbL films. N1s spectra of (b) ANFs and (d) (GO/ANF) LbL films. The black curves are the original data and baseline, and the colored curves are the deconvoluted peaks.

To transform the GO/ANF LbL films into structural electrodes for supercapacitors, the as-prepared LbL films were reduced by two different methods. The first method was thermal reduction, in which the GO/ANF LbL films were annealed at 200 °C in vacuum for 2 h to yield TRGO/ANF LbL electrodes. The second method was chemical vapor reduction, where the GO/ANF LbL films were reduced under hydrazine vapor at 40 °C for 18 h to yield CRGO/ANF LbL electrodes. Attempts using solution-based chemical reduction with hydrazine and hydroiodic acid caused delamination and deconstruction of the LbL electrode. Further, hydrazine vapor reduction at high temperatures (80 °C) also damaged the film, creating cracks in the surface. It was found that hydrazine vapor reduction under relatively mild conditions (40 °C) could successfully reduce the LbL film without any delamination or cracking (Figure 3.6); therefore this method was employed over the other chemical options. After both chemical and thermal treatments, the color of the LbL films changed from light brown to black, indicative of reduction of GO to RGO, and the film thicknesses decreased by 13.6 % and 7.0 %, respectively.[63, 159] The reduction of GO was monitored using Raman spectroscopy and XPS. Figure 3.7 shows the Raman spectra of LbL films before and after reduction, compared to GO sheets and ANFs. The characteristics peaks of the ANFs arise from C=C stretching (1181, 1277, 1514, and 1610 cm^{-1}), C-H in-plane bending (1327 cm^{-1}), N-H bending/C-N stretching (1569 cm^{-1}), and C=O stretching (1648 cm^{-1}).[190] For the GO sheets, the characteristic D and G bands were observed at 1352 and 1595 cm^{-1}, respectively.[28] The D band (ring breathing) is related to the defective carbon structure and G band (in-phase vibration of the aromatic rings) arises

from the sp^2-hybridized graphitic carbon structure.[191] The presence of both GO and ANF peaks in the GO/ANF film confirms that both materials were incorporated into the LbL film. As shown in Figure 3.7, after reduction the D/G intensity ratio increased from 0.75 to 0.80 and 1.05 for thermal and chemical reduction, respectively. The increased D/G ratio comes from the smaller sp^2 graphitic domains, which were newly created upon reduction of GO, which should lead to enhanced electrochemical performance.[63]

The reduction of the GO sheets was also confirmed using XPS. The C/O atomic ratio of the GO/ANF LbL films obtained in the XPS survey scan was 3.9, vs a C/O ratio of 7.0 and 6.1 after thermal and chemical reduction, respectively. The increase of the C/O ratio for the reduced films is due to a decrease in the oxygen content within the LbL film. This decrease is assumed to be dominated by the thermal reduction of GO because ANFs do not decompose until around 500 °C.[172] For chemical reduction, the extensive hydrogen bonding between PPTA chains and GO sheets probably prevents chemical degradation of the ANFs. The increase in the C/O ratio appears low likely due to the high ANF content, which contributes to both C and O signals.[192] For CRGO/ANF films, a notable increase in the nitrogen content from 4.4 to 7.6 % was observed due to reaction of hydrazine with the oxygen functional groups on GO sheets.[86] TRGO/ANF LbL electrodes showed negligible changes in the nitrogen content.

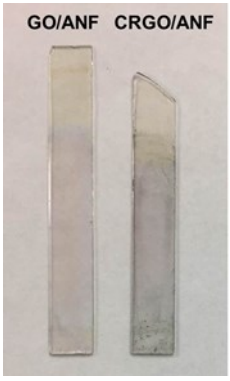

Figure 3.6. Digital image of $(GO/ANF)_{40}$ (before reduction) and $(CRGO/ANF)_{40}$ (after reduction) LbL films on ITO-coated glass.

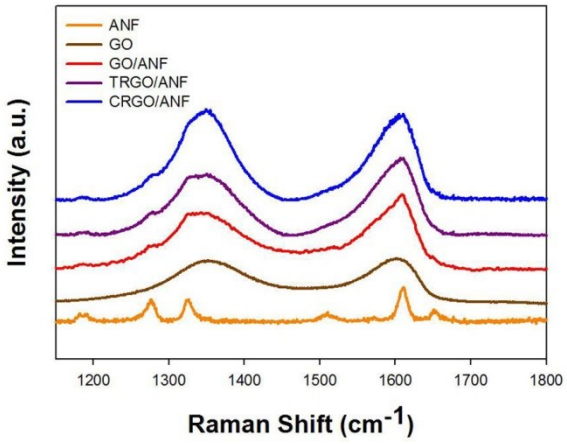

Figure 3.7. Raman spectra of ANFs, GO sheets, GO/ANF, TRGO/ANF, and CRGO/ANF LbL films.

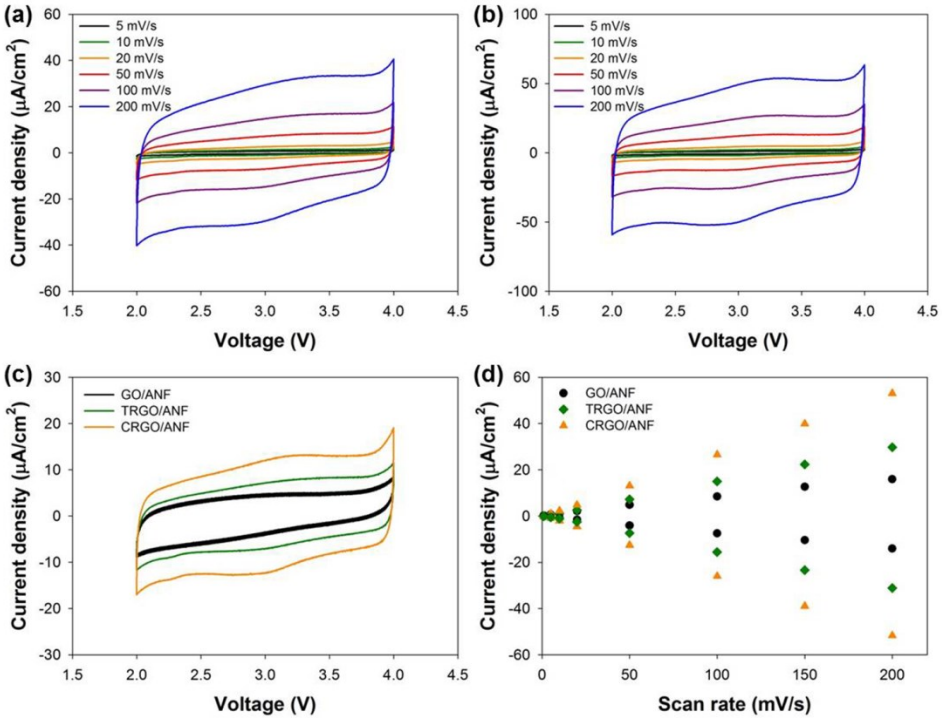

Figure 3.8. Cyclic voltammograms of (a) $(TRGO/ANF)_{40}$ and (b) $(CRGO/ANF)_{40}$ LbL films at varying scan rates, (c) cyclic voltammograms of $(GO/ANF)_{40}$, $(TRGO/ANF)_{40}$, $(CRGO/ANF)_{40}$ LbL films at a scan rate of 50 mV/s, and (d) plots of current at 3 V vs scan rate. Voltage is vs Li/Li^+ and the electrolyte was 0.5 M $LiClO_4$ in propylene carbonate.

After reduction, the electrochemical behavior of TRGO/ANF and CRGO/ANF LbL films was investigated using cyclic voltammetry (CV) using a three-electrode cell, where the working electrode was the LbL film and the counter and reference electrodes were separate lithium metal ribbons. The scan rate was varied from 5 to 200 mV/s over a voltage window of 2-4 V vs Li/Li^+, and the electrolyte was 0.5 M $LiClO_4$ in propylene carbonate.

Both $(TRGO/ANF)_{40}$ and $(CRGO/ANF)_{40}$ LbL films show fairly rectangular CVs, indicative of the capacitive behavior arising from the reduced GO sheets, Figures 3.8a and 8b, respectively.[58] The CV curves also show a broad shoulder around 3 V, attributed to pseudocapacitive charge storage arising from the remaining oxygen-containing functional groups on the surface of TRGO and CRGO sheets.[75, 86, 125] For comparison, Figure 3.8c plots CV curves for $(GO/ANF)_{40}$, $(TRGO/ANF)_{40}$, and $(CRGO/ANF)_{40}$ LbL electrodes at a scan rate of 50 mV/s. The chemically reduced LbL electrodes exhibited the highest areal current, followed by the thermally reduced electrode, and then the un-reduced electrode. From cyclic voltammetry, Figure 3.8d shows the current at 3 V plotted vs scan rate; the current increased linearly with scan rate, confirming a capacitive charge storage mechanism.[125] The electrode showed good wettability towards the electrolyte, having contact angles below 30^{o}, Figure 3.9.

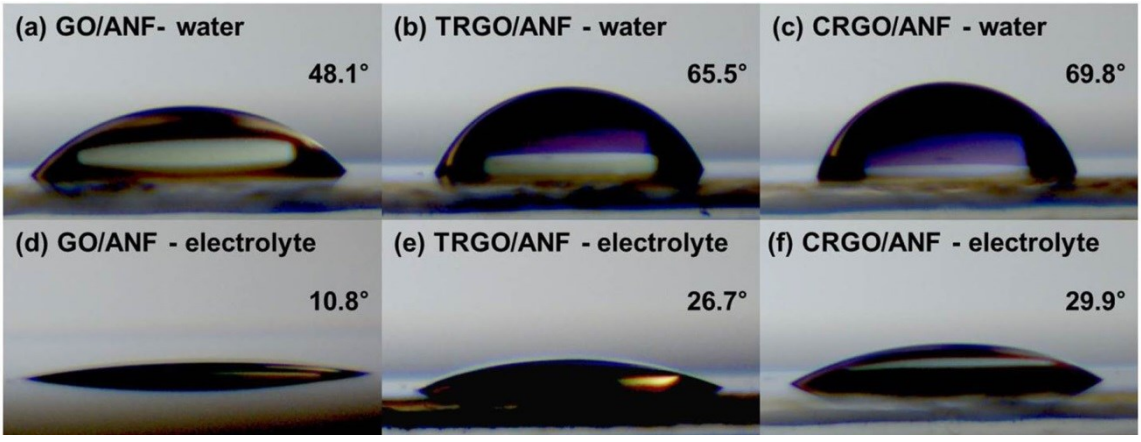

Figure 3.9. Contact angle images of water and 0.5 M $LiClO_4$ electrolyte on (a, d) GO/ANF film, (b, e) TRGO/ANF film, and (c, f) CRGO/ANF film.

For comparison, the areal capacitances were calculated from the CV curves at 50 mV/s, yielding 79.6 μF/cm^2 for the as-prepared GO/ANF, 112.5 μF/cm^2 for TRGO/ANF, and 195.5 μF/cm^2 for CRGO/ANF LbL electrodes. The highest capacitance observed was 221 μF/cm^2 for CRGO/ANF electrodes at a scan rate of 5 mV/s, corresponding to a volumetric capacitance 78 F/cm^3, Table 3.2. Electrodes of varying layer pair number or thickness were also examined, Figure 3.10, where it was observed that the current response and areal capacitance increased with the number of layer pairs as expected.

Table 3.2. Areal and volumetric capacitance of $(TRGO/ANF)_{40}$ and $(CRGO/ANF)_{40}$ electrodes.

Scan rate (V/s)	TRGO/ANF		CRGO/ANF	
	Areal (μF /cm^2)	Volumetric (F/cm^3)	Areal (μF /cm^2)	Volumetric (F/cm^3)
0.005	129	41.8	221	77.6
0.01	116	37.4	220	77.2
0.02	115	37.1	216	75.7
0.05	113	36.4	196	68.6
0.1	112	36.2	193	67.6
0.2	110	35.4	183	64.0

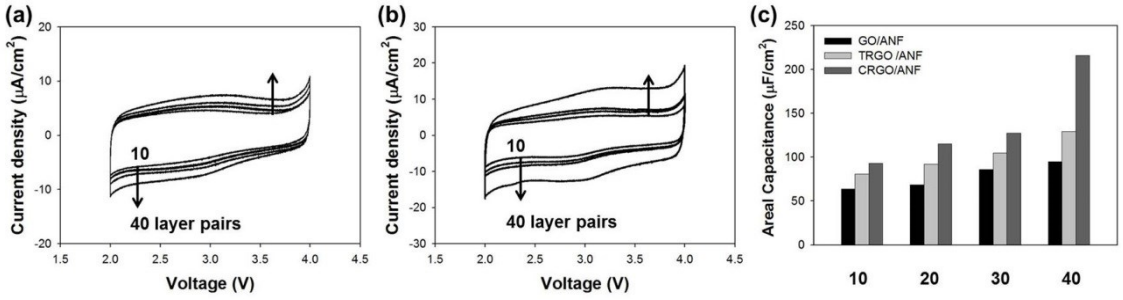

Figure 3.10. CV curves of 10, 20, 30, and 40 layer pairs of (a) TRGO/ANF LbL electrode and (b) CRGO/ANF LbL electrode at 50 mV/s. (c) Areal capacitance of GO/ANF, TRGO/ANF, and CRGO/ANF LbL electrodes in terms of the number of layer pairs. The number in the x-axis denotes the number of layer pairs of the film.

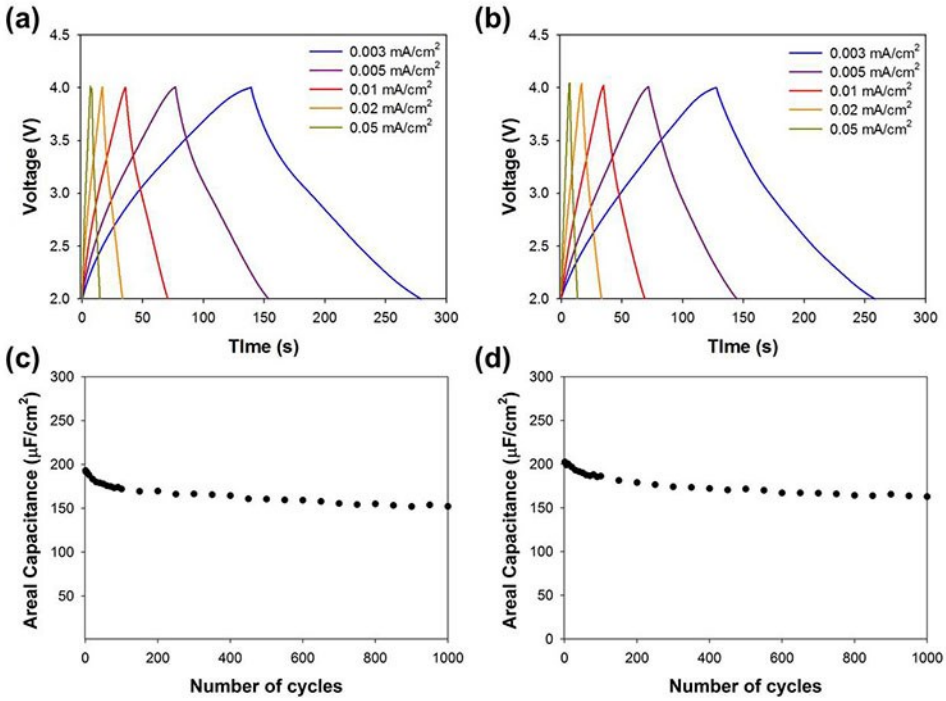

Figure 3.11. Galvanostatic charge/discharge curves of (a) $(TRGO/ANF)_{40}$ LbL electrode and (b) $(CRGO/ANF)_{40}$ LbL electrode, cycling behavior of (c) $(TRGO/ANF)_{40}$ LbL electrode and (d) $(CRGO/ANF)_{40}$ LbL electrode up to 1000 cycles at 0.005 mA/cm^2.

Galvanostatic charge/discharge testing was performed at different current densities from 0.003 to 0.05 mA/cm^2, Figure 3.11. The highest areal capacitance values were 196 μF /cm^2 (61 F/cm^3) and 212 μF /cm^2 (74 F/cm^3) at a current density of 0.003 mA/cm^2 for $(TRGO/ANF)_{40}$ and $(CRGO/ANF)_{40}$ electrodes, respectively. After 1000 cycles at 0.0005 mA/cm^2, both CRGO/ANF and TRGO/ANF electrodes maintained 80 % of their initial areal capacitance.

Examination of the volumetric capacitance provides some prospective on performance. The volumetric capacitances generally ranged from 78 to 35 F/cm^3 for

cyclic voltammetry and 51 to 74 F/cm^3 for galvanostatic cycling. This is relatively lower than the reported capacitances of thicker graphene electrodes (100-200 F/cm^3).[193-195] Comparing with other reports specific to LbL electrodes, the capacitances measured here are also lower.[196-198] This is most likely due to the low graphene content and its patchy adsorption during LbL assembly. The ANFs are not electrochemically active, so it is not surprising that the activity should be diminished; however, it should be noted that ANFs are critical to achieving mechanical robustness.

To complement findings regarding the capacitance, the electrical conductivity of the reduced LbL films was measured using a four-point probe method. It was generally difficult to obtain stable values for both types of reduced LbL films because of the low graphene content. Only for $(TRGO/ANF)_{40}$ LbL films was an averaged conductivity obtained (0.0044 S/m). This low content limits the connections between graphene sheets and reduces conductive pathways, in agreement with our findings on the composition and structure of these LbL electrodes.

Due to the low film thicknesses (~40 nm), AFM nanoindentation experiments were performed on five representative LbL samples and the individual film components (pure ANF and pure GO), to evaluate the nanomechanical properties of the LbL structures in comparison to the underlying substrate (ITO vs Si), film constituents (GO vs CRGO), as well as different film thicknesses and terminal layers. The samples tested were: $(GO/ANF)_{40}$ (ANF terminated, ITO substrate), $(GO/ANF)_{35}$ (ANF terminated, Si substrate), $(GO/ANF)_{35.5}$ (GO terminated, Si substrate), $(CRGO/ANF)_{35}$ (ANF

terminated, Si substrate), $(CRGO/ANF)_{35.5}$ (CRGO terminated, Si substrate), pure ANF, and pure GO.

By comparing the force-distance curves of the LbL films to the force-distance curves of an ideally hard SiO_2 reference, the indentation depth (δ) (Figure 3.12) can be used to estimate the Young's modulus (E_s) of each sample based on the Johnson, Kendall, Roberts (JKR) contact mechanics model.[185, 199-200] Assuming $E_s << E_{tip}$ (E_{tip}: Young's modulus of the AFM tip), E_s was calculated in SPIP using Equation (3.1-3) based on the contact area (a), reduced modulus of the contact (K), the Poisson ratio of the sample (ν_s, estimated as 0.33, with typical polymers in the range 0.2 – 0.5[29]), the applied load (L), the pull-off force (F_{adh}), and the tip radius of curvature (R_{tip}).

$$a = \left[\frac{R_{tip}}{K}\left(L + 2F_{adh} + \sqrt{4F_{adh}L + 2F_{adh}R_{tip}}\right)\right]^{1/3} \quad (3.1)$$

$$\delta = \frac{a^2}{R_{tip}} - \frac{4}{3}\sqrt{\frac{aF_{adh}}{KR_{tip}}} \quad (3.2)$$

$$E_s = \frac{3K\left(1-\nu_s^2\right)}{4} \quad (3.3)$$

To account for the surface roughness of the films, which in AFM nanomechanical experiments can cause the true tip-sample contact area to be overestimated, the RMS surface roughness (R_{surf}) was used to calculate the reduced radius of contact, R_{red}, Equation (3.4). Table 3.3 reports the average value and standard deviation for the pull-off force (taken as the tip-sample adhesion, F_{adh}), indentation depth (δ), and Young's modulus (E_s, at 15 nN indentation load and using R_{red}) of the samples.

$$R_{red} = \frac{R_{tip}R_{surf}}{R_{tip}+R_{surf}} \quad (3.4)$$

Table 3.3. Summary of nanomechanical measurements: average value and standard deviation of adhesion (F_{adh}), indentation depth (δ), and Young's modulus (E_s) measured at an indentation load of 15 nN.

Sample	F_{adh} (nN)	δ (nm)	E_s (MPa)
$(GO/ANF)_{40}$	6.0 ± 1.2	12.8 ± 0.9	146 ± 24
$(GO/ANF)_{35}$	6.8 ± 2.0	8.9 ± 0.8	258 ± 43
$(GO/ANF)_{35.5}$	5.3 ± 1.5	10.7 ± 0.7	206 ± 35
$(CRGO/ANF)_{35}$	6.1 ± 1.2	9.1 ± 0.6	286 ± 46
$(CRGO/ANF)_{35.5}$	4.8 ± 0.9	12.0 ± 0.9	159 ± 32
ANF	4.8 ± 1.4	23.9 ± 1.5	49 ± 10
GO	6.5 ± 0.7	7.1 ± 0.2	232 ± 41
polystyrene	8.6 ± 0.5	2.1 ± 0.1	1.8 ± 0.5 (GPa)

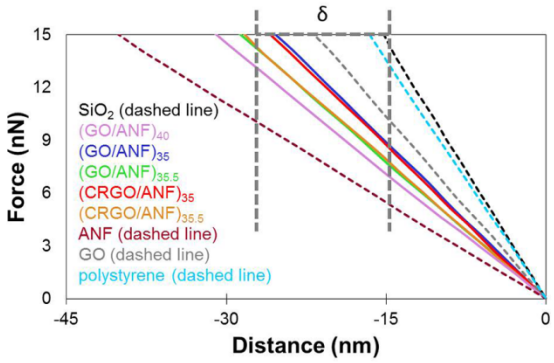

Figure 3.12. Representative force-distance curves for the LbL samples vs the SiO_2 reference. The indentation depth (δ) at 15 nN is indicated by the grey dashed line.

As seen in Table 3.3 the Young's modulus for each of the LbL films is *ca.* 200 MPa, with little variation in Young's modulus considering the standard deviation. This value is intermediate of the individual ANF and GO components, and shows no dependence on underlying substrate (ITO vs Si), chemical modification of the GO flakes (GO vs CRGO), or the outermost layer (GO/CRGO vs ANF).

In addition to comparing the Young's modulus across different samples, the spatial distribution of Young's modulus within a given sample was examined through maps generated from the grid-array collection of the force-distance curves. Figure 3.13 shows a 3D representation of the Young's modulus values at each point in the 32 x 32 grid over a 1 μm^2 area. Minimal variation in Young's modulus was observed for each sample. In particular, for the $(GO/ANF)_{35.5}$ sample, a region containing a GO flake (outlined by the white dashed line in Figure 3.14a-c) was located primarily by the friction force image (Figure 3.14b). A region containing a CRGO flake was also

identified for the $(CRGO/ANF)_{35.5}$ sample and is included in the Figure 3.15. While in the topography cross section of Figure 3.14a the GO flake is indistinguishable from the surrounding film, it was observed as a region of reduced in friction in Figure 3.14b, and there was a small difference in the adhesion map (Figure 3.14c) between the GO flake and ANF film (~1.5 nN lower pull-off force on the GO flake). However, there was no distinguishable difference in Young's modulus on vs off the GO flake (Note that Figure 13.4d is a 2D representation of the same data shown in Figure 3.13). The lack of visibility in topography, minimal difference in adhesion, and uniformity of Young's modulus across the GO flake suggests that the nanofibers could be wetting the GO flake, even in cases where the films were GO terminated. Similar results were obtained for the $(CRGO/ANF)_{35.5}$ sample, Figure 3.15.

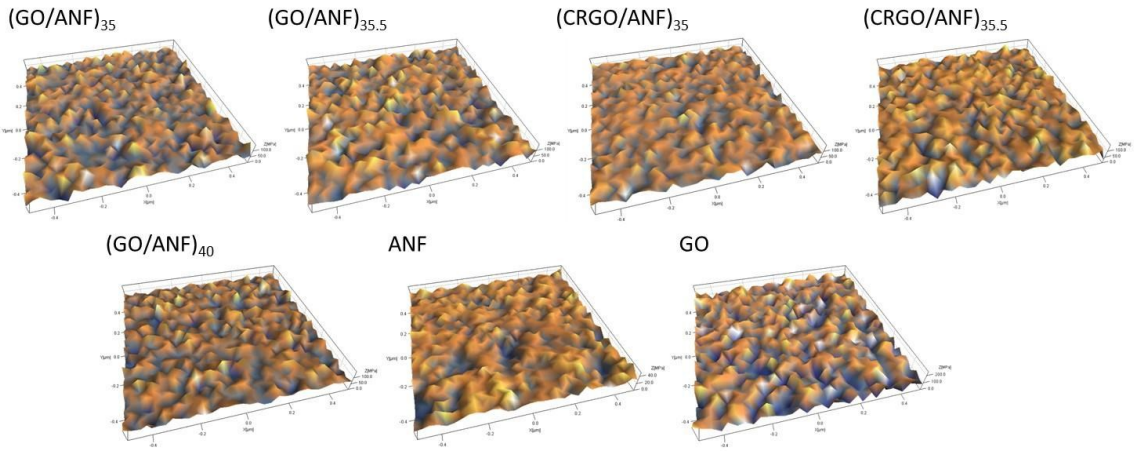

Figure 3.13. Three-dimensional images (1 x 1 μm) of Young's modulus for each sample generated from a 32 x 32 point grid of force-distance curves. For $(GO/ANF)_{35}$, $(GO/ANF)_{35.5}$, $(CRGO/ANF)_{35}$, $(CRGO/ANF)_{35.5}$, and $(GO/ANF)_{40}$ the z-scale is 150 MPa. For ANF the z-scale is 50 MPa, and for GO the z-scale is 250 MPa.

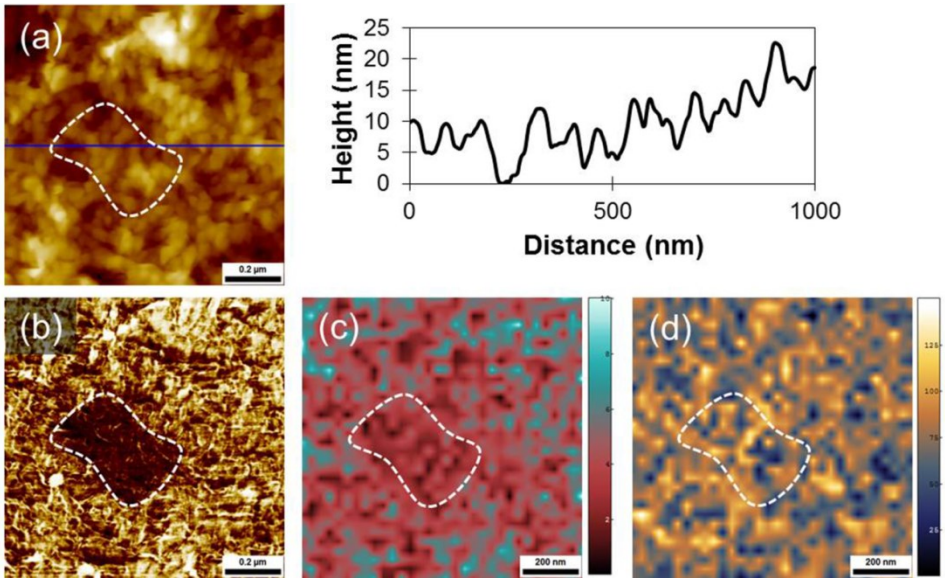

Figure 3.14. (a) Topography and corresponding cross section (1 x 1 µm) for a $(GO/ANF)_{35.5}$ LbL sample. (b) Friction force image taken simultaneously as (a). (c) Adhesion map (z-scale: 10 nN) taken simultaneously as (d) Young's modulus map (z-scale: 150 MPa). Note that (d) is a 2D representation of the same data shown in Figure 3.13 for the $(GO/ANF)_{35.5}$ sample. Most clearly visible in the friction image (b), a GO flake was located and is outlined by the white dashed line. The cross section of (a) shows that while the GO flake is indistinguishable from the morphology of the nanofibers, it is visible as a region of reduced friction (b) and lower adhesion (~1.5 nN) in (c).

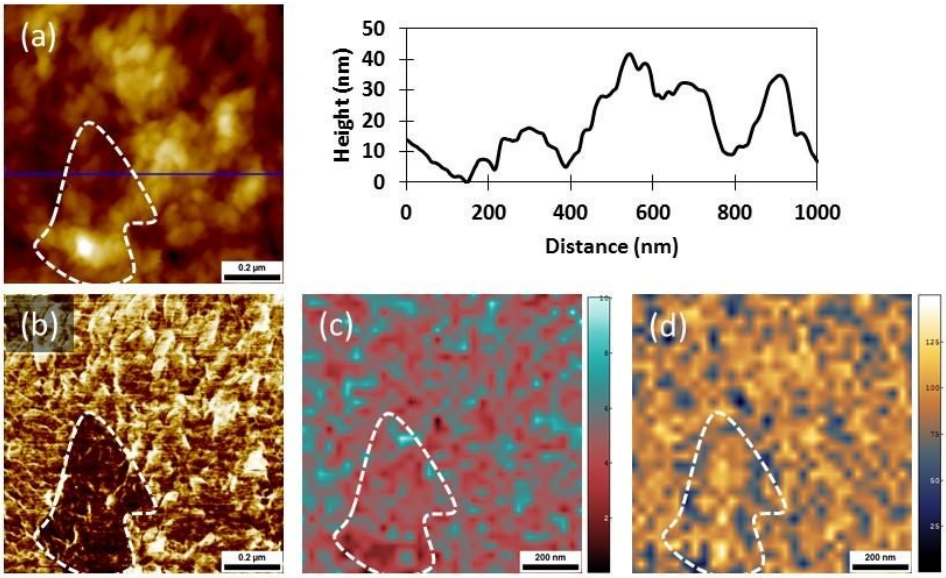

Figure 3.15. (a) Topography and cross section, (b) friction force image, (c) adhesion map (z-scale: 10 nN), and (d) 2D Young's modulus map (z-scale: 150 MPa) for the $(CRGO/ANF)_{35.5}$ LbL film. Here note the CRGO flake outlined by the white dashed line, similar to the results discussed for Figure 3.14. In (c), the adhesion on the flake is ~1 nN lower than the surrounding area.

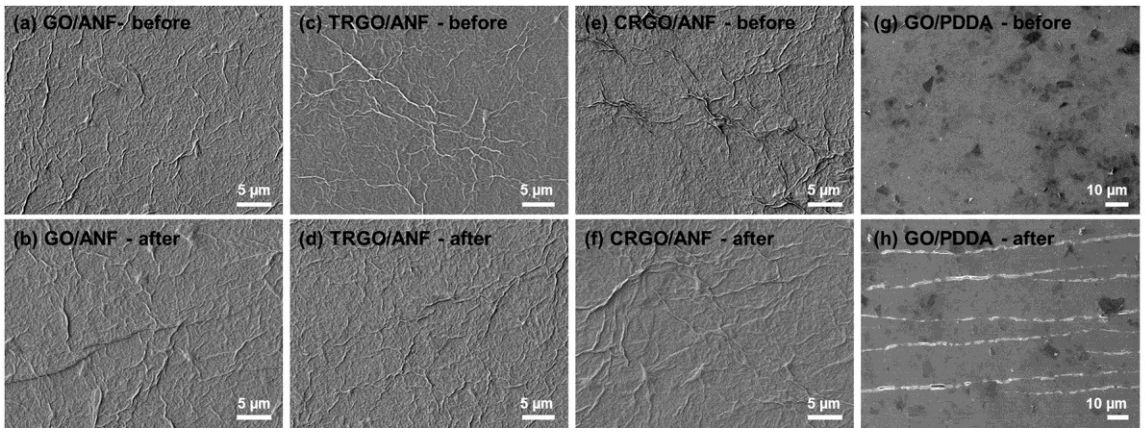

Figure 3.16. SEM surface images of (a, b) GO/ANF, (c, d) TRGO/ANF, (e, f) CRGO/ANF, and (g, h) GO/PDDA LbL films before and after 1000 cycles of flexure. The films are deposited on flexible ITO-coated PET substrates, and all films are 20 layer pairs.

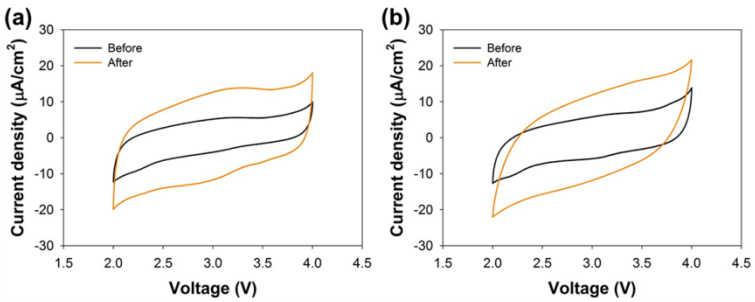

Figure 3.17. CV curves for (a) TRGO/ANF LbL and (b) CRGO/ANF LbL electrodes before and after 1000 cycles of flexure. Scan rate is 50 mV/s.

The electrochemical and structural stability of GO/ANF LbL films on PET after 1000 cycles of flexing to a radius of 5 mm was demonstrated. SEM images of the GO/ANF, TRGO/ANF, and CRGO/ANF LbL electrodes show no evidence of cracks or delamination following repeated bending, Figure 3.16. In contrast, a control film in which ANFs were replaced with a model polycation showed extensive cracking. This demonstrates that the mechanically strong ANFs can serve as a robust polymer matrix to bear mechanical deformation and stress during flexure. Interestingly, after cyclic flexure, the areal capacitance increased from 92 and 115 $\mu F/cm^2$ to 215 and 234 $\mu F/cm^2$ for TRGO/ANF and CRGO/ANF LbL electrodes, respectively, Figure 3.17. This two-fold enhancement may arise from ordering of the graphene sheets during the loading and unloading process, which increases the sheet-to-sheet contact, resulting in higher capacitance. [63, 201]

To explore how different LbL assembly strategy can affect the properties of the LbL films, GO/ANF composite films were created by spin-assisted LbL assembly process. The spin-assisted LbL films were assembled using the same procedure with dip-assisted LbL process. As the first layer, PDDA was dropped on the substrate and maintained for 1 min and spun. Next, GO dispersion (0.5 mg/mL, pH 3.5) was dropped on PDDA coated substrate, maintained for 1 min to interact with PDDA by electrostatic interaction, and spun. ANF/DMSO dispersion (0.2 mg/mL) was dropped on the GO sheets coated substrate, maintained for 10 sec and spun, and water (pH 7) was dropped on the substrate, maintained for 1 min and spun to re-protonate the negatively charged ANFs, which is critical for the formation of hydrogen bondings between ANFs, as well

as the ANFs and GO sheets, enabling the film growth. The substrates were spun at a spin speed of 2000 rpm.

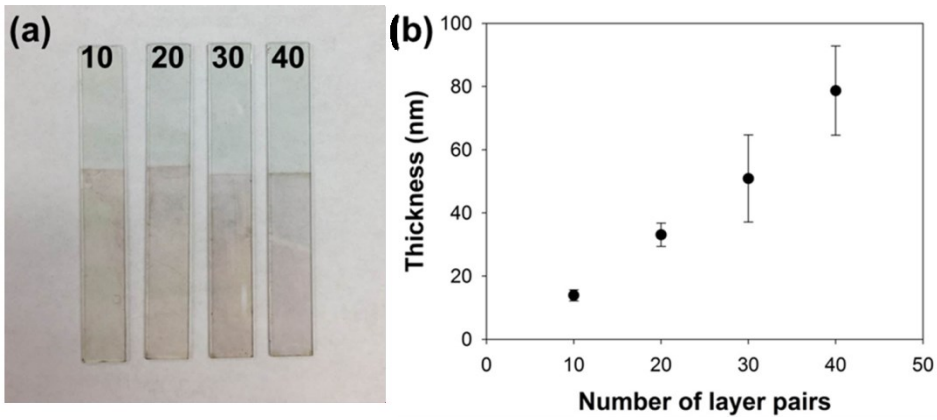

Figure 3.18. (a) Digital image of spin-assisted GO/ANF LbL films on ITO-coated glass with 10, 20, 30, and 40 layer pairs. (b) Growth profile of spin-assisted GO/ANF LbL films measured using profilometry.

The GO/ANF LbL films were light brown color, Figure 3.18a. The growth behavior of the LbL films was measured using profilometry. The thickness growth profile exhibited linear growth behavior with a growth rate of 2 nm per layer pair, Figure 3.18b. The thickness of spin-assisted $(GO/ANF)_{40}$ LbL film was 79 nm, which is thicker than the film made by dip-assisted LbL assembly. This might be because the absence of the water and DMSO rinsing steps could not remove the loosely adsorbed GO sheets and ANFs, respectively.

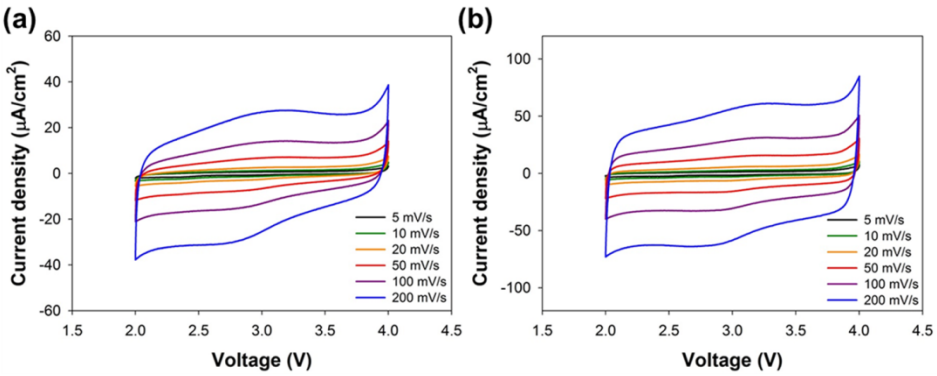

Figure 3.19. CV curves of (a) $(TRGO/ANF)_{40}$ and (b) $(CRGO/ANF)_{40}$ spin-assisted LbL films at varying scan rates.

As-prepared spin-assisted GO/ANF LbL films were reduced by both thermal and chemical treatment. Upon the reduction, the electrochemical performance was investigated using CV in three-electrode cell system. The CV curves of $(TRGO/ANF)_{40}$ and $(CRGO/ANF)_{40}$ spin-assisted LbL electrodes exhibited nearly rectangular shapes with a broad shoulder around 3V, which indicates that the charge can be stored by capacitive behavior of the RGO sheets and pseudocapacitive behavior of the remaining oxygen-containing functionalities on the surface of RGO sheets, Figure 3.19a and 19b. The CV curves of spin-assisted LbL electrodes showed the similar charge storage behavior compared with dip-assisted LbL electrodes. The areal capacitances were also calculated using integrated CV areas. The areal capacitances were 121 $\mu F/cm^2$ for TRGO/ANF, and 274 $\mu F/cm^2$ for CRGO/ANF LbL electrodes at a scan rate of 50 mV/s. The capacitance of the CRGO/ANF LbL electrode was higher than that of TRGO/ANF LbL electrode. While the areal capacitance of spin-assisted RGO/ANF LbL electrodes was slightly enhanced compared to dip-assisted LbL electrodes, the areal capacitance

were relatively lower compared to the reported values of graphene electrodes. This is also because the films are thin and the graphene content is low within the film.

3.4 Conclusion

Reduced GO/ANF LbL electrodes were fabricated via LbL assembly of GO sheets and ANFs, followed by thermal and chemical reduction. Their electrochemical and mechanical properties were examined, as well as their durability during repeated flexing. The LbL films were assembled by interfacial intermolecular interactions such as hydrogen bonding and π-π stacking between the GO sheets and the ANFs. The assembled GO/ANF LbL films exhibited linear growth behavior and an ANF-rich structure, with graphene oxide sheets intercalated between the ANFs within the LbL film. The films were reduced chemically and thermally, in which chemical reduction appeared to be more complete than thermal reduction. Both electrodes exhibited capacitive charge storage with areal capacitances as high as 221 $\mu F/cm^2$ (78 F/cm^3) in the case of CRGO/ANF LbL electrodes. The nanomechanical properties of the LbL film did not show a strong trend, independent of the terminal layers, film thickness, or reduction method, likely because of the high ANF content. The mechanical properties appeared to reflect a mixture of the two components. However, the electrodes showed exceptional durability toward repeated flexure, in which no cracks appeared after 1000 cycles. This highlights that ANFs provide exceptional flexibility to these graphene-based electrodes. Overall, the ANF/graphene composition shows a promising combination of properties, facilitated by favorable interactions between the two materials.

CHAPTER IV

MECHANICALLY STRONG GRAPHENE/ARAMID NANOFIBER COMPOSITE ELECTRODES FOR STRUCTURAL ENERGY AND POWER[1]

4.1 Introduction

Structural power systems, which simultaneously provide structural and electrochemical energy storage functionalities, have attracted great attention as a newly emerging type of energy and power system for a wide range of applications. The motivation is that a satisfactory combination of these two functionalities would yield a savings in mass and volume, with direct implications for aerial and ground vehicles, as well as portable electronics. A primary challenge is to develop multifunctional composites that can offer acceptable energy storage and mechanical performance simultaneously without dramatically sacrificing either property.[5, 202] Recent work in both structural electrodes and structural electrolytes for supercapacitors and Li-ion batteries shows an inherent tradeoff that must be understood and manipulated.[7, 203-205]

One common approach for structural electrodes is to use a structural material itself as the main component. Carbon-based materials including graphene, carbon fibers, and carbon nanotubes are primary examples.[5, 206-209] Carbon-fiber supercapacitor structural electrodes have been recently demonstrated, but these show low capacitance.[6, 202] Graphene, a two dimensional carbon-based nanosheet, has received great attention

[1] Modified and reprinted from "Mechanically strong graphene/aramid nanofiber composite electrodes for structural energy and power" by Se Ra Kwon, John Harris, Tianyang Zhou, James G. Boyd, and Jodie L. Lutkenhaus, *Submitted.*

because of its unique properties such as high capacitance, excellent electrical conductivity, good chemical and thermal stability, and extraordinary mechanical strength.[53, 128, 210] These characteristics render graphene a promising candidate for structural supercapacitors electrodes.[58, 211-212]

Graphene paper electrodes are particularly explored, yet many challenges remain towards their eventual use in structural energy and power. One challenge is the irreversible agglomeration and the restacking of individual graphene sheets, which decreases surface area and considerably lowers capacitive energy storage.[9, 63, 194] There have been great efforts to address this issue and optimize the properties of graphene paper by manipulating its physical, chemical, and structural properties.[9, 78, 84, 194, 213-214] Another approach to the challenge of restacking is to combine graphene paper electrodes with other guest materials that lay between the sheets such as polyaniline (PANI), manganese dioxide (MnO_2), carbon black, and carbon nanotubes (CNTs).[82, 164, 215-216] A second challenge lies in that of the mechanical properties of graphene paper electrodes. Graphene modification or inclusion of guest materials may potentially compromise modulus, strength, or toughness. A select few actually show good combinations of mechanical and electrochemical properties. Flexible reduced graphene oxide (RGO)/MnO_2 paper electrodes showed high areal capacitance (897 mF/cm^2) and good mechanical properties (8.79 MPa tensile strength, 9.84 GPa Young's modulus), comparable to other free-standing graphene papers.[198] Also, graphene/PANI composite paper exhibited large electrochemical capacitance of 233 F/g and enhanced tensile strength of 12.6 MPa, which is better than a reference graphene paper (8.8 MPa).[82]

Graphene-cellulose composite paper electrode showed excellent mechanical flexibility as well as an areal capacitance of 81 mF/cm^2 and excellent cyclic stability, which was attributed to the porous architecture of the electrodes supported by the polymeric cellulose matrix.[166] One of the more difficult mechanical properties to enhance is that of strength, with most of these prior examples falling below that of 15 MPa. This is because graphene sheets easily slide along one another in tension, especially with the inclusion of guest materials.

One of the most promising guest materials of late is that of aramid nanofiber (ANFs), or nanoscale Kevlar® fiber.[86, 89] Kevlar®, an ultrastrong para-aramid synthetic macroscale fiber produced from poly(paraphenylene terephthalamide) (PPTA), is well known for its excellent mechanical properties with a Young's modulus of 90 GPa and a tensile strength of 3.8 GPa.[86, 217-218] The exceptional strength and stiffness, which arise from interactions between PPTA chains such as π-π stacking, van der Waals forces, and hydrogen bonding, enable the use of the Kevlar® as a superior reinforcing material.[86] During the ANF production process, a strong base causes deprotonation between the polymer chains and forms a stable dispersion of polymeric nanofibers.[86, 89] The ANFs bear a negative surface charge, which allows for easy incorporation into nanocomposites.[175-176]

There have been several reports on composite materials containing ANFs and graphene or graphene-derivatives, but none for structural energy and power.[96-98, 174, 176] ANF/graphene nanocomposites have exhibited high mechanical performance (29.6 GPa Young's modulus and 209.4 MPa tensile strength) as well as good electrical conductivity

(145.8 S/m) and interfacial shear strength.[98, 174] ANF/CNT paper fabricated by a vacuum-assisted layer-by-layer process exhibited high mechanical performance, with a Young's modulus of 35 GPa and an ultimate tensile strength of 383 MPa.[176] ANFs with RGO sheets or CNTs have also been used as reinforcing nanofillers for poly(methylmethacrylate) (PMMA) and poly(vinyl alcohol), yielding enhancements in modulus of over 80%, for example.[96-97] Yet it is not known how ANFs would behave in structural energy and power systems. They possess extensive sites for noncovalent interactions for enhancing tensile strength and modulus, but ANFs are also electrochemically inactive, meaning that some tradeoff is expected.

Here, we report free-standing, high-strength composite supercapacitor electrodes consisting of RGO sheets and ANFs that balance both mechanical and electrochemical performance. These are prepared by vacuum-assisted filtration of the two components, and subsequent thermal reduction. This self-assembly technique was selected because it is suitable for designing nanocomposites with highly structured, uniform layers. The resulting electrode consists of oriented graphene layers separated by randomly dispersed ANFs, inter-connected by hydrogen bonding and π-π interactions between the materials. We hypothesize that these beneficial non-covalent interactions prevent re-stacking of the GO sheets during the filtration process and improve the mechanical stiffness and strength of the electrodes. The fundamental origin of the relationship between mechanical and electrochemical properties as it relates to electrode composition and structure is probed. Thus, this work contributes to the emerging need of mechanically

robust materials for multifunctional energy and power systems that display combinations of both desired properties.

4.2 Experimental Section

4.2.1 Materials

Graphite (SP-1) was purchased from Bay Carbon. Kevlar® 69 thread was purchased from Thread Exchange. Dimethyl sulfoxide, potassium permanganate, and sodium nitrate were purchased from Sigma Aldrich. Potassium hydroxide was purchased from Amresco. Carbon paper was purchased from Alfa Aesar. Microporous poly(propylene) separator (Celgard 3501) was provided from Celgard.

4.2.2 Preparation of RGO/ANF electrodes

To prepare the ANF dispersion, 1.0 g of bulk Kevlar® 69 thread and 1.5 g of potassium hydroxide (KOH) were added into 500 mL of dimethyl sulfoxide (DMSO).[86] The mixture was stirred for 7 to 10 days at room temperature, yielding a dark red ANF/DMSO dispersion (2 mg/mL). To prepare the GO dispersion, graphite oxide was first synthesized using a modified Hummers method.[158] 3 g of graphite powder was put into cold concentrated 120 mL of H_2SO_4. 2.5 g of $NaNO_3$ was added and stirred for 5 h in an ice water bath. Then, 15 g of $KMnO_4$ was gradually added to the mixture under stirring and the temperature of the mixture should be kept below 20 °C by cooling with ice. Then, the mixture was stirred at 35 °C for 2 h and diluted with 250 mL of deionized water at low temperature. 700 mL of deionized water and 20 mL of 30 wt% H_2O_2 was

added to the mixture. During this reaction the color of the mixture turned to brown. The mixture was washed with 5 wt% HCl solution and filtered. The filtered mixture was re-dispersed in deionized water and dialyzed to remove metal ions and acids. The resulting dispersion was dried at 60°C to yield graphite oxide powder. This was then dissolved in deionized water and exfoliated to give the GO dispersion using ultrasonication. A GO/DMSO dispersion was next obtained via solvent exchange. 200 mL of DMSO was added to 100 mL of the graphene oxide aqueous dispersion (2 mg/mL) and further sonicated for 2 h. The water was removed by vacuum distillation to give GO/DMSO dispersion (1 mg/mL).

GO/ANF composite films were fabricated via vacuum-assisted filtration. The desired amount of ANF/DMSO dispersion (0.2 mg/mL) was added into the GO/DMSO dispersion (1 mg/mL) and stirred for 1 h. Then, deionized water was added into the mixture and further stirred at 80 °C for 2 h to re-protonate the ANF amide groups and form hydrogen bonds between the ANFs and GO sheets. The GO/ANF/DMSO mixture was vacuum-filtered on nylon filter membrane (47 mm diameter, 0.2 μm pore size). The filtered GO/ANF composite films were rinsed with water and dried in air. The composite films were carefully peeled from the nylon membrane and placed between glass slides and dried at 80 °C in vacuum for 3 days. The total amount of the material was adjusted to 40 mg to yield films with 10 to 20 μm of thickness. These were then thermally annealed at 200 °C in vacuum for 2 h to yield reduced GO (RGO)/ANF composite films. The composite films were placed between the heavy tiles to prevent bubble formation during the thermal reduction process.

4.2.3 Materials characterization

The morphologies of the composite films were investigated using scanning electron microscopy (SEM) (JSM-7500F, JEOL) and atomic-force microscopy (AFM), (Nanoscope IIIa, Digital Instruments) in tapping mode. The prepared composite films were characterized using Raman spectroscopy (Horiba Jobin Yvon) with 514 nm excitation. X-ray photoelectron spectroscopy (XPS) analysis was performed using an Omicron ESCA Probe (Omicron Nanotechnology) with a monochromated Mg Ka radiation (hm = 1253.6 eV). X-ray diffraction (XRD) patterns were measured using an X-ray diffractometer (Bruker-AXS D8 Advance) with Cu-Ka radiation (λ=0.154 nm). Static uniaxial in-plane tensile testing was performed using a dynamic mechanical analyzer (DMA Q800, TA Instruments). The samples were cut into the rectangular strips of approximately 2 mm width and 20 mm length with a razor blade and the thickness of the film was measured using cross-sectional SEM. The samples were gripped using a film tension clamp with a clamp compliance of 0.2 μm/N. All tensile tests were conducted under controlled strain rate mode with a preload of 0.02 N and a strain ramp rate of 1 %/min. Mechanical data represents the average of at least 10 samples, with Dixon's q-test used to remove outliers. The error was taken as the standard deviation.

4.2.4 Electrochemical characterization

Electrochemical performance was characterized using a two-electrode symmetric coin cell with 6 M KOH as an aqueous electrolyte. The coin cell consisted of a top and bottom metal covering, two identical electrodes and current collectors, spring, spacer,

separator, and electrolyte. The electrodes were prepared by punching RGO/ANF composite films to 16 mm diameter. The typical combined mass of a pair of electrodes was around 9 mg, and the thickness of an individual electrode was 10-15 μm. Carbon paper and porous poly(propylene) were used as the current collector and the separator, respectively. All electrochemical tests were performed using a potentiostat/galvanostat (Gamry Interface 1000, Gamry Instruments) at room temperature.

Cyclic voltammetry was carried out at varying scan rates in a voltage range from 0 to 1 V. From the cyclic voltammetry curve, the specific capacitance (F/g) was calculated using the equation, $\mathrm{C} = 2\oint_{V_-}^{V_+} IdV/(v \times \Delta V \times m)$, where m is the mass of two electrodes (g), I is the current (A), V is the voltage (V), ΔV is the potential window, v is the scan rate (V/s), and V_+ and V_- are the high-voltage cut-off and low-voltage cut-off, respectively. Galvanostatic charge-discharge testing was conducted at various current densities based on the total mass of the two electrodes. The specific capacitance was calculated by the equation, $\mathrm{C} = 4I\Delta t/(m \times \Delta V)$, where I is the current (A), V is the voltage (V), ΔV is the potential window, $\Delta \mathrm{t}$ is discharging time (s), and m is the mass of two electrodes (g).

4.3 Results and Discussion

RGO/ANF structural electrodes of varying composition were fabricated using vacuum-assisted filtration. The synthesized ANFs were 30-40 nm in diameter and 5 to 10 μm in length, Figure 4.1. The desired amount of ANF/DMSO dispersion was added to a GO/DMSO dispersion and stirred; to this, water was added during stirring, followed

by filtration. The addition of the water produced a gel-like flocculation caused by the re-protonation of ANFs. This led to hydrogen bonding between the oxygen functional groups on GO sheets and the amide groups on ANFs.[176, 219] In addition, GO sheets and ANFs may associate by π-π interactions between the GO's graphitic basal plane and the ANF's polymer backbone.[220-221]

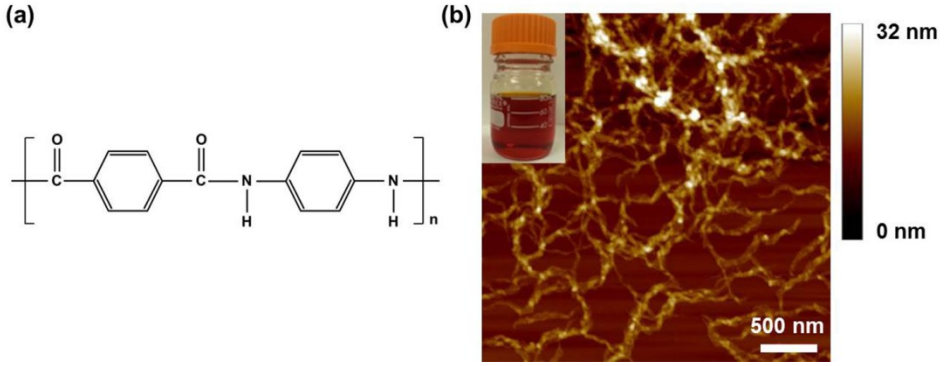

Figure 4.1. (a) Molecular structure of polyaramid PPTA. (b) AFM height images of ANFs drop-cast on mica (inset: digital image of prepared ANFs/DMSO dispersion).

As-prepared GO/ANF composite films were annealed at 200 °C under vacuum for 2 h to reduce the insulating GO sheets to electrically conductive RGO sheets. ANFs within the film begin to decompose at around 500 °C, so this reduction temperature is not expected to affect the ANFs.[86] Upon reduction, the color of the film changed from dark brown to black with a slight metallic luster, Figure 4.2a-2d. The free-standing electrodes were highly flexible, demonstrating structural integrity, as shown in Figure 4.2f and 2g. A top-view SEM image of the RGO and RGO/25wt% ANF composite

electrode showed a smooth surface, and the cross-sectional image revealed a well-stacked, compact, layered structure as shown in Figure 4.3.

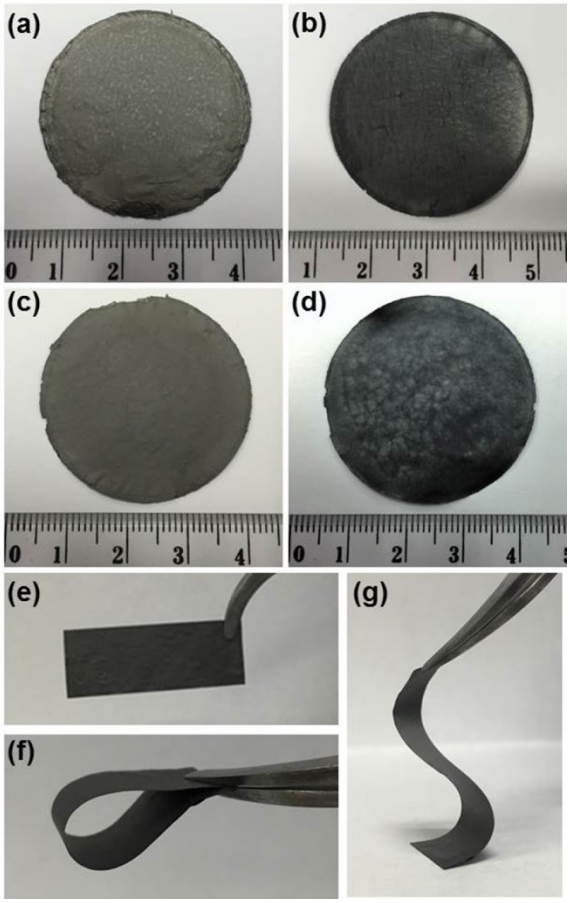

Figure 4.2. Digital images of (a) GO paper, (b) RGO paper, (c) GO/25 wt% ANF composite paper, (d) RGO/25 wt% ANF composite paper, and (e-g) RGO/25 wt% ANF composite electrodes in various states of flexure.

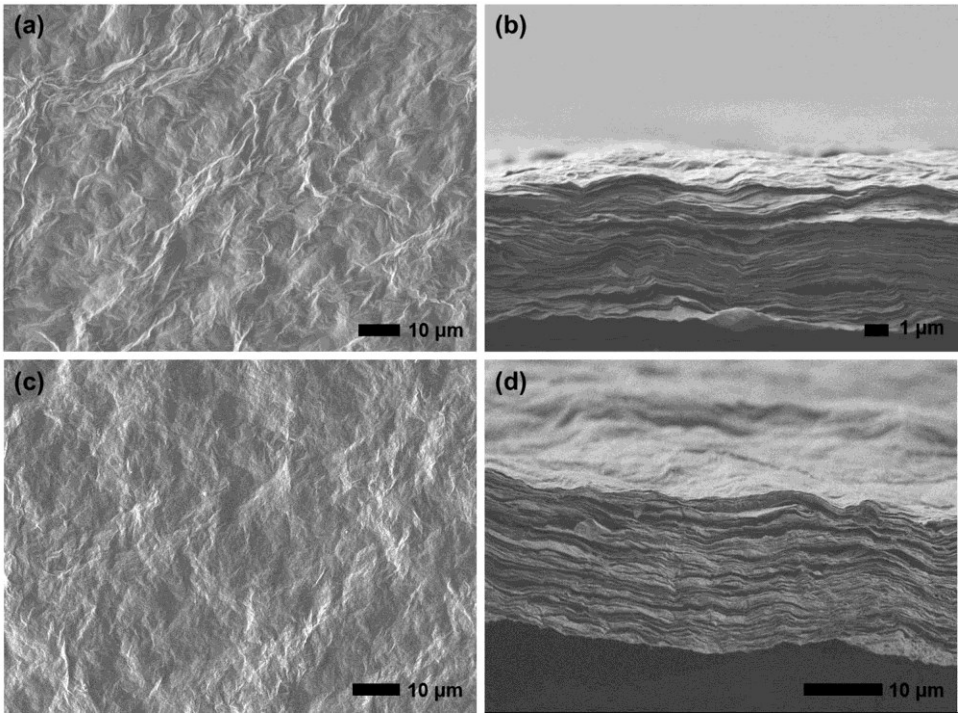

Figure 4.3. (a) Surface and (b) cross-sectional SEM images of RGO paper, (c) surface and (d) cross-sectional SEM images of RGO/25 wt% ANF composite paper.

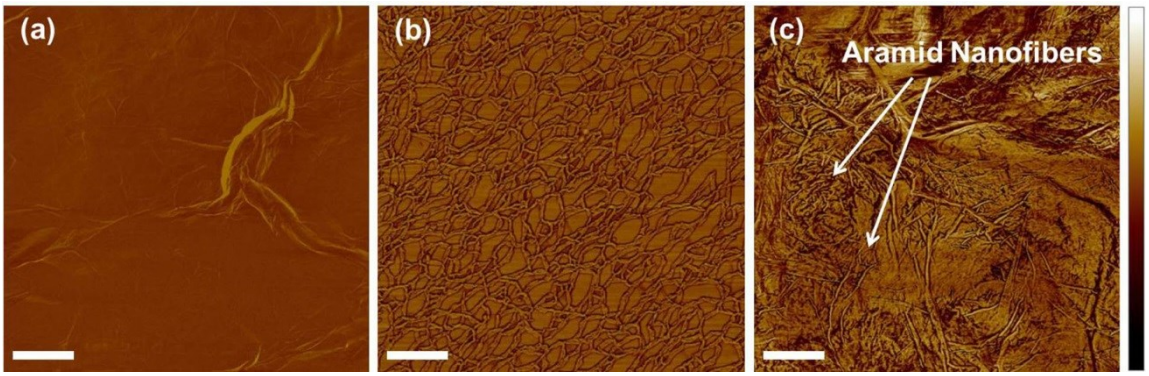

Figure 4.4. AFM phase images of (a) vacuum-assisted GO paper, (b) drop-cast ANFs on mica, and (c) GO/25 wt% ANF composite paper. Phase angle range is 0-55^{o}. Scale bars are 500 nm.

The ANFs were not easily observed in the SEM images due to their small dimension and relatively low content within the electrode. Instead, AFM was used to distinguish the presence of the ANFs. Figure 4.4 shows the AFM phase images of vacuum-assisted GO paper, drop-cast ANFs, and GO/ANF composite paper. The surface of the GO paper appeared smooth with an occasional wrinkle, which is characteristic of GO sheets, and the drop-cast ANFs appeared as thin fibers, Figure 4.4a and 4b, respectively. On the other hand, the GO/ANF composite paper surface showed randomly distributed ANFs and wrinkles from GO sheets, Figure 4.4c. These images demonstrate the presence of both GO sheets and ANFs in the composite electrode.

X-ray photoemission spectroscopy (XPS) analysis was performed to verify the elemental composition at the surface of GO, GO/10 wt% ANF, and GO/25wt% ANF films, Figure 4.5a. The GO film had 27 atomic percent (at %) oxygen and 73 at % carbon, but no nitrogen. The composite film had 1.7 at % and 3.3 at % nitrogen for 10 wt% and 25 wt% ANF content, respectively. This confirms the presence of the ANFs within the composite films since the nitrogen signal originates from the ANFs. XPS was further utilized to confirm the reduction of GO sheets. Figure 4.5b illustrates the XPS C1s spectra of GO/10 wt% ANF and RGO/10 wt% ANF composite papers. In the spectra of GO/10wt% ANF composite film, two distinct peaks, which correspond to sp^2-hybridized graphitic carbon (284.5 eV) and oxygen functional groups (286.2 eV), were observed.[63, 75] After thermal treatment, the peak assigned to the oxygen functional groups disappeared, indicating the reduction of GO to RGO.[63, 222-223] Also, the C/O ratio, which

was obtained from XPS survey scans, increased from 2.9 to 4.2, consistent with the reduction process.

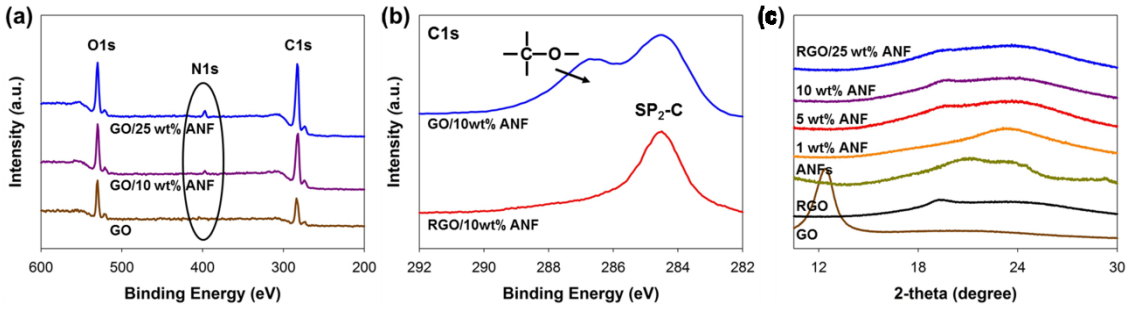

Figure 4.5. (a) XPS survey scans of GO, GO/10 wt% ANF, and GO/25 wt% ANF composite papers. (b) XPS C1s spectra of GO/10 wt% ANF and RGO/10 wt% ANF composite papers. (c) XRD patterns of GO, RGO, ANFs, and RGO/ANF composite papers.

Figure 4.5c shows the XRD patterns of GO, RGO, ANFs, and RGO/ANF composite electrodes. The GO paper exhibited a strong peak at around 12.1°, corresponding to a basal spacing of 0.74 nm.[224] After thermal reduction, weak and broad peaks at around 19° (d=0.47 nm) and 24° (d=0.37 nm) were observed in the RGO diffraction pattern, confirming successful reduction.[225] The peak at 24° results from restacked graphene layers after reduction, and the peak at around 19° arises from partially reduced GO.[225-226] The reduction process decreased the distance between graphene layers by removing oxygen-containing functional groups existing between the graphene layers and allowed for a more compact layered structure. Pure ANF films

exhibited diffraction peaks at 20.9° (d=0.42 nm) and 23.4° (d=0.38 nm), assigned to (110) and (200) diffractions, respectively.[86, 98] The diffraction patterns of RGO/ANF composite papers displayed two broad peaks around 19° and 23°, yet this is difficult to interpret because the shapes and positions are similar to that of both the RGO paper and the ANFs.

The mechanical properties of RGO, ANFs, and RGO/ANF composite paper electrodes were examined by tensile-testing, Figure 4.6a and Table 4.1. The Young's modulus and maximum tensile strength increased substantially with an increasing amount of ANFs. The average Young's modulus and tensile strength of the RGO/25 wt% ANF composite electrodes were 13.0±1.4 GPa and 100.6±7.9 MPa, which is 350 % and 290 % higher than RGO's Young's modulus and tensile strength of 3.7±0.4 MPa and 34.4±0.1 MPa, respectively. The RGO/1 wt% ANF electrode showed only a modest enhancement, whereas the Young's modulus and tensile strength of the RGO/5 wt% ANF electrode increased by 200 % and 170 %, respectively, as compared to RGO. The toughness of the composite films was generally higher than that of RGO, but no strong trend with composition was observed. The vacuum-filtered ANFs tend to have an extremely high toughness of 981.8±109 kJ/m^3, but modulus and strength were lower than that of the RGO/25 wt% ANFs electrode. The enhanced mechanical properties of the RGO/ANF composite electrodes are ascribed to the extensive hydrogen bonding and π-π interactions between the ANFs and the graphene sheets, where the fibrous ANFs are inter-connected to the face of the graphene sheets and bind the graphene sheets each other.[86, 89] 2D-orientation of the ANFs along the face of the RGO sheet could also

enhance the mechanical properties. This strengthens the mechanical connection and enables effective stress transfer. This result is remarkable because the usual inclusion of nanofillers into an RGO system at high nanofiller level often results in poor dispersion and a decrease in tensile strength and Young's modulus.[97, 227] Here, we observe the opposite at high ANF levels, where the general composite structure is retained and the mechanical properties are enhanced.

It should be emphasized that the observed enhancements are relative to RGO controls synthesized and measured here, resulting in up to 350 % and 290 % improvements in Young's modulus and tensile strength, respectively. In comparing against literature, it was found that the tensile strength of our prepared RGO paper was lower than the other reported values.[128, 228] This might be due to differences in structure and properties, caused by chemical modification of the GO sheets such as defects and heterogeneities or even concentration during vacuum filtration.[11, 82, 198, 229] The most likely cause is that our RGO paper was partially reduced at relatively low temperatures, resulting in more oxygen functional groups that interfere with π-π stacking and van der Walls interactions between RGO sheets, which reduces the mechanical properties of the pure RGO paper.

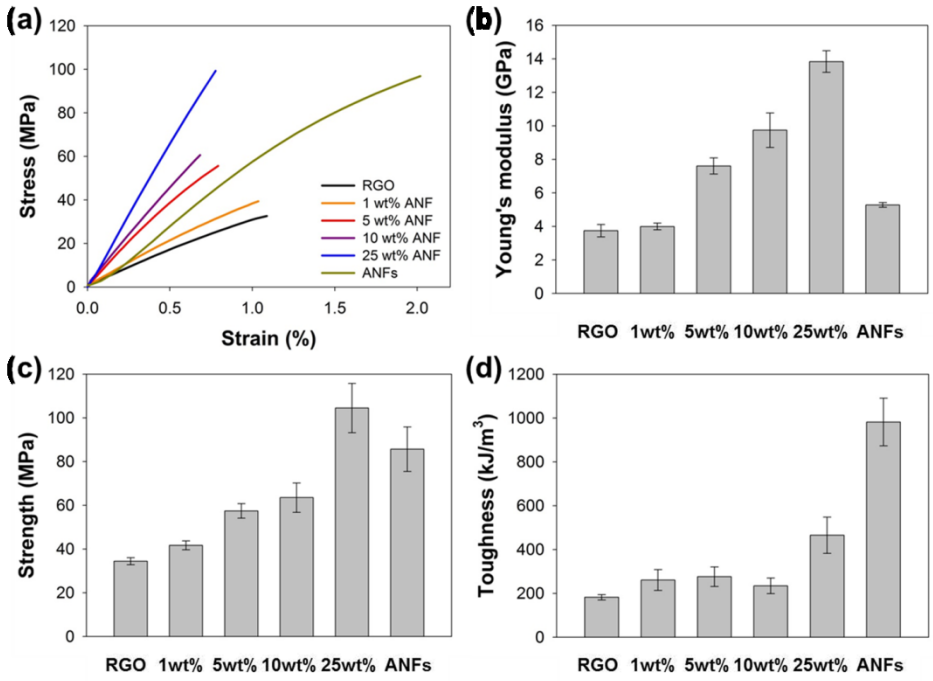

Figure 4.6. (a) Typical stress-strain curves of RGO/ANF composite electrodes. (b) Averaged Young's modulus, (c) averaged maximum tensile strength, and (d) averaged toughness of RGO/ANF composite electrodes. The weight fraction in the x-axis denotes the ANF content in the RGO electrode.

Table 4.1. Results of tensile testing.

wt %	#	Young's modulus (GPa)	Ultimate strain (%)	Strength (MPa)	Toughness (kJ/m^3)
RGO	1	3.3	1.09	32.6	195.2
	2	3.8	0.93	35.1	171.5
	3	4.1	0.95	35.6	180.2
	average	3.7±0.4	1.0±0.1	34.4±0.1	182.3 ±12
1 wt%	1	4.2	1.0	39.4	221.8
	2	3.8	1.3	42.3	297.9
	3	3.9	1.2	43.4	298.1
	average	4.0±0.2	1.2±0.1	41.7±2.0	272.6±44
5 wt%	1	8.2	0.79	55.7	241.0
	2	7.8	0.98	62.2	340.0
	3	7.3	0.85	54.6	251.1
	average	7.8±0.5	0.87±0.1	57.5±4.1	277.4±55
10 wt%	1	10.9	0.72	71.2	275.6
	2	9.1	0.68	58.7	211.3
	3	9.2	0.68	60.6	216.7
	average	9.7±1.0	0.69±0.02	63.5±6.7	234.5±36
25 wt%	1	14.4	0.81	109.0	459.1
	2	13.1	0.78	99.3	393.6
	3	11.6	0.88	93.4	429.5
	average	13.0±1.4	0.82±0.1	100.6±7.9	427.4±33
ANFs	1	5.2	2.2	83.4	988.2
	2	5.4	2.0	96.8	1087.5
	3	5.2	2.0	76.8	869.9
	average	5.3±0.1	2.04±0.1	85.7±10.2	981.8±109

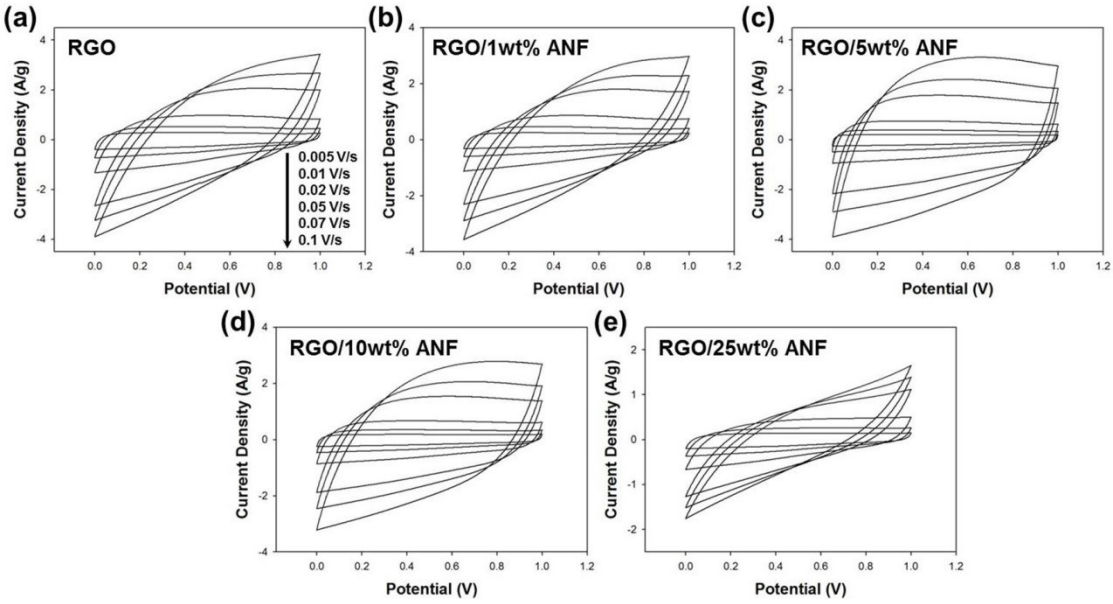

Figure 4.7. Cyclic voltammograms of RGO/ANF composite electrodes at varying scan rates and with different ANFs composition. (a) RGO, (b) RGO/1 wt% ANF, (c) RGO/5 wt% ANF, (d) RGO/10 wt% ANF, and (e) RGO/25 wt% ANF.

The supercapacitor performance of RGO/ANF composite paper electrodes was next investigated using a symmetrical two-electrode system in aqueous 6 M KOH electrolyte using cyclic voltammetry. Figure 4.7 shows the response of each composite paper electrode as the scan rate varied from 1 mV/s to 100 mV/s. Figure 4.8a shows the cyclic voltammograms (CVs) of the RGO/ANF composite electrodes of varying ANF compositions at a scan rate of 20 mV/s. The CV curves exhibit nearly rectangular shapes, which indicates capacitive charge storage by an electrical double layer mechanism.[58, 213] In general, the area enclosed by the CV decreased as the ANFs content increased from 0 to 25 wt%, suggestive of a decrease in capacitance. This trend is

confirmed by the calculated specific capacitance at various scan rates, Figure 4.8b and Table 4.2. The highest specific capacitance of each electrode was 226, 187, 170, 144, and 121 F/g for RGO, 1, 5, 10, and 25 wt% ANF composites at a scan rate of 1 mV/s. This trend is because, as the amount of electrically inactive ANFs increased within the composite electrodes, the RGO was diluted and the sheet-to-sheet contact was reduced.

As the scan rate increased, the specific capacitance of the electrode decreased. The specific capacitance of the RGO and 1 wt% composite decreased to 85 and 76 F/g at a scan rate of 100 mV/s, which corresponds to 37 % and 41 % of the values at 1 mV/s, respectively. For the 5 wt% and 10 wt% ANF composite electrodes, 57 % and 56 % of the capacitance was maintained at 100 mV/s, showing improved rate capability compared with the RGO and 1 wt% composite electrode. The better stability of the composite electrodes at 5 and 10 wt% ANF originates from the incorporation of the ANFs between the graphene layers. Although the electrically inactive ANFs yield lower capacitance values, the ANFs separate the graphene sheets and increase the inter-layer distance between the graphene sheets, which gives a more porous structure. This structure promotes ion diffusion and prevents re-stacking of the graphene sheets. In support of this, the CV curves of composite electrodes with 1, 5, and 10 wt% ANFs were less distorted at higher scan rates as compared with the RGO electrode, Figure 4.7. However, there does appear to be a point at which the ANF composition is so high that the electrochemical properties are dramatically reduced. This occurs at a much higher loading of 25 wt% ANFs, in which highly distorted CV curves and lower specific

capacitance were obtained. This is due to the high amount of non-conductive ANFs within the electrodes, where the high ANF content hinders electron conduction.

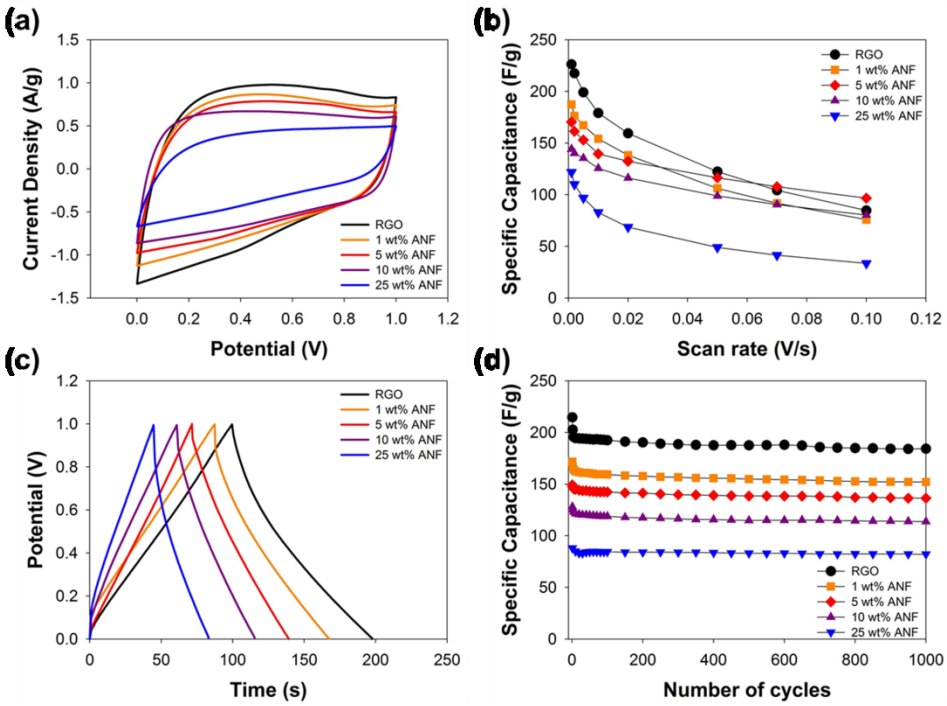

Figure 4.8. (a) Cyclic voltammograms of RGO/ANF composite electrodes at a scan rate of 20 mV/s. (b) Specific capacitance dependence on potential sweep rate. (c) Galvanostatic charge/discharge curves for RGO/ANF composite electrodes at a current density of 0.5 A/g. (d) Cycling behavior of RGO/ANF composite electrodes up to 1000 cycles at 0.5 A/g. Composition varied from 100% RGO to 25 wt% ANF. The current and capacitance are normalized against the total electrode mass (RGO + ANF).

Table 4.2. Specific capacitance at varying scan rates from CV curves.

Scan rate (V/s)	Specific Capacitance (F/g)				
	TRGO	1 wt% ANF	5 wt% ANF	10 wt% ANF	25 wt% ANF
0.001	226.3	187.4	170.4	144.2	121.8
0.002	217.5	176.2	161.4	140.1	110.0
0.005	199.1	167.3	153.0	135.4	96.9
0.01	179.1	154.2	139.6	125.6	82.8
0.02	159.4	138.3	132.4	116.2	68.7
0.05	122.4	106.2	116.4	98.8	49.0
0.07	104.2	91.7	107.8	90.5	41.4
0.1	84.7	75.9	96.6	80.3	33.5

Galvanostatic charge/discharge cycling was also performed for RGO and composite electrodes. Figure 4.8c shows typical galvanostatic charge/discharge curves at a current density of 0.5 A/g. The calculated specific capacitance was 207, 171, 145, 124, and 93 F/g for RGO and composite electrodes containing 1, 5, 10, and 25 wt% ANFs, respectively. Prolonged cycling at 0.5 A/g, shows the excellent stability of the composite electrodes, Figure 4.8d and Table 4.3. The specific capacitance of the RGO electrode retained 86 % of the initial capacitance after 1000 cycles. In comparison, the RGO/ANF composite electrodes showed slightly better capacity retention, maintaining 89 to 93 % of the initial capacitance. This is attributed to the prevention of restacking and aggregation of graphene sheets by introducing ANFs between the graphene layers in the composite electrodes. Also, the ANFs may maintain electrochemical stability because of the extensive hydrogen bonding between PPTA chains. The results from galvanostatic charge-discharge cycling are consistent with those from cyclic voltammetry, where the introduction of the ANFs allows structural changes that facilitate ion diffusion and better electrochemical stability, but decrease the capacitance because of its insulating nature. However, it should be noted that, for multifunctional energy and power, there often exists a tradeoff between electrochemical and mechanical properties, where an acceptable balance between the two must be met.

Table 4.3. Specific capacitance and capacitance retention ratio from galvanostatic charge/discharge cycling test at 0.5 A/g.

cycle #	RGO		1 wt% ANF		5 wt% ANF		10 wt% ANF		25 wt% ANF	
	F/g	%	F/g	%	F/g	%	F/g	%	F/g	%
1	215	100.0	172	100.0	149	100.0	128	100.0	88	100.0
10	194	90.6	162	94.6	145	97.1	121	94.8	85	96.5
50	194	90.1	161	93.6	143	95.9	120	93.5	85	96.0
100	193	89.7	159	92.9	142	95.4	119	92.8	85	96.0
200	190	88.7	158	91.9	141	94.7	117	91.7	84	95.4
300	189	87.9	157	91.3	140	93.6	116	91.0	84	95.3
400	188	87.4	156	90.7	139	93.2	116	90.4	84	95.0
500	188	87.4	155	90.2	138	92.8	115	89.7	83	94.4
600	188	87.6	154	89.9	138	92.7	115	89.8	83	94.4
700	186	86.6	154	89.5	138	92.6	115	89.9	82	93.6
800	185	86.1	153	88.9	137	91.9	114	89.4	82	93.7
900	184	85.8	152	88.8	137	91.6	114	89.2	82	93.5
1000	184	85.8	152	88.6	136	91.4	114	88.8	82	93.3

To visualize the mechanical and electrochemical properties together, we plot the specific capacitance vs tensile strength of our results compared against other free-standing paper electrodes collected from the literature, Figure 4.9 and Table 4.4. These include that of carbon-based flexible paper electrodes including buckypaper, RGO aerogels, wire shaped RGO/CNT composites, RGO/MnO_2, polypyrrole (Ppy)/RGO, RGO/PANI, RGO-cellulose, SWCNT-Ppy-cyanate ester (CE) composite, and RGO paper fabricated using different chemical modifications.[8-9, 82, 123, 166, 198, 229-235]

The plot shows that the RGO/ANF composite films here exhibit a good combination of electrochemical and mechanical properties as compared to most other graphene-based nanocomposite electrodes. The higher specific capacitance of Ppy/RGO and SWCNT-Ppy-CE composite papers was attributed to the incorporation of a conducting polymer, which increased the specific capacitance by adding psuedocapacitance.[231-232] Whereas other graphene paper electrodes exhibited capacitance values similar to that of the RGO/ANF paper electrodes, our electrodes exhibited much higher tensile strength due to the extensive interactions between the RGO sheets and ANFs.[9, 229] This result is important as it offers a route to high strength capacitor electrodes without a significant tradeoff in capacitance.

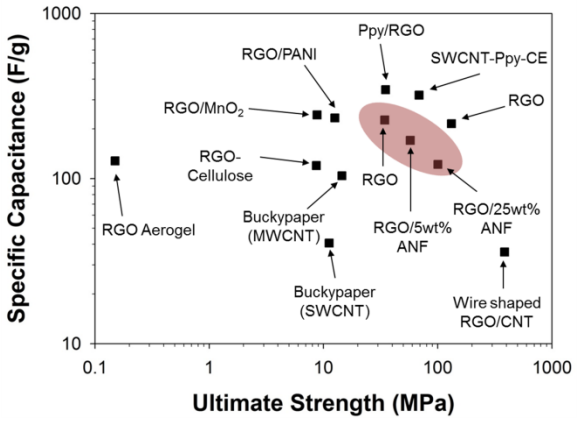

Figure 4.9. An Ashby plot of specific capacitance vs ultimate strength for results herein compared against other free-standing paper electrodes.

Table 4.4. Ashby plot data from Figure 4.9.

Materials	Strength (MPa)	Specific Capacitance (F/g)	Fabrication Method	
			Electrochemical	Mechanical
RGO/MnO_2 paper[198]	8.79	243	Vacuum filtration of GO/MnO_2 dispersion, followed by hydrazine reduction	
Polypyrrole nanofibre/RGO paper[232]	35	345	Vacuum filtration of Ppy/GO dispersion, followed by HI reduction	
RGO-Cellulose paper[166]	8.67	120	Vacuum filtration of graphene dispersion through cellulose filter paper	
Wire shaped RGO/CNT composite[233]	385.7	35.9	Wet spinning of GO/FWCNT dispersion (4:1 wt. ratio), followed by HI reduction	
RGO-Polyaniline paper[82]	12.6	233	In situ anodic electropolymerization of polyaniline film on graphene paper	
RGO aerogel[235]	0.15	128	Supercritical CO_2 drying of graphene hydrogel precursors obtained from heating the aqueous mixture of graphene oxide with L-ascorbic acid	
MWCNT paper[123, 234]	14.5	104	Spray layer-by-layer assembly of MWNT-NH_3^+/MWNT-COO^-) on carbon paper[123]	Electrophoretically deposited on stainless steel susbstrate and liberated from substrate[234]

Table 4.4. Continued.

Materials	Strength (MPa)	Specific Capacitance (F/g)	Fabrication Method	
			Electrochemical	Mechanical
SWCNT-Ppy-CE composite paper[231]	68.73	320	Ppy deposited on SWCNT buckypaper by potentioamperometric polymerization, and soaked in cyanate ester solution	
RGO paper[214, 229]	132	215	Vacuum filtration of chemically reduced grapehene dispersion, followed by dipping in water for solvated graphene film[214]	Vacuum filtration of chemically reduced graphene dispersion[229]
SWCNT paper[8, 230]	11.2	40.7	Vacuum filtration of SWNT dispersion[230]	Vacuum filtration of SWNT dispersion[8]

For structural electrode materials, it is required to simultaneously balance the electrochemical and mechanical properties without substantially sacrificing one property over another. This relationship may be expressed as the multifunctional efficiency, σ^{mf}, which is defined as the sum of the energy and structural efficiencies (σ^{e} and σ^{s} or $\hat{\sigma}^{s}$ respectively):[236-238]

$$\sigma^{mf} = \sigma^{e} + \sigma^{s} \quad \text{or} \quad \sigma^{mf} = \sigma^{e} + \hat{\sigma}^{s} \tag{4.1}$$

$$\sigma^{e} = \frac{\Gamma}{\Gamma_{typ}} \tag{4.2}$$

$$\sigma^{s} = \frac{\mathrm{E}}{\mathrm{E}_{typ}} \tag{4.3}$$

$$\hat{\sigma}^{s} = \frac{F}{F_{typ}} \tag{4.4}$$

where Γ_{typ}, E_{typ}, and F_{typ} are the specific energy, Young's modulus, and tensile strength of a typical capacitor or structural composite, respectively. It has been discussed that savings in mass or volume are obtained when σ^{mf} is greater than 1. By this relation, a strength-based σ^{mf} is 1.38, 1.25, 1.32, and 1.53 for the RGO electrodes containing 0, 1, 5, and 25 wt% ANFs, respectively. Similarly a modulus-based $\sigma^{mf}$is 1.77, 1.64, 2.58, and 3.21 for the RGO electrodes containing 0, 1, 5, and 25 wt% ANFs, respectively, taking epoxy (specific Young's modulus = 2.8 GPa cm^3/g, specific tensile strength = 60.18 MPa cm^3/g) and carbon aerogel (specific energy = 29.16 Wh/kg) as typical structural and capacitor systems, respectively. This demonstrates that the multifunctional

efficiency can be tuned by composition and may prove to be a useful selection criterion for structural energy and power systems.

4.4 Conclusion

High strength RGO/ANF supercapacitor electrodes were fabricated by harnessing the extensive hydrogen bonding and π-π interactions occurring between ANFs and RGO sheets. These RGO/ANF composite electrodes exhibited a well-layered structure in which ANFs were dispersed between the graphene sheets, leading to a 350 % and 290 % improvement for Young's modulus and tensile strength, respectively, relative to RGO. As a result, the ultimate tensile strength of the RGO/ANF composite (100.6±7.9 MPa) was far larger than that of other graphene-based or CNT-based paper electrodes (the majority are < 15 MPa). The inclusion of ANFs generally led to good capacitive cycling behavior and modest enhancement in rate capability, which was attributed to the porous structure of the composite electrodes that prevented restacking and aggregation. At larger ANF content, the capacitance decreased while the mechanical properties increased, demonstrating a tradeoff. These electrodes demonstrated an outstanding combination of both mechanical and electrochemical properties as compared to other paper-based electrodes. The multifunctional efficiency of the RGO/ANF composite electrode was consistently greater than unity, suggesting an acceptable combination of both mechanical and electrochemical properties to realize a potential savings in mass. These intriguing properties suggest that the design of a structural electrode using graphene and ANFs is a

promising combination for mechanically strong electrodes with good electrochemical properties.

CHAPTER V

CONCLUSIONS AND FUTURE DIRECTIONS

5.1 Conclusions

This thesis investigated how material properties and film fabrication methods of composites affect the morphologies and compositions of the composite films, and how the architecture of the nanocomposite can influence the electrochemical and mechanical performance of the electrodes. Graphene was combined with selected polymers, including PANI NFs and ANFs, using various processing methods. Three different graphene-polymer nanocomposite systems were explored: spray-assisted LbL assembled PANI NF/graphene electrodes, dip-assisted LbL assembled ANF/graphene electrodes, and vacuum-filtrated graphene/ANF paper electrodes. The properties of these nanocomposite electrodes were examined in the context of structural energy and power.

The first technique to prepare the composite film was a spray-assisted LbL assembly which enabled rapid fabrication of thick films onto a variety of substrates. PANI NF/ERGO electrodes were successfully fabricated by alternate spraying of PANI NFs and GO sheets, followed by an electrochemical reduction. The film deposition was optimized by removing the rinsing step and controlling the blow-drying time. The rinsing step disturbed the formation of wetted area where the materials' diffusion-adsorption process takes place, which resulted in poor film quality. The thickness of the wetted area for the film formation was optimized by adjusting the blow-drying time during the process. The prepared PANI NF/GO spray-assisted LbL film showed linear

film growth behavior and the average thickness per layer pair, 46 nm per layer pair, was comparable with the diameter of PANI NFs, suggesting the film structure in which PANI NFs lay flat to the substrate's surface with GO sheets in between the PANI NF layers. The morphology and the electrochemical performance of the spray-assisted LbL electrodes were compared with the electrodes made by dip-assisted LbL assembly. The spray-assisted LbL electrodes exhibited 74 times faster film growth behavior and more porous structure than dip-assisted LbL electrodes. The increased porosity enabled the enhanced rate capability and a higher power at a given specific energy compared with dip-assisted LbL electrodes. The highest capacity, energy and power obtained were 114 mAh/g at 0.03 A/g, 346 mWh/g at 0.1 A/g, and 54090 mW/g at 20 A/g, respectively. Based on the performance of the electrodes and the versatile adaptability of the spray-assisted LbL process onto various substrates including flexible PET, it was demonstrated that the spray-assisted LbL process is a promising film fabrication method for the flexible energy storage devices.

For the second and the third research areas, mechanically strong polymer ANFs were selected as a reinforcing material and blended with graphene using various processing techniques, including dip-assisted LbL assembly and vacuum-assisted filtration, for multifunctional nanocomposite electrodes.

RGO/ANF LbL films were fabricated via dip-assisted LbL assembly of GO sheets and ANFs and subsequent thermal and chemical reduction. The GO/ANF LbL films were created by interfacial intermolecular interactions such as hydrogen bonding and π-π stacking between the GO sheets and the ANFs. The GO/ANF LbL films

exhibited linear growth behavior with a small growth rate of 1.2 nm per layer pair, which suggested a sub-monolayer deposition of the materials. The surface composition of the films indicated ANFs-rich structure of the assembled LbL films (75% of ANFs and 25% of GO sheets), where the GO sheets were intercalated between the ANFs within the LbL film. After chemical and thermal reductions, the electrochemical properties of CRGO/ANF and TRGO/ANF LbL electrodes were investigated as electrodes for supercapacitors. RGO/ANF LbL electrodes exhibited capacitive charge storage behavior and the electrochemical performance of the CRGO/ANF LbL electrodes was higher than that of TRGO/ANF LbL electrodes. Nanomechanical test showed that the mechanical properties of the LbL films did not show a strong trend, independent of the terminal layers, film thickness, or reduction method. Young's modulus values were intermediate of the individual ANF and GO components, likely because of the high ANF content. However, the electrodes showed exceptional durability toward repeated flexure, in which no cracks appeared after 1000 cycles. This demonstrated that ANFs provide exceptional flexibility to RGO/ANF electrodes as robust polymer matrix and RGO/ANF combination is promising for flexible, mechanically strong energy and power.

To increase the graphene content within the film, vacuum-assisted filtration was selected as an alternative strategy. The RGO/ANF composite electrodes for supercapacitors were prepared by simple filtration of a GO/ANF mixture, followed by thermal annealing. These RGO/ANF composite paper electrodes showed well-layered, uniform structure where ANFs were placed between graphene sheets. The polymeric nanofiller, ANFs were inter-connected with graphene sheets by non-covalent

interactions such as hydrogen bonding and π-π stacking, binding the graphene sheets each other. As a result, the tensile strength and Young's modulus of the RGO/25 wt% ANF composite electrodes reached 100.6±7.9 MPa and 13.0±1.4 GPa, which is 350 % and 290 % improvement as compared to RGO, respectively. Further, the incorporation of ANFs into the composite system led to stable electrochemical performance, showing enhanced rate capability and capacitance retention. This was attributed to the porous structure of the composite electrodes in which ANFs prevent the aggregation and restacking of graphene sheets. The RGO/ANF composite paper electrodes exhibited excellent combination of both mechanical and energy storage properties as compared to other carbon-based paper electrodes. The multifunctional efficiency demonstrated the acceptable combination of both mechanical and electrochemical properties for these high-strength composite supercapacitor electrodes, suggesting the potential reduction in mass or volume of structural power system. It was realized that the RGO/ANF composite electrode is promising combination for multifunctional structural electrodes which can offer desired mechanical and electrochemical properties.

In conclusion, multifunctional structural composite electrodes were designed and demonstrated in this thesis. Ultimately, through the novel material design, desirable multifunctional properties can be achieved for structural power system.

5.2 Future Directions

As observed in Chapter IV, the RGO/ANF composite paper electrodes exhibited the excellent combination of both mechanical and electrochemical functionalities, but at high ANFs content, the electrochemical performance dramatically decreased. The tradeoff arising from the large ANF content might be improved by adding the third component into the system such as CNTs and $LiCoO_2$.

CNTs are promising electrode materials for structural power systems due to the high electrical conductivity and excellent mechanical properties. CNTs have been used as an electrode material as itself or an additive, providing conductive pathways and capacitance. Also, the high aspect ratio and mechanical properties allow the CNTs to be used as high performance reinforcing nanofillers for composites. Along this line, by incorporating functionalized MWNT into the RGO/ANF composite electrodes, functionalized MWNT might provide extensive reactive sites with ANFs and create uniform two-dimensional distribution within the composites even at higher ANFs loading, leading to the enhancement in mechanical property. The capacitive charge storage feature of MWNT contributes to the capacitance of the electrodes, providing an effective conductive pathway within the composite electrodes. Further, the porous structure enabled by the inclusion of MWNT might improve the electrochemical performance by diluting the insulating ANFs and facilitating ion diffusion.

$LiCoO_2$ is the most commonly used cathode material for lithium ion batteries due to its high specific energy. The structural stability and the electrochemical performance of $LiCoO_2$ cathodes might be improved by incorporating RGO/ANF composite system

into the $LiCoO_2$ cathodes. Typical $LiCoO_2$ cathodes can be prepared by mixing $LiCoO_2$, binder, and conductive additives. The polymeric binder and carbon-based conductive additives can be replaced by ANFs and RGO nanosheets, respectively. Within $LiCoO_2$/RGO/ANF cathode structure, the RGO/ANF composite architecture where RGO and ANFs were inter-connected by non-covalent bondings might provide conductive pathways and robust structural network for $LiCoO_2$ cathode. The energy storage capability of RGO sheets by capacitive and pseudocapacitive behavior can contribute to the overall capacity of the $LiCoO_2$/RGO/ANF composite electrodes and the porous structure of the composite electrodes arisen from the inclusion of RGO/ANF can improve the rate capability and power density. Further, the cycling loss arising from the structural instability might be improved through the incorporation of RGO/ANF composite into the $LiCoO_2$ cathode. The RGO/ANF network prevents the structural changes of $LiCoO_2$ during the lithium intercalation/deintercalation process, leading to enhanced cyclic behavior. Also, the mechanical properties of the composite electrode can be improved by incorporating RGO/ANFs, as compared to $LiCoO_2$ electrodes

The combination of RGO/ANF with MWNTs and $LiCoO_2$ might be a promising way to obtain higher multifunctionalities as mechanically robust electrodes with good electrochemical performance.

REFERENCES

1. El-Kady, M. F.; Strong, V.; Dubin, S.; Kaner, R. B. *Science* **2012**, *335*, 1326-1330.

2. Hu, L.; Pasta, M.; La Mantia, F.; Cui, L.; Jeong, S.; Deshazer, H. D.; Choi, J. W.; Han, S. M.; Cui, Y. *Nano Letters* **2010**, *10*, 708-714.

3. Hu, L.; Wu, H.; La Mantia, F.; Yang, Y.; Cui, Y. *ACS Nano* **2010**, *4*, 5843-5848.

4. Singh, N.; Galande, C.; Miranda, A.; Mathkar, A.; Gao, W.; Reddy, A. L. M.; Vlad, A.; Ajayan, P. M. *Scientific Reports* **2012**, *2*, 481.

5. Asp, L. E.; Greenhalgh, E. S. *Composites Science and Technology* **2014**, *101*, 41-61.

6. Carlson, T.; Ordéus, D.; Wysocki, M.; Asp, L. E. *Composites Science and Technology* **2010**, *70*, 1135-1140.

7. Hagberg, J.; Leijonmarck, S.; Lindbergh, G. *Journal of The Electrochemical Society* **2016**, *163*, A1790-A1797.

8. Whitten, P. G.; Spinks, G. M.; Wallace, G. G. *Carbon* **2005**, *43*, 1891-1896.

9. Yang, X.; Zhu, J.; Qiu, L.; Li, D. *Advanced Materials* **2011**, *23*, 2833-2838.

10. Xiao, F.-X.; Pagliaro, M.; Xu, Y.-J.; Liu, B. *Chemical Society Reviews* **2016**, *45*, 3088-3121.

11. Eda, G.; Fanchini, G.; Chhowalla, M. *Nature Nanotechnology* **2008**, *3*, 270-274.

12. Putz, K. W.; Compton, O. C.; Palmeri, M. J.; Nguyen, S. T.; Brinson, L. C. *Advanced Functional Materials* **2010**, *20*, 3322-3329.

13. Simon, P.; Gogotsi, Y. *Nature Materials* **2008**, *7*, 845-854.

14. Scrosati, B.; Garche, J. *Journal of Power Sources* **2010**, *195*, 2419-2430.

15. Winter, M.; Brodd, R. J. *Chemical Reviews* **2004**, *104*, 4245-4270.

16. Liu, R.; Duay, J.; Lee, S. B. *Chemical Communications* **2011**, *47*, 1384-1404.

17. Patil, A.; Patil, V.; Shin, D. W.; Choi, J.-W.; Paik, D.-S.;Yoon, S.-J. *Materials Research Bulletin* **2008**, *43*, 1913-1942.

18. Galiński, M.; Lewandowski, A.; Stępniak, I. *Electrochimica Acta* **2006**, *51*, 5567-5580.

19. Manuel Stephan, A. *European Polymer Journal* **2006**, *42*, 21-42.

20. Arora, P.; Zhang, Z. *Chemical Reviews* **2004**, *104*, 4419-4462.

21. Desilvestro, J.; Haas, O. *Journal of the Electrochemical Society* **1990**, *137*, 5C-22C.

22. Eriksson, T. A.; Doeff, M. M. *Journal of Power Sources* **2003**, *119–121*, 145-149.

23. Idemoto, Y.; Narai, H.; Koura, N. *Journal of Power Sources* **2003**, *119–121*, 125-129.

24. Thomas, J. *Nature Materials* **2003**, *2*, 705-706.

25. Yamada, A.; Chung, S. C.; Hinokuma , K. *Journal of the Electrochemical Society* **2001**, *148*, A224-A229.

26. Liang, Y.; Tao, Z.; Chen, J. *Advanced Energy Materials* **2012**, *2*, 742-769.

27. Novák, P.; Müller, K.; Santhanam, K. S. V.; Haas, O. *Chemical Reviews* **1997**, *97*, 207-282.

28. Kwon, S. R.; Jeon, J.-W.; Lutkenhaus, J. L. *RSC Advances* **2015**, *5*, 14994-

15001.

29. Shao, L.; Jeon, J.-W.; Lutkenhaus, J. L. *Journal of Materials Chemistry A* **2014**, *2*, 14421-14428.

30. Jeon, J.-W.; Ma, Y.; Mike, J. F.; Shao, L.; Balbuena, P. B.; Lutkenhaus, J. L. *Physical Chemistry Chemical Physics* **2013**, *15*, 9654-9662.

31. Arico, A. S.; Bruce, P.; Scrosati, B.; Tarascon, J.-M.; van Schalkwijk, W. *Nature Materials* **2005**, *4*, 366-377.

32. Liu, S.; Liu, X.; Li, Z.; Yang, S.; Wang, J. *New Journal of Chemistry* **2011**, *35*, 369-374.

33. Shukla, A. K.; Banerjee, A.; Ravikumar, M. K.; Jalajakshi, A. *Electrochimica Acta* **2012**, *84*, 165-173.

34. Lee, S. W.; Gallant, B. M.; Byon, H. R.; Hammond, P. T.; Shao-Horn, Y. *Energy & Environmental Science* **2011**, *4*, 1972-1985.

35. Wang, Y.; Song, Y.; Xia, Y. *Chemical Society Reviews* **2016**, *45*, 5925-5950.

36. Ogoshi, T.; Yoshikoshi, K.; Sueto, R.; Nishihara, H.; Yamagishi, T.-a. *Angewandte Chemie* **2015**, *54*, 6466-6469.

37. Conway, B. E., *Electrochemical Supercapacitors : Scientific Fundamentals and Technological Applications*, Kluwer Academic/Plenum Press, New York, USA, **1999**.

38. Frackowiak, E.; Béguin, F. *Carbon* **2001**, *39*, 937-950.

39. Toupin, M.; Bélanger, D.; Hill, I. R.; Quinn, D. *Journal of Power Sources* **2005**, *140*, 203-210.

40. Liu, H.-J.; Wang, J.; Wang, C.-X.; Xia, Y.-Y. *Advanced Energy Materials* **2011**, *1*,

1101-1108.

41. Li, H.-Q.; Liu, R.-L.; Zhao, D.-Y.; Xia, Y.-Y. *Carbon* **2007**, *45*, 2628-2635.

42. Liu, H.-J.; Cui, W.-J.; Jin, L.-H.; Wang, C.-X.; Xia, Y.-Y. *Journal of Materials Chemistry* **2009**, *19*, 3661-3667.

43. Zhou, D.-D.; Du, Y.-J.; Song, Y.-F.; Wang, Y.-G.; Wang, C.-X.; Xia, Y.-Y. *Journal of Materials Chemistry A* **2013**, *1*, 1192-1200.

44. Zhou, D.-D.; Liu, H.-J.; Wang, Y.-G.; Wang, C.-X.; Xia, Y.-Y. *Journal of Materials Chemistry* **2012**, *22*, 1937-1943.

45. Hulicova-Jurcakova, D.; Seredych, M.; Lu, G. Q.; Bandosz, T. J. *Advanced Functional Materials* **2009**, *19*, 438-447.

46. Yang, X.; Wu, D.; Chen, X.; Fu, R. *The Journal of Physical Chemistry C* **2010**, *114*, 8581-8586.

47. Zhao, Y.; Ran, W.; He, J.; Song, Y.; Zhang, C.; Xiong, D.-B.; Gao, F.; Wu, J.; Xia, Y. *ACS Applied Materials & Interfaces* **2015**, *7*, 1132-1139.

48. Zhou, D.-D.; Li, W.-Y.; Dong, X.-L.; Wang, Y.-G.; Wang, C.-X.; Xia, Y.-Y. *Journal of Materials Chemistry A* **2013**, *1*, 8488-8496.

49. Wang, G.; Zhang, L.; Zhang, J. *Chemical Society Reviews* **2012**, *41*, 797-828.

50. Liu, Y.; Ma, Y.; Guang, S.; Xu, H.; Su, X. *Journal of Materials Chemistry A* **2014**, *2*, 813-823.

51. Zhao, Y.; Zhang, Z.; Ren, Y.; Ran, W.; Chen, X.; Wu, J.; Gao, F. *Journal of Power Sources* **2015**, *286*, 1-9.

52. Wang, Z.; Tammela, P.; Stromme, M.; Nyholm, L. *Nanoscale* **2015**, *7*, 3418-

3423.

53. Park, S.; Ruoff, R. S. *Nature Nanotechnology* **2009**, *4*, 217-224.

54. Balandin, A. A.; Ghosh, S.; Bao, W.; Calizo, I.; Teweldebrhan, D.; Miao, F.; Lau, C. N. *Nano Letters* **2008**, *8*, 902-907.

55. Bolotin, K. I.; Sikes, K. J.; Jiang, Z.; Klima, M.; Fudenberg, G.; Hone, J.; Kim, P.; Stormer, H. L. *Solid State Communications* **2008**, *146*, 351-355.

56. Lee, C.; Wei, X.; Kysar, J. W.; Hone, J. *Science* **2008**, *321*, 385-388.

57. Brownson, D. A. C.; Kampouris, D. K.; Banks, C. E. *Journal of Power Sources* **2011**, *196*, 4873-4885.

58. Stoller, M. D.; Park, S.; Zhu, Y.; An, J.; Ruoff, R. S. *Nano Letters* **2008**, *8*, 3498-3502.

59. Li, D.; Muller, M. B.; Gilje, S.; Kaner, R. B.; Wallace, G. G. *Nature Nanotechnology* **2008**, *3*, 101-105.

60. Park, S.; An, J.; Piner, R. D.; Jung, I.; Yang, D.; Velamakanni, A.; Nguyen, S. T.; Ruoff, R. S. *Chemistry of Materials* **2008**, *20*, 6592-6594.

61. Wang, X.; Zhi, L.; Müllen, K. *Nano Letters* **2008**, *8*, 323-327.

62. Xu, Y.; Bai, H.; Lu, G.; Li, C.; Shi, G. *Journal of the American Chemical Society* **2008**, *130*, 5856-5857.

63. Stankovich, S.; Dikin, D. A.; Piner, R. D.; Kohlhaas, K. A.; Kleinhammes, A.; Jia, Y.; Wu, Y.; Nguyen, S. T.; Ruoff, R. S. *Carbon* **2007**, *45*, 1558-1565.

64. Dreyer, D. R.; Park, S.; Bielawski, C. W.; Ruoff, R. S. *Chemical Society Reviews* **2010**, *39*, 228-240.

65. Pei, S.; Zhao, J.; Du, J.; Ren, W.; Cheng, H.-M. *Carbon* **2010**, *48*, 4466-4474.

66. Shin, H.-J.; Kim, K. K.; Benayad, A.; Yoon, S.-M.; Park, H. K.; Jung, I.-S.; Jin, M. H.; Jeong, H.-K.; Kim, J. M.; Choi, J.-Y.;Lee, Y. H. *Advanced Functional Materials* **2009**, *19*, 1987-1992.

67. Si, Y.; Samulski, E. T. *Nano Letters* **2008**, *8*, 1679-1682.

68. Stankovich, S.; Dikin, D. A.; Dommett, G. H. B.; Kohlhaas, K. M.; Zimney, E. J.; Stach, E. A.; Piner, R. D.; Nguyen, S. T.; Ruoff, R. S. *Nature* **2006**, *442*, 282-286.

69. Zhang, J.; Yang, H.; Shen, G.; Cheng, P.; Zhang, J.;Guo, S. *Chemical Communications* **2010**, *46*, 1112-1114.

70. McAllister, M. J.; Li, J.-L.; Adamson, D. H.; Schniepp, H. C.; Abdala, A. A.; Liu, J.; Herrera-Alonso, M.; Milius, D. L.; Car, R.; Prud'homme, R. K.;Aksay, I. A. *Chemistry of Materials* **2007**, *19*, 4396-4404.

71. Jeon, J.-W.; Kwon, S. R.; Lutkenhaus, J. L. *Journal of Materials Chemistry A* **2015**, *3*, 3757-3767.

72. Zhou, M.; Wang, Y.; Zhai, Y.; Zhai, J.; Ren, W.; Wang, F.; Dong, S. *Chemistry – A European Journal* **2009**, *15*, 6116-6120.

73. Bai, H.; Li, C.; Shi, G. *Advanced Materials* **2011**, *23*, 1089-1115.

74. Huang, X.; Zeng, Z.; Fan, Z.; Liu, J.; Zhang, H. *Advanced Materials* **2012**, *24*, 5979-6004.

75. Byon, H. R.; Gallant, B. M.; Lee, S. W.; Shao-Horn, Y. *Advanced Functional Materials* **2013**, *23*, 1037-1045.

76. Li, L.; Raji, A.-R. O.; Tour, J. M. *Advanced Materials* **2013**, *25*, 6298-6302.

77. Peng, L.; Peng, X.; Liu, B.; Wu, C.; Xie, Y.; Yu, G. *Nano Letters* **2013**, *13*, 2151-2157.

78. Wang, X.; Zhou, X.; Yao, K.; Zhang, J.; Liu, Z. *Carbon* **2011**, *49*, 133-139.

79. Yu, G.; Hu, L.; Liu, N.; Wang, H.; Vosgueritchian, M.; Yang, Y.; Cui, Y.; Bao, Z. *Nano Letters* **2011**, *11*, 4438-4442.

80. Zhang, F.; Zhang, T.; Yang, X.; Zhang, L.; Leng, K.; Huang, Y.; Chen, Y. *Energy & Environmental Science* **2013**, *6*, 1623-1632.

81. Chang, H.-H.; Chang, C.-K.; Tsai, Y.-C.; Liao, C.-S. *Carbon* **2012**, *50*, 2331-2336.

82. Wang, D.-W.; Li, F.; Zhao, J.; Ren, W.; Chen, Z.-G.; Tan, J.; Wu, Z.-S.; Gentle, I.; Lu, G. Q.; Cheng, H.-M. *ACS Nano* **2009**, *3*, 1745-1752.

83. Wu, Q.; Xu, Y.; Yao, Z.; Liu, A.; Shi, G. *ACS Nano* **2010**, *4*, 1963-1970.

84. Yin, S.; Zhang, Y.; Kong, J.; Zou, C.; Li, C. M.; Lu, X.; Ma, J.; Boey, F. Y. C.; Chen, X. *ACS Nano* **2011**, *5*, 3831-3838.

85. Beidaghi, M.; Wang, C. *Advanced Functional Materials* **2012**, *22*, 4501-4510.

86. Byon, H. R.; Lee, S. W.; Chen, S.; Hammond, P. T.; Shao-Horn, Y. *Carbon* **2011**, *49*, 457-467.

87. Vollrath, F.; Knight, D. P. *Nature* **2001**, *410*, 541-548.

88. Cheng, M.; Chen, W.; Weerasooriya, T. *Journal of Engineering Materials and Technology* **2005**, *127*, 197-203.

89. Cao, K.; Siepermann, C. P.; Yang, M.; Waas, A. M.; Kotov, N. A.; Thouless, M. D.; Arruda, E. M. *Advanced Functional Materials* **2013**, *23*, 2072-2080.

90. Lin, T. K.; Wu, S. J.; Lai, J. G.; Shyu, S. S. *Composites Science and Technology* **2000**, *60*, 1873-1878.

91. Saikrasun, S.; Amornsakchai, T.; Sirisinha, C.; Meesiri, W.; Bualek-Limcharoen, S. *Polymer* **1999**, *40*, 6437-6442.

92. Li, G.; Zhang, C.; Wang, Y.; Li, P.; Yu, Y.; Jia, X.; Liu, H.; Yang, X.; Xue, Z.; Ryu, S. *Composites Science and Technology* **2008**, *68*, 3208-3214.

93. Mathur, A.; Netravali, A. N. *Journal of Materials Science* **1996**, *31*, 1265-1274.

94. Rajabian, M.; Dubois, C. *Polymer Composites* **2006**, *27*, 129-137.

95. Yu, Z.; Ait-Kadi, A.; Brisson, J. *Polymer Engineering and Science* **1991**, *31*, 1222-1227.

96. Fan, J.; Wang, J.; Shi, Z.; Yu, S.; Yin, J. *Materials Chemistry and Physics* **2013**, *141*, 861-868.

97. Fan, J.; Shi, Z.; Zhang, L.; Wang, J.; Yin, J. *Nanoscale* **2012**, *4*, 7046-7055.

98. Fan, J.; Shi, Z.; Tian, M.; Yin, J. *RSC Advances* **2013**, *3*, 17664-17667.

99. Lyu, J.; Wang, X.; Liu, L.; Kim, Y.; Tanyi, E. K.; Chi, H.; Feng, W.; Xu, L.; Li, T.; Noginov, M. A.; Uher, C.; Hammig, M. D.; Kotov, N. A. *Advanced Functional Materials* **2016**, *26*, 8435-8445.

100. Decher, G. *Science* **1997**, *277*, 1232-1237.

101. Srivastava, S.; Kotov, N. A. *Accounts of Chemical Research* **2008**, *41*, 1831-1841.

102. Adamczyk, Z.; Weroński, P.; Barbasz, J. *Journal of Colloid and Interface Science* **2008**, *317*, 1-10.

103. Jiang, C.; Markutsya, S.; Tsukruk, V. V. *Langmuir* **2004**, *20*, 882-890.

104. Ko, Y.; Kim, Y.; Baek, H.; Cho, J. *ACS Nano* **2011**, *5*, 9918-9926.

105. Schaaf, P.; Voegel, J.-C.; Jierry, L.; Boulmedais, F. *Advanced Materials* **2012**, *24*, 1001-1016.

106. Zhuk, A.; Mirza, R.; Sukhishvili, S. *ACS Nano* **2011**, *5*, 8790-8799.

107. Kharlampieva, E.; Kozlovskaya, V.; Sukhishvili, S. A. *Advanced Materials* **2009**, *21*, 3053-3065.

108. Bieker, P.; Schönhoff, M. *Macromolecules* **2010**, *43*, 5052-5059.

109. Buron, C. C.; Filiâtre, C.; Membrey, F.; Bainier, C.; Buisson, L.; Charraut, D.; Foissy, A. *Thin Solid Films* **2009**, *517*, 2611-2617.

110. McAloney, R. A.; Sinyor, M.; Dudnik, V.; Goh, M. C. *Langmuir* **2001**, *17*, 6655-6663.

111. Schoeler, B.; Poptoshev, E.; Caruso, F. *Macromolecules* **2003**, *36*, 5258-5264.

112. Shiratori, S. S.; Rubner, M. F. *Macromolecules* **2000**, *33*, 4213-4219.

113. Andreeva, D. V.; Skorb, E. V.; Shchukin, D. G. *ACS Applied Materials & Interfaces* **2010**, *2*, 1954-1962.

114. Ariga, K.; Lvov, Y. M.; Kawakami, K.; Ji, Q.; Hill, J. P. *Advanced Drug Delivery Reviews* **2011**, *63*, 762-771.

115. Han, B.-H.; Manners, I.; Winnik, M. A. *Chemistry of Materials* **2005**, *17*, 3160-3171.

116. Ji, Q.; Honma, I.; Paek, S.-M.; Akada, M.; Hill, J. P.; Vinu, A.; Ariga, K. *Angewandte Chemie* **2010**, *122*, 9931-9933.

117. Kim, B.-S.; Park, S. W.; Hammond, P. T. *ACS Nano* **2008**, *2*, 386-392.

118. Lee, S. W.; Kim, B.-S.; Chen, S.; Shao-Horn, Y.; Hammond, P. T. *Journal of the American Chemical Society* **2009**, *131*, 671-679.

119. Shchukin, D. G.; Zheludkevich, M.; Yasakau, K.; Lamaka, S.; Ferreira, M. G. S.; Möhwald, H. *Advanced Materials* **2006**, *18*, 1672-1678.

120. Li, Y.; Wang, X.; Sun, J. *Chemical Society Reviews* **2012**, *41*, 5998-6009.

121. Izquierdo, A.; Ono, S. S.; Voegel, J. C.; Schaaf, P.; Decher, G. *Langmuir* **2005**, *21*, 7558-7567.

122. Mulhearn, W. D.; Kim, D. D.; Gu, Y.; Lee, D. *Soft Matter* **2012**, *8*, 10419-10427.

123. Kim, S. Y.; Hong, J.; Kavian, R.; Lee, S. W.; Hyder, M. N.; Shao-Horn, Y.; Hammond, P. T. *Energy & Environmental Science* **2013**, *6*, 888-897.

124. Chiarelli, P. A.; Johal, M. S.; Holmes, D. J.; Casson, J. L.; Robinson, J. M.; Wang, H.-L. *Langmuir* **2002**, *18*, 168-173.

125. Lee, S. W.; Yabuuchi, N.; Gallant, B. M.; Chen, S.; Kim, B.-S.; Hammond, P. T.; Shao-Horn, Y. *Nature Nanotechnology* **2010**, *5*, 531-537.

126. Hyder, M. N.; Lee, S. W.; Cebeci, F. Ç.; Schmidt, D. J.; Shao-Horn, Y.; Hammond, P. T. *ACS Nano* **2011**, *5*, 8552-8561.

127. Putz, K. W.; Compton, O. C.; Segar, C.; An, Z.; Nguyen, S. T.; Brinson, L. C. *ACS Nano* **2011**, *5*, 6601-6609.

128. Chen, H.; Müller, M. B.; Gilmore, K. J.; Wallace, G. G.; Li, D. *Advanced Materials* **2008**, *20*, 3557-3561.

129. Medhekar, N. V.; Ramasubramaniam, A.; Ruoff, R. S.; Shenoy, V. B. *ACS Nano*

2010, *4*, 2300-2306.

130. Park, S.; Lee, K.-S.; Bozoklu, G.; Cai, W.; Nguyen, S. T.; Ruoff, R. S. *ACS Nano* **2008**, *2*, 572-578.

131. Li, Z.; Mi, Y.; Liu, X.; Liu, S.; Yang, S.; Wang, J. *Journal of Materials Chemistry* **2011**, *21*, 14706-14711.

132. Li, D.; Huang, J.; Kaner, R. B. *Accounts of Chemical Research* **2008**, *42*, 135-145.

133. Tran, H. D.; Li, D.; Kaner, R. B. *Advanced Materials* **2009**, *21*, 1487-1499.

134. Wan, M. *Advanced Materials* **2008**, *20*, 2926-2932.

135. Chaudhari, S.; Sharma, Y.; Archana, P. S.; Jose, R.; Ramakrishna, S.; Mhaisalkar, S.; Srinivasan, M. *Journal of Applied Polymer Science* **2013**, *129*, 1660-1668.

136. Lu, Q.; Zhao, Q.; Zhang, H.; Li, J.; Wang, X.; Wang, F. *ACS Macro Letters* **2013**, *2*, 92-95.

137. Mi, H.; Zhang, X.; Yang, S.; Ye, X.; Luo, J. *Materials Chemistry and Physics* **2008**, *112*, 127-131.

138. Zhang, K.; Zhang, L. L.; Zhao, X. S.; Wu, J. *Chemistry of Materials* **2010**, *22*, 1392-1401.

139. Huang, J. X.; Kaner, R. B. *Angewandte Chemie* **2004**, *43*, 5817-5821.

140. Du, X.; Skachko, I.; Barker, A.; Andrei, E. Y. *Nature Nanotechnology* **2008**, *3*, 491-495.

141. Zhang, Z.; Chen, G.; Wang, H.;Zhai, W. *Journal of Materials Chemistry C* **2015**, *3*, 1649-1654.

142. Guo, H.-L.; Wang, X.-F.; Qian, Q.-Y.; Wang, F.-B.; Xia, X.-H. *ACS Nano* **2009**, *3*, 2653-2659.

143. Sheng, K.; Bai, H.; Sun, Y.; Li, C.; Shi, G. *Polymer* **2011**, *52*, 5567-5572.

144. Lee, S. W.; Gallant, B. M.; Lee, Y.; Yoshida, N.; Kim, D. Y.; Yamada, Y.; Noda, S.; Yamada, A.; Shao-Horn, Y. *Energy & Environmental Science* **2012**, *5*, 5437-5444.

145. Al-Mashat, L.; Shin, K.; Kalantar-zadeh, K.; Plessis, J. D.; Han, S. H.; Kojima, R. W.; Kaner, R. B.; Li, D.; Gou, X.; Ippolito, S. J.; Wlodarski, W. *The Journal of Physical Chemistry C* **2010**, *114*, 16168-16173.

146. Cong, J.; Chen, Y.; Luo, J.; Liu, X. *Journal of Solid State Chemistry* **2014**, *218*, 171-177.

147. Yan, X.; Chen, J.; Yang, J.; Xue, Q.; Miele, P. *ACS Applied Materials & Interfaces* **2010**, *2*, 2521-2529.

148. Sarker, A. K.; Hong, J.-D. *Langmuir* **2012**, *28*, 12637-12646.

149. Lee, S. W.; Kim, J.; Chen, S.; Hammond, P. T.; Shao-Horn, Y. *ACS Nano* **2010**, *4*, 3889-3896.

150. Krogman, K. C.; Zacharia, N. S.; Schroeder, S.; Hammond, P. T. *Langmuir* **2007**, *23*, 3137-3141.

151. Schlenoff, J. B.; Dubas, S. T.; Farhat, T. *Langmuir* **2000**, *16*, 9968-9969.

152. Kim, B.-S.; Smith, R. C.; Poon, Z.; Hammond, P. T. *Langmuir* **2009**, *25*, 14086-14092.

153. Krogman, K. C.; Lyon, K. F.; Hammond, P. T. *The Journal of Physical Chemistry B* **2008**, *112*, 14453-14460.

154. Otto, T.; Mundra, P.; Schelter, M.; Frolova, E.; Dorfs, D.; Gaponik, N.; Eychmüller, A. *ChemPhysChem* **2012**, *13*, 2128-2132.

155. Hong, J.; Kang, S. W. *Journal of Nanoscience and Nanotechnology* **2011**, *11*, 7771-7776.

156. Tung, T. T.; Castro, M.; Kim, T. Y.; Suh, K. S.; Feller, J.-F. *Journal of Materials Chemistry* **2012**, *22*, 21754-21766.

157. Tung, T. T.; Castro, M.; Pillin, I.; Kim, T. Y.; Suh, K. S.; Feller, J. F. *Carbon* **2014**, *74*, 104-112.

158. Hummers, W. S.; Offeman, R. E. *Journal of the American Chemical Society* **1958**, *80*, 1339-1339.

159. Pei, S.; Cheng, H.-M. *Carbon* **2012**, *50*, 3210-3228.

160. Wang, H.; Hao, Q.; Yang, X.; Lu, L.; Wang, X. *Nanoscale* **2010**, *2*, 2164-2170.

161. Sathiya, M.; Prakash, A. S.; Ramesha, K.; Tarascon, J. M.; Shukla, A. K. *Journal of the American Chemical Society* **2011**, *133*, 16291-16299.

162. Cutler, C. A.; Bouguettaya, M.; Reynolds, J. R. *Advanced Materials* **2002**, *14*, 684-688.

163. Jeon, J.-W.; O'Neal, J.; Shao, L.; Lutkenhaus, J. L. *ACS Applied Materials & Interfaces* **2013**, *5*, 10127-10136.

164. He, Y.; Chen, W.; Li, X.; Zhang, Z.; Fu, J.; Zhao, C.; Xie, E. *ACS Nano* **2013**, *7*, 174-182.

165. Jeong, H. T.; Kim, B. C.; Gorkin, R.; Higgins, M. J.; Wallace, G. G. *Electrochimica Acta* **2014**, *137*, 372-380.

166. Weng, Z.; Su, Y.; Wang, D.-W.; Li, F.; Du, J.; Cheng, H.-M. *Advanced Energy Materials* **2011**, *1*, 917-922.

167. Zhou, G.; Li, F.; Cheng, H.-M. *Energy & Environmental Science* **2014**, *7*, 1307-1338.

168. Ji, L.; Meduri, P.; Agubra, V.; Xiao, X.; Alcoutlabi, M. *Advanced Energy Materials* **2016**, *6*, 1502159.

169. Wu, S.; Xu, R.; Lu, M.; Ge, R.; Iocozzia, J.; Han, C.; Jiang, B.; Lin, Z. *Advanced Energy Materials* **2015**, *5*, 1500400.

170. Yan, J.; Wang, Q.; Wei, T.; Fan, Z. *Advanced Energy Materials* **2014**, *4*, 1300816.

171. Stoller, M. D.; Ruoff, R. S. *Energy & Environmental Science* **2010**, *3*, 1294-1301.

172. Yang, M.; Cao, K.; Sui, L.; Qi, Y.; Zhu, J.; Waas, A.; Arruda, E. M.; Kieffer, J.; Thouless, M. D.; Kotov, N. A. *ACS Nano* **2011**, *5*, 6945-6954.

173. Gu, R.; Yu, J.; Hu, C.; Chen, L.; Zhu, J.; Hu, Z. *Applied Surface Science* **2012**, *258*, 10168-10174.

174. Park, B.; Lee, W.; Lee, E.; Min, S. H.; Kim, B.-S. *ACS Applied Materials & Interfaces* **2015**, *7*, 3329-3334.

175. Tung, S.-O.; Ho, S.; Yang, M.; Zhang, R.; Kotov, N. A. *Nature Communications* **2015**, *6*, 6152.

176. Zhu, J.; Cao, W.; Yue, M.; Hou, Y.; Han, J.;Yang, M. *ACS Nano* **2015**, *9*, 2489-2501.

177. Lee, S. W.; Kim, B.-S.; Chen, S.; Shao-Horn, Y.; Hammond, P. T. *Journal of the*

American Chemical Society **2008**, *131*, 671-679.

178. Avouris, P. *Nano Letters* **2010**, *10*, 4285-4294.

179. Zhang, Z.; Chen, G.; Wang H.; Zhai, W. *Journal of Materials Chemistry C* **2015**, *3*, 1649-1654.

180. Zhang, X.; Chen, H.; Zhang, H. *Chemical Communications* **2007**, *14*, 1395-1405.

181. Bai, Y.; Ho, S.; Kotov, N. A. *Nanoscale* **2012**, *4*, 4393-4398.

182. Zhang, H.; Shih, J.; Zhu, J.; Kotov, N. A. *Nano Letters* **2012**, *12*, 3391-3398.

183. Zhu, J.; Zhang, H.; Kotov, N. A. *ACS Nano* **2013**, *7*, 4818-4829.

184. Sader, J. E.; Chon, J. W. M.; Mulvaney, P. *Review of Scientific Instruments* **1999**, *70*, 3967.

185. Butt, H.-J.; Cappella, B.; Kappl, M. *Surface Science Reports* **2005**, *59*, 1-152.

186. Salehi-Mobarakeh, H.; Ait-Kadi, A.; Brisson, J. *Polymer Engineering & Science* **1996**, *36*, 778-785.

187. Hsiao, M.-C.; Liao, S.-H.; Yen, M.-Y.; Teng, C.-C.; Lee, S.-H.; Pu, N.-W.; Wang, C.-A.; Sung, Y.; Ger, M.-D.; Ma, C.-C. M.; Hsiao, M.-H. *Journal of Materials Chemistry* **2010**, *20*, 8496-8505.

188. Su, Q.; Pang, S.; Alijani, V.; Li, C.; Feng, X.; Müllen, K. *Advanced Materials* **2009**, *21*, 3191-3195.

189. Liu, S.; Chan, C.-M.; Weng, L.-T.; Li, L.; Jiang, M. *Macromolecules* **2002**, *35*, 5623-5629.

190. Penn, L.; Milanovich, F. *Polymer* **1979**, *20*, 31-36.

191. Ferrari, A. C.; Meyer, J. C.; Scardaci, V.; Casiraghi, C.; Lazzeri, M.; Mauri, F.;

Piscanec, S.; Jiang, D.; Novoselov, K. S.; Roth, S.; Geim, A. K. *Physical Review Letters* **2006**, *97*, 187401.

192. Zhu, Y.; Stoller, M. D.; Cai, W.; Velamakanni, A.; Piner, R. D.; Chen, D.; Ruoff, R. S. *ACS Nano* **2010**, *4*, 1227-1233.

193. Wang, M.; Duong, L. D.; Mai, N. T.; Kim, S.; Kim, Y.; Seo, H.; Kim, Y. C.; Jang, W.; Lee, Y.; Suhr, J.; Nam, J.-D. *ACS Applied Materials & Interfaces* **2015**, *7*, 1348-1354.

194. Yang, X.; Cheng, C.; Wang, Y.; Qiu, L.; Li, D. *Science* **2013**, *341*, 534-537.

195. Zhang, L. L.; Zhou, R.; Zhao, X. S. *Journal of Materials Chemistry* **2010**, *20*, 5983-5992.

196. Chang, L.; Wei, W.; Sun, K.; Hu, Y. H. *Journal of Materials Chemistry A* **2015**, *3*, 10183-10187.

197. Maiti, U. N.; Lim, J.; Lee, K. E.; Lee, W. J.; Kim, S. O. *Advanced Materials* **2014**, *26*, 615-619.

198. Sumboja, A.; Foo, C. Y.; Wang, X.; Lee, P. S. *Advanced Materials* **2013**, *25*, 2809-2815.

199. Batteas, J. D.; Stark, R. E., Surface and Interfacial Studies of Plant Biopolymers by SPM and NMR. In *Molecular Interfacial Phenomena of Polymers and Biopolymers*, Chen, P., Ed. Woodhead Publishing Ltd., Cambridge, UK, **2005**, pp 580-608.

200. Derjaguin, B. V.; Muller, V. M.; Toporov, Y. P. *Journal of Colloid and Interface Science* **1975**, *53*, 314-326.

201. Park, S.; Lee, K. S.; Bozoklu, G.; Cai, W.; Nguyen, S. T.; Ruoff, R. S. *ACS Nano*

2008, *2*, 572-578.

202. Shirshova, N.; Qian, H.; Shaffer, M. S. P.; Steinke, J. H. G.; Greenhalgh, E. S.; Curtis, P. T.; Kucernak, A.; Bismarck, A. *Composites Part A: Applied Science and Manufacturing* **2013**, *46*, 96-107.

203. Shirshova, N.; Bismarck, A.; Carreyette, S.; Fontana, Q. P. V.; Greenhalgh, E. S.; Jacobsson, P.; Johansson, P.; Marczewski, M. J.; Kalinka, G.; Kucernak, A. R. J.; Scheers, J.; Shaffer, M. S. P.; Steinke, J. H. G.; Wienrich, M. *Journal of Materials Chemistry A* **2013**, *1*, 15300-15309.

204. Snyder, J.; Gienger, E.; Wetzel, E. *Journal of Composite Materials* **2015**, *49*, 1835-1848.

205. Snyder, J. F.; Carter, R. H.; Wetzel, E. D. *Chemistry of Materials* **2007**, *19*, 3793-3801.

206. Mo, R.; Tung, S. O.; Lei, Z.; Zhao, G.; Sun, K.; Kotov, N. A. *ACS Nano* **2015**, *9*, 5009-5017.

207. Qian, H.; Diao, H.; Shirshova, N.; Greenhalgh, E. S.; Steinke, J. G. H.; Shaffer, M. S. P.; Bismarck, A. *Journal of Colloid and Interface Science* **2013**, *395*, 241-248.

208. Rivera, M.; Cole, D. P.; Hahm, M. G.; Reddy, A. L. M.; Vajtai, R.; Ajayan, P. M.; Karna, S. P.; Bundy, M. L. In *Lightweight carbon nanotube-based structural-energy storage devices for micro unmanned systems*, SPIE, Baltimore, Maryland, USA, **2012**.

209. Shirshova, N.; Qian, H.; Houlle, M.; Steinke, J. H. G.; Kucernak, A. R. J.; Fontana, Q. P. V.; Greenhalgh, E. S.; Bismarck, A.; Shaffer, M. S. P. *Faraday Discussions* **2014**, *172*, 81-103.

210. Zhu, Y.; Murali, S.; Cai, W.; Li, X.; Suk, J. W.; Potts, J. R.; Ruoff, R. S. *Advanced Materials* **2010**, *22*, 3906-3924.

211. Gwon, H.; Kim, H.-S.; Lee, K. U.; Seo, D.-H.; Park, Y. C.; Lee, Y.-S.; Ahn, B. T.; Kang, K. *Energy & Environmental Science* **2011**, *4*, 1277-1283.

212. Liu, F.; Song, S.; Xue, D.; Zhang, H. *Advanced Materials* **2012**, *24*, 1089-1094.

213. Wen, Z.; Wang, X.; Mao, S.; Bo, Z.; Kim, H.; Cui, S.; Lu, G.; Feng, X.; Chen, J. *Advanced Materials* **2012**, *24*, 5610-5616.

214. Yuan, C. Z.; Gao, B.; Shen, L. F.; Yang, S. D.; Hao, L.; Lu, X. J.; Zhang, F.; Zhang, L. J.; Zhang, X. G. *Nanoscale* **2011**, *3*, 529-545.

215. Pham, D. T.; Lee, T. H.; Luong, D. H.; Yao, F.; Ghosh, A.; Le, V. T.; Kim, T. H.; Li, B.; Chang, J.; Lee, Y. H. *ACS Nano* **2015**, *9*, 2018-2027.

216. Wang, G.; Sun, X.; Lu, F.; Sun, H.; Yu, M.; Jiang, W.; Liu, C.; Lian, J. *Small* **2012**, *8*, 452-459.

217. Takayanagi, M.; Katayose, T. *Journal of Polymer Science: Polymer Chemistry Edition* **1981**, *19*, 1133-1145.

218. Tanner, D.; Fitzgerald, J. A.; Phillips, B. R. *Angewandte Chemie International Edition in English* **1989**, *28*, 649-654.

219. Yang, M.; Cao, K.; Yeom, B.; Thouless, M.; Waas, A.; Arruda, E. M.; Kotov, N. A. *Journal of Composite Materials* **2015**, *49*, 1873-1879.

220. Ghislandi, M.; Tkalya, E.; Schillinger, S.; Koning, C. E.; de With, G. *Composites Science and Technology* **2013**, *80*, 16-22.

221. Potts, J. R.; Dreyer, D. R.; Bielawski, C. W.; Ruoff, R. S. *Polymer* **2011**, *52*, 5-

25.

222. Park, S.; An, J.; Potts, J. R.; Velamakanni, A.; Murali, S.; Ruoff, R. S. *Carbon* **2011**, *49*, 3019-3023.

223. Wang, D.-W.; Sun, C.; Zhou, G.; Li, F.; Wen, L.; Donose, B. C.; Lu, G. Q.; Cheng, H.-M.; Gentle, I. R. *Journal of Materials Chemistry A* **2013**, *1*, 3607-3612.

224. Zhang, L.; Liang, J.; Huang, Y.; Ma, Y.; Wang, Y.; Chen, Y. *Carbon* **2009**, *47*, 3365-3368.

225. Cui, P.; Lee, J.; Hwang, E.; Lee, H. *Chemical Communications* **2011**, *47*, 12370-12372.

226. Wang, D.-W.; Du, A.; Taran, E.; Lu, G. Q.; Gentle, I. R. *Journal of Materials Chemistry* **2012**, *22*, 21085-21091.

227. Zhao, X.; Zhang, Q.; Chen, D.; Lu, P. *Macromolecules* **2010**, *43*, 2357-2363.

228. Dikin, D. A.; Stankovich, S.; Zimney, E. J.; Piner, R. D.; Dommett, G. H. B.; Evmenenko, G.; Nguyen, S. T.; Ruoff, R. S. *Nature* **2007**, *448*, 457-460.

229. Park, S.; Suk, J. W.; An, J.; Oh, J.; Lee, S.; Lee, W.; Potts, J. R.; Byun, J.-H.; Ruoff, R. S. *Carbon* **2012**, *50*, 4573-4578.

230. Barisci, J. N.; Wallace, G. G.; Baughman, R. H. *Journal of Electroanalytical Chemistry* **2000**, *488*, 92-98.

231. Che, J.; Chen, P.; Chan-Park, M. B. *Journal of Materials Chemistry A* **2013**, *1*, 4057-4066.

232. Li, S.; Zhao, C.; Shu, K.; Wang, C.; Guo, Z.; Wallace, G. G.; Liu, H. *Carbon* **2014**, *79*, 554-562.

233. Ma, Y.; Li, P.; Sedloff, J. W.; Zhang, X.; Zhang, H.; Liu, J. *ACS Nano* **2015**, *9*, 1352-1359.

234. Rigueur, J. L.; Hasan, S. A.; Mahajan, S. V.; Dickerson, J. H. *Carbon* **2010**, *48*, 4090-4099.

235. Zhang, X.; Sui, Z.; Xu, B.; Yue, S.; Luo, Y.; Zhan, W.; Liu, B. *Journal of Materials Chemistry* **2011**, *21*, 6494-6497.

236. Baechle, D. M.; O'Brien, D. J.; Wetzel, E. D. In *Structural dielectrics for multifunctional capacitors*, SPIE, San Diego, California, USA, **2008**.

237. O'Brien, D. J.; Baechle, D. M.; Wetzel, E. D. In *Performance Metrics for Structural Composite Capacitiors*, SMASIS 2010, Philadelphia, Pennsylvania, USA, **2010**.

238. O'Brien, D. J.; Baechle, D. M.; Wetzel, E. D. *Journal of Composite Materials* **2011**, *45*, 2797-2809.